Mohamed Boudiaf University - M’sila

FACULTY OF TECHNOLOGY

Serial number …………………

Registration number: D.ME/3C/03/19

Thesis

Submitted for the award of the diploma of

DOCTORAT LMD

Department: Mechanical engineering

Specialty: Energetic

Theme

Study of turbulent flow through a fan

Candidate

AMOUR Aissa

Defended on: 06/03/2024

Defended before the jury composed of:

Last Name & First Name	Grade	Establishment	Position
ZAOUI Moussa	**Professor**	Univ. de **M’sila**	President
MENASRI Noureddine	**Professor**	Univ. de **M’sila**	Advisor
BAKHTI Fatima Zohra	**MCA**	Univ. de **M’sila**	Co-advisor
MAKRI Hocine	**MCA**	Univ. de **M’sila**	Examiner
MOUSSAOUI Mustafa	**Professor**	Univ. de **Djelfa**	Examiner
AMROUNE Salah	**Professor**	Univ. de **M’sila**	Guest

Academic Year : 2023/2024

Acknowledgement

Completing this doctoral thesis has marked a profound journey of personal and academic growth, continuous learning, and discovery. I extend my heartfelt gratitude to the individuals who have played a pivotal role in making this endeavor possible. Foremost among them is my advisor, Prof. Dr. **Noureddine MENASRI**. His unwavering support, guidance, and invaluable mentorship have significantly shaped the trajectory of this research. I am fortunate to have worked under his supervision, and his dedication throughout this journey has been indispensable. I am also grateful to Dr. **Bakhti Fatima Zohra** for her support and advice throughout my doctoral studies.

I sincerely thank Mr. **Zaoui Moussa**, a professor at the University of M'sila, for graciously agreeing to preside over the thesis committee. My gratitude also extends to Mr. **MAKRI Hocine**, a professor at the University of M'sila, for his willingness to evaluate this work, and to Mr. **Moussaoui Mustafa**, Professor at the University of Djelfa, for his thoughtful assessment of the research. Additionally, I am deeply thankful to Mr. **Amroune Salah** for accepting the invitation to join as a guest on the thesis committee.

I appreciate the stimulating academic environment and collaborative opportunities my colleagues and fellow researchers at the University of M'sila provide. Their support has been instrumental in the development of this research.

Special appreciation goes to my father and mother for their enduring encouragement. Their steadfast support has been my pillar during the challenges of this academic journey. Lastly, I dedicate this work to express profound gratitude to my wife. It is challenging to encapsulate in words the depth of my appreciation. Embarking on the PhD journey together a few years ago was both demanding and beautiful, and it is solely due to her boundless support and exceptional patience that we have completed it as a team.

Contents

List of Symbols

Greek Symbols

α	Particle impact angle
ϵ	dissipation rate of turbulent kinetic energy
η_t	Total effeciency
λ	Viscous stress tensor
μ_f	Fluid dynamic viscosity
μ_t	Eddy viscosity
Φ	Extensive proprety
ϕ	Intensive proprety
ρ_p	Particle density
τ	Viscous stress tensor
τ_p	Particle response time
τ_t	Characteristic eddy lifetime

Math symbols

δ_{ij}	Kronecker delta function
∇	Diveregence operator
$\overline{S_{ij}}$	mean strain-rate tensor
D_{ij}	Rate of deformation tensor

Nondimensional numbers

R_e	Reynolds number

Roman Symbols

u_τ	friction velocity
ℓ_{mix}	Prandtl's mixing length
η_s	static effeciency
κ	von Kármán constant
$\mathbf{b}$	Body forces
$\mathbf{n}$	Outward normal vector
$\overline{U}$	Mean velocity
d_p	Particle diameter
E_r	Erosion rate
Ke	kinetic energy
L	Integral length scale of turbulence
P_s	Static pressure
P_t	Total pressure
P_{ref}	Reference velocity pressure
Q_d	Design flow rate
Stk	Stokes number
T	Impeller period
t	time
u'	Root mean square of fluid velocity fluctuation
u'	velocity fluctuation in the x-axis
u^+	dimensionless velocity
U_2	Blade speed at trailing edge
v'	velocity fluctuation in the y-axis

V_p	Particle impact velocity
w'	velocity fluctuation in the z-axis
y^+	dimensionless wall distance
k	turbulent kinetic energy
M	Torque
N	Rtoational speed
RF	Rotational frequency
$\mathrm{W}_{\mathrm{shaft}}$	Power shaft
y	Normal distance from the cell centroid to the adjacent wall

Acronyms

AF	Airfoil
BC	Backward-curved blades
BEP	Best effeciency point
BI	backward-inclined blades
CFD	Computational fluid dynamics
CS	Control system
CV	control volume
DDPM	Dense discrete phase model
E-E	Euleurian-Euleurian
E-L	Euleurian-Lagrangian
FC	forward-curved blades
FDM	Finite difference methods
FEM	Finite element methods
FVM	Finite volume methods
IF	Impact frequency
KE	Kinetic energy
LSP	Large-Size particles
MRF	Multiple reference frame

RANS	Reynolds-Averaged Navier-stokes
RB	Radial-blades
RT	Radial-tip blades
RTT	Reynold transport theorem
SRF	Single reference frame
SSP	Small-Size particles
URANS	Unsteady Reynolds-Averaged Navier-stokes

List of Figures

List of Tables

Chapter 1

Introduction general

1.1 Erosion in Turbomachines: An Overview of the Issues

Multiphase flows refer to flows where multiple materials, each potentially in distinct states or with different chemical properties but in the same state, flow simultaneously in a system, such as combinations of gases, liquids, and solids, are frequently encountered across a range of engineering applications. In many industrial processes, multiphase flow is the desired outcome of the process. Within the sector of material conveyance such as pneumatic conveyance systems, multi-phase flows play a fundamental role in the efficient handling and effective transfer of materials. Practical examples of such applications encompass chemical reactors, oil transportation pipelines, and the food processing industry. In these cases, understanding and managing multi-phase flows is imperative for attaining the intended process results.

Conversely, there are situations where multi-phase flows are undesirable side effects that should be either avoided or minimized. Consider oil and gas pipelines, where the inclusion of liquid droplets or solid particles within the gas stream can trigger issues like erosion, corrosion, and pipeline blockages, resulting in expensive maintenance and operational disruptions. In such contexts, the system's design and operation must prioritize the prevention or minimization of multi-phase flows to ensure optimal functionality.

Solid particle erosion represents a prevalent issue within turbomachinery applications, primarily due to multiple factors that allow the introduction of particles into pumps, turbines, compressors, and fans where the system typically involves multiphase flows. The erosion phenomenon involves the collision of solid particles with the surfaces of turbomachinery components, potentially resulting in material loss, surface roughening, and, eventually, component failure. The occurrence of erosion can manifest in various parts of the turbomachinery, including impellers, blades, diffusers, and volutes. The specific location depends on the prevailing flow conditions and the attributes of the solid particles.

Centrifugal pumps find extensive utility in applications involving pumping substantial quantities of solid-liquid mixtures, often referred to as slurries. Within this context, the primary components that experience high erosion rates include the impeller, liners, and notably, the pump casing, which is the component most susceptible to particle impact, as indicated by Wilson [2]. In contrast, the erosion observed in turbines and compressors tends to be more severe compared to that in pumps. This heightened erosion rate is attributed to the higher gas velocities and the presence of intricate flow patterns. Consequently, erosion can manifest in various parts of these devices, including the rotor blades, stator vanes, and casing. In the case of fans, erosion exhibits similarities to its occurrence in pumps. Here, it is the impeller and volute that are prone to erosion, influenced by particle impact on the blade surfaces and the recirculation of particles within the flow.

In summary, erosion in multiphase flows poses a substantial challenge for turbomachinery, including pumps, turbines, compressors, and fans. It can result in decreased performance, a shorter operational lifespan, and escalated maintenance expenditures. Effectively predicting and mitigating erosion necessitates a comprehensive grasp of erosion mechanisms, as well as the development and validation of CFD-based erosion models. Consequently, the industrial fan community aims to understand the mechanisms of solid particle erosion and design fans that can withstand erosive environments without affecting performance.

1.2 Erosion in Centrifugal Fans: A Case Study of Induced Mill Fan (FN-280)

The cement manufacturing process is highly rigorous, including various industrial operations. The severe conditions, characterized by abrasive and adhesive substances, continuously challenge all equipment and machinery, including fans. Consequently, cement plants must rely on robust and heavy-duty fans. Among these fans is the backward-curved centrifugal mill fan, dedicated to precise tasks within a specific manufacturing process. A notable example is the cement mill fan (FN-280), an induced draft fan employed to generate a negative pressure airflow to ensure the good work of the dust abatement operation in a Bag-Filter housing system as part of the milling process (Figure 1.1).

Under standard operating conditions,it is expected that the gas flow passing through the bag filter positioned upstream of the fan will maintain a low concentration of solid particles, ideally not exceeding a threshold of 30 mg/m^3. However, when the filter fabric experiences damage, the entrained dust concentration in the flow stream can significantly rise. Consequently, contingent upon the fan flow rate and the properties of the dust, the fan becomes more vulnerable to a high erosion rate. This increased wear affects both the rotating and stationary components of the fan, which are exposed to abrasive dust, leading to a reduction in the thickness of these components. Ultimately, this results in a noticeable decrease in the equipment's lifespan. This, in turn, adversely affects the fan's performance and may result in substantial expenses and production disruptions, particularly when fan blades require replacement (Figure 1.2). Notably, high dust concentration and the presence of exceptionally abrasive particulates can accelerate the reduction of the fan components' thickness. Importantly, this erosion is typically asymmetric, contributing to rotor imbalance and placing augmented loads on the bearings while inducing vibrations.

Erosion issues emerged on the Mill-Fan (FN-280) at the Lafarge Cement plant in

Figure 1.1: Bag-Filter housing of the dedusting system (BF-260)

.

M'Sila, Algeria, several years ago. This particular facility encompasses four integrated cement production lines. Interestingly, all the FN-280 lines had been in operation since 2003, operating without any prior erosion-related problems. However, the situation changed when the dust-laden airflow passing through the fan intensified due to issues with the damaged Bag-filter fabric. In these new operating conditions, the existing fan struggled to run without encountering difficulties. Over time, the rotor components endured severe damage, prompting the maintenance team to consider repairing the fan rotor blade, recognized as the most affected component. To address this, the plant's maintenance team initiated rotor repairs by introducing wear plates on the pressure

Figure 1.2: Fan Impeller failure

.

side of the fan blades, with the aim of prolonging the rotor's operational lifespan (Figure 1.3). These repair activities were conducted locally within the mechanical workshop. Despite these repair efforts, fan vibrations persisted, largely attributed to the inevitable rotor imbalance. Consequently, further mechanical balancing of the rotors remains a critical requirement.

Erosion of centrifugal fan blades represents a prominent challenge in the field of industrial fan design. This issue is particularly prevalent when considering centrifugal fans deployed within cement applications, as they typically handle particle-laden flows with erosive particles. The impact of solid particle erosion can manifest in various damaging forms, including material loss, cracking, pitting, and even the generation of erosion-induced vibrations. These detrimental effects introduce alterations in the fan blades' geometry profiles, culminating in a reduction of both chord length and thickness. Collectively, these changes lead to a decline in overall fan efficiency and reliability of the fan. Furthermore, the associated maintenance and replacement costs may rise

Figure 1.3: Sacrificial plates welded on the blade pressure side

.

significantly. Therefore, understanding the mechanisms of erosion and establishing effective mitigation strategies is paramount.

To address solid particle erosion in turbomachinery, a range of approaches is available. These encompass judicious material selection, surface treatment methods, protective coatings, and design enhancements. Surface treatment methods, such as shot peening, can enhance surface hardness and erosion resistance. The application of protective coatings, such as ceramics or metallic coatings, can offer a barrier against erosion. While the aforementioned strategies are valuable in reducing erosion, particularly on impeller blades, the optimization of design holds a pivotal role in predicting erosion patterns and minimizing susceptibility to erosion. This, in turn, aids in estimating the rate of material loss. Design optimization primarily targets the modification of the flow field to reduce particle impact frequency, and location and alter particle impact characteristics that lead to a minimum erosion rate. When considering design modifications, parameters like particle impact angle, velocity, and mechanical properties of the material should be investigated and considered.

In summary, design optimization is not a theoretical matter but a practical necessity. It ensures the longevity and reliability of fans in demanding industrial environments, making it a critical phase of any fan design process. Consequently, the development of computational methods capable of predicting erosion patterns is of great importance when designing new industrial fans intended for operation in erosive environments. This ensures the longevity and optimal performance of such fans.

1.3 Motivation for the Present Research

Despite the considerable resources allocated to investigating solid particle erosion in turbomachinery, the underlying mechanisms of this erosive process remain inadequately understood. Previous studies on erosion within turbomachinery predominantly focused on pumps and compressors, overlooking the distinct challenges faced by centrifugal fans. While these studies have provided valuable insights into material wear, behavior, and protective measures, they fall short of capturing the peculiar flow characteristics, operating conditions, and erosive patterns specific to centrifugal fans. Consequently, erosion mechanisms within these important machines remain limited. In industries like cement plants, centrifugal fans play a central role and are constantly exposed to abrasive cement particles that can lead to severe wear. Surprisingly, there has been a noticeable scarcity of research investigating the impact of erosion on centrifugal fans, despite their widespread utilization.

various experimental methods have been employed to study slurry pumps, such as the paint wear method (PWM) [6,7], inductive displacement transducer (IDT) [8], scanning electron microscopic (SEM) [9], and particle image velocimetry (PIV) [10–18]. Through these approaches, measuring material mass loss, imagining erosion morphology, and visualizing flow characteristics were realized. These methods have contributed to a more comprehensive understanding of multiphase flows and wall erosion in slurry pumps. However, it's important to note that experimental studies are often associated with high costs, intensive labor, and time-consuming processes. This is particularly evident in erosion measurement, where physical pump models need to be intentionally damaged.

While conducting experimental studies on erosion in turbomachinery applications can be both challenging and expensive, a numerical methodology offers a viable alternative. Computational fluid dynamics (CFD) has emerged as a valuable tool for the prediction of erosion in multiphase flow systems. Over recent years, numerical modeling has attracted significant attention and engagement from a diverse range of scientists and engineers. During this period, models have been extensively developed and effectively applied across many practical applications. CFD investigations have evolved into a fundamental element in the field of industrial product design and engineering processes, including those related to turbomachinery applications. Although CFD predictions do not entirely supplant experimental investigations, they undeniably play a crucial role in providing a deeper understanding of intricate flow phenomena. One noteworthy advantage of this approach lies in its ability to provide valuable local and temporal data, often challenging to obtain through experimental means.

The CFD-based erosion models typically involve the coupling of a fluid solver with a particle tracking algorithm that simulates the trajectories of particles in the flow. However, the accuracy of the CFD-based erosion models is highly dependent on the quality of the turbulence and particle models used, as well as the validation of the model against experimental data. Furthermore, the complexity and variability of the erosion mechanisms in multiphase flows pose significant challenges in the development and validation of CFD-based erosion models. Regarding this fact, in order to track the erodent particles and have an in-depth insight into the erosion pattern by means of a numerical approach, it is crucial to accurately predict the 3D flow field to capture the peculiar flow physics within the centrifugal fan. However, the flow field in the fan is turbulent, characterized by a high Reynolds number with inevitable flow separation. Therefore, making the prediction of the flow field in the fan using computational methods is a challenging task.

1.4 Scope and Objectives of the thesis

The primary aim of this thesis is to investigate the performance characteristics and erosion issues of a large centrifugal fan that is in operation at a cement plant. This investigation utilizes CFD methodologies in order to validate the numerical technique adopted and to gain a deeper understanding of how fan design and operating conditions influence the likelihood of fan component failures caused by solid particle erosion. The thesis is focused on achieving the following Objectives:

- Performing numerical simulations to investigate the complex flow field inside the backward-S-curved fan and providing a basis for verification of the numerical simulations and validating the CFD model adopted.
- Investigating the erosion process and mechanisms by means of numerical simulation using a Particle transport model coupled with a CFD solver and investigating the reliability and effectiveness of the model to replicate the on-field erosion pattern.

- To investigate the effects of change in flow regime and particle loads on erosion patterns.
- Studying the effects of geometrical modifications on the aerodynamic performance of the fan and erosion pattern.

For an in-depth analysis of the fan's flow behavior, numerical simulations are performed using Unsteady Reynolds-Averaged Navier-stokes (URANS) simulation. The results of these numerical simulations are then compared with experimental data derived in accordance with the industrial fan testing standard ISO 5801 requirements, thereby allowing for a rigorous evaluation of the accuracy of the adopted CFD solver, grid configuration, and turbulence modeling. Additionally, the tracking of solid particles and their impact characteristics are resolved using a Particle transport model, in conjunction with an empirical erosion model, to examine the erosion patterns on the fan components. The numerical erosion patterns are then subjected to a qualitative comparison against actual erosion patterns obtained from on-site inspections. Within the scope of this thesis, numerical simulation serves as the primary tool to explore the effects of varying the number of impeller blades and making adjustments to the blade's outlet angle. This exploration aims to gain insights into their combined impact on the fan's aerodynamic performance and erosion rates and patterns.

1.5 Thesis Structure

To provide a clear roadmap of the structure of this thesis, the following sections outline the content and objectives of each chapter.

- **Chapter 1** serves as an introduction to the erosion challenges faced by turbomachines, with a particular focus on centrifugal fans. It elucidates the adverse effects of solid particle erosion on fan components and the subsequent impact on operational lifespan. A case study of a cement plant centrifugal fan (FN-280) suffering erosion-related issues is presented, underscoring the need for effective erosion mitigation strategies. The research is driven by a gap in understanding erosion in centrifugal fans, prompting the exploration of CFD solutions. The scope and objectives of the thesis are outlined.

- **Chapter 2** establishes foundational principles of erosion mechanisms. The chapter also discusses the difficulty of modeling solid particle erosion in turbomachinery applications, shedding light on key erosion parameters. Furthermore, this chapter presents a critique of the literature of relevant research on solid particle erosion in turbomachinery, including both experimental and CFD-based methodologies.

- **Chapter 3**. Within this chapter, various centrifugal fan types, their working principles, and the distinct advantages associated with each type are explored. Furthermore, a detailed examination of the utilization of centrifugal fans in cement plants is conducted, with a specific emphasis on the pivotal role played by the induced cement mill fan (FN-280) throughout the cement milling process. In addition, the section provides insight into the methodology of reverse design engineering. It elucidates the underlying reasons for opting for this approach to create the CAD model of the fan's blade.

- **Chapter 4** initiates a comprehensive discourse on the CFD methodology employed within the scope of this study. This entails detailed elucidations of the essential governing equations for resolving the flow dynamics and modeling of particle-laden flows. Moreover, it encompasses an in-depth discussion of the solution procedure for solving the mathematical equations and the numerical techniques that have been applied. Furthermore, it provides a mesh sensitivity study and validation of the particle track model.

- **Chapter 5** presents the obtained outcomes derived from the numerical prediction of the fan performance curve, particle dispersion, and the erosion patterns exhibited on the fan components. We undertake an in-depth analysis and discussion of the characteristics of particle impact, providing valuable insights into critical parameters that influence erosion patterns, including impact frequency, velocity, and angle. Subsequently, we delve into an investigation of the impact of geometric modification to the fan design, such as adjustments in blade outlet angle and the number of blades, on erosion rates and patterns.

- **Chapter 6** summarizes the outcomes of this study and shows the conclusions drawn and the recommendations for future studies.

Chapter 2

Literature Review

2.1 Solid Particle Erosion mechanisms

Erosion is the process in which material is removed from a metal surface due to the interaction with either solid particles suspended in the gas stream, known as dry erosion, or with a liquid medium that may or may not contain suspended particles, referred to as aqueous erosion. The presence of solid particles significantly intensifies the erosion process, which occurs through various degradation mechanisms [3]. To cause structural damage to the target material, the impacting solid particles must carry a sufficient amount of Kinetic energy (KE) [4]. The size and velocity of these particles play a crucial role in determining the extent of erosion.

Although erosion fundamentally involves the removal of material from a surface due to particle impact, the mechanisms governing this process can exhibit notable distinctions when comparing brittle and ductile materials. Nevertheless, a widely accepted postulation is that erosion, regardless of the material type, is driven by two primary mechanisms, namely cutting and deformation. The cutting mechanism is linked to particles impacting at oblique angles, while the deformation mechanism is associated with particles impacting at normal angles [5], inducing plastic deformation on the target surface [6]. Given the vast diversity in material properties, it becomes apparent that the one-size-fits-all approach to quantifying the removal of target material is implausible. The mechanism governing erosion is predominantly steered by the inherent ductility of the metal involved.

From a historical perspective, the study of erosion mechanisms in ductile metals dominated the academic literature until the 1970s [7]. Finnie pioneered investigations into erosion behavior mechanisms of ductile materials, introducing his initial ductile erosion model based on the concept of micro-cutting. He suggested that micro-cutting primarily drove erosion in ductile materials and even proposed a micro-geometry model tailored to such materials [4]. Figure 2.1 visually outlines the typical sequence of events in a ductile erosion mechanism. The formation of a crater by an impinging particle serves as the initial indicator of the erosion process, followed by the accumulation of subsequent impacts that enlarge the crater. The continual impacts ultimately lead to the removal of the accumulated material [8]. However, it's important to note that this model displayed an underestimation of erosion magnitude for particles striking at high-impact angles compared to experimental findings [8]. Subsequently, it was revealed that micro-cutting wasn't the primary erosion mechanism for ductile materials [9]. Instead, material removal from the metal surface is primarily driven by localized plastic deformation, wherein the material is eliminated through the cutting action of the eroding particle [10].

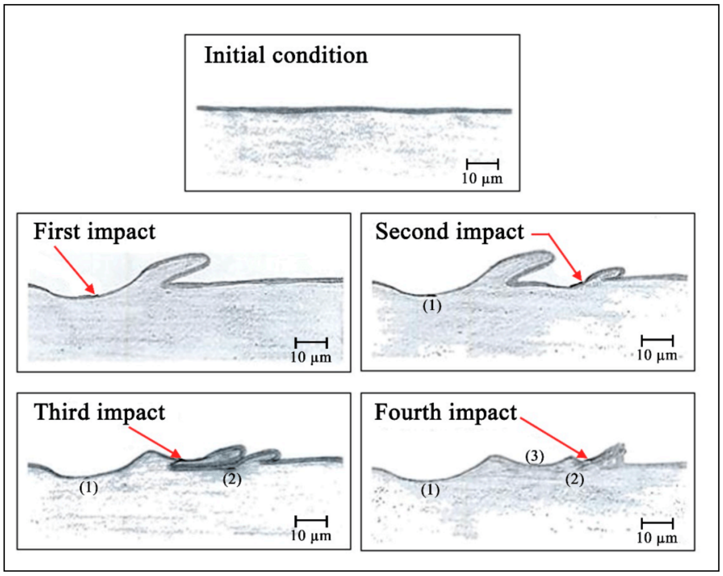

Figure 2.1: Ductile erosion mechanism micro cutting or plastic deformation. [11]

Brittle materials experience erosion through a mechanism characterized by chipping and cracking. The solid particle erosion process in brittle materials is well-established, with a widely accepted understanding. Erosion in brittle materials is attributed to the formation of cracks. When a particle impacts a brittle surface, it initiates the creation of lateral and radial cracks. Subsequent impacts on this surface lead to the propagation and growth of these cracks. Consequently, these cracks divide the target surface into smaller fragments, which are subsequently expelled as particles continue to impact the surface. The formation and progression of cracks stand out as the predominant erosion mechanism in brittle materials.

The results of erosion studies often express the ratio of the surface mass or volume removal to impinging particle mass. In general, the erosion rate of a given material is affected by the particles' impact velocity and impingement angle [12]. The variation in erosion rate with impingement angle is characteristically different for ductile and brittle material as shown schematically in Figure 2.2 According to the figure, it is obvious that the erosion rate is strongly related to the impact angle for both materials. furthermore if the damage is caused by a ductile mechanism then the maximum rate of erosion typically takes place at shallow angles of impact between 20°and 30°.while for brittle erosion mechanism, the maximum rate of erosion rate typically takes place at a normal angle of 90°. This is attributed to the predominantly different mechanisms of cutting and brittle fracture.

2.2 Solid particle erosion modeling

In a broader context, a deep understanding of the dynamics governing multiphase flows is an essential prerequisite for effectively designing, and controlling numerous engineering systems. This requirement demands a comprehensive, interdisciplinary approach that draws from the fields of fluid mechanics, thermodynamics, transport phenomena, and materials science. As engineering applications continue to advance, becoming increasingly complex and diverse, the importance of conducting research and

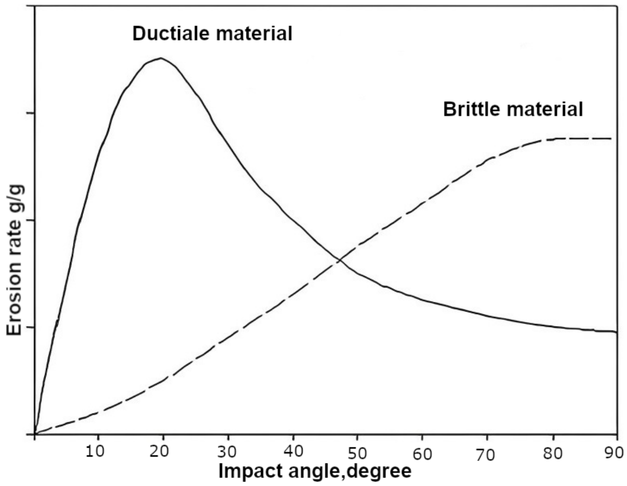

Figure 2.2: Erosion rate at different impact angles for ductile and brittle materials. [13]

development in the realm of multiphase flows is expected to grow even further.

The extent of material removal from a surface due to eroding solid particles in a fluid stream depends upon the prevailing flow conditions and the specific mechanism driving the material's removal. understanding the erosion process can be dissected into two primary phases. The first phase involves using fluid flow conditions to determine the particle impact characteristics like impact angle and velocity as they hit the target surface, the subsequent phase involves quantifying the material that is removed from the surface.

Solid particle erosion emerges as an intricate phenomenon marked by the complex interactions between particles and various components of the turbomachine. It can affect a range of surfaces, including blade surfaces, blade tips, leading and trailing edges, and it may even extend to the inner surfaces of volutes and diffusers. The extent and severity of erosion are influenced by multiple factors, including the mechanical properties of both the target surface material and solid particles, the impact velocity and angle of particle impacts, particle concentration, and the geometrical properties of the particles [14]. Importantly, these parameters are relatively significant regardless of the material being either brittle or ductile. However, not all of these factors are easily controllable or measurable during tests [15], and considering the combination of these diverse factors in influencing erosion, studying them independently can be quite challenging.

2.2.1 Key Factors Affecting Erosion in Ductile Materials

When designing new rotating machinery that may operate in environments prone to erosion, it is imperative to thoroughly investigate how the erosion rate is influenced by various factors related to particle flow within the system, as well as the materials used for constructing the critical components of the turbomachine. Predicting erosion in rotating machinery is an exceedingly extreme challenge. This complexity predominantly stems from the fact that erosion is governed by a multitude of variables, including particle impact characteristics, such as impact velocity and angle, along with the particle impact frequency. These factors are significantly influenced by the flow conditions of the carrier fluid, and practical examples may be found where alterations in these conditions have had a substantial impact, either exacerbating or mitigating erosion [10]. Furthermore, it is essential to track the trajectory of particles through the flowfield after multiple impacts. Following the impact on the surfaces, the particles may rebound with even higher velocities, which heightens the probability of subsequent, more severe impacts [16].

Since the 1960s, substantial contributions have been made in understanding the impact of particle interactions with ductile materials in erosive environments [17–20]. Extensive research and erosion models have emerged, building upon initial theories to encompass a wide range of factors affecting the erosion of ductile materials. While these key erosion-influencing parameters are frequently analyzed independently, it is vital to recognize that their impacts on erosion are frequently interrelated and not mutually exclusive.

2.2.1.1 Impact angle

The study of erosion in ductile materials is crucial because the impact angle at which particles strike the material surface dictates the material removal mechanism. It is essential to characterize these interactions to accurately predict erosion rate and behavior. The impact angle essentially determines whether the primary material removal mechanism is indentation or cutting. Historically, early theories categorized erosion mechanisms in ductile materials as cutting at shallow impact angles and plastic deformation at high impact angles. However, these theories did not encompass the full complexity of the erosion process, particularly the effects of multiple particle impacts. Current understanding recognizes that multiple mechanisms come into play following a single particle impact, and the cumulative impact of multiple particles is a significant factor in erosion [21].

Subsequent research has consistently shown that erosion in ductile materials is highly sensitive to the impingement angle of particles. Studies investigating the impact angle's effects on erosion have consistently demonstrated varying rates of material removal at different angles. Typically, the highest erosion rates are observed when the impact angle ranges from about 20° to 30° for ductile materials [10, 22–24].

2.2.1.2 Flow condition and impact velocity

In engineering contexts, the fluid dynamics and particle transport within a fluid medium indirectly influence the characteristics of particle impact on surfaces, thereby influencing erosion rates and patterns. When a particle is transported by a fluid flow toward a surface, the fluid surrounding the particle departs from its original path to travel alongside the surface. This deflection induces drag forces on the particle's surface, culminating in an alteration of the particle's trajectory. Consequently, the particle follows a path that may not align with the flow streamlines.

Perturbations in the fluid flow, such as modifications in the surface roughness and adjustments in the geometry of the flow domain, can result in either an increase or decrease in erosion rates. This is due to the deviation of particle trajectories from the fluid's streamlines, subsequently heightening the probability of surface impacts and influencing impact characteristics such as velocity.

Fundamental research has explored the relationship between the wear rate and the velocity of particle impacts, while more practical investigations have delved into how the wear rate changes concerning the overall flow velocity within particular systems [15]. Both categories of studies have shown that velocity exerts a substantial influence on the wear rate. Impact velocity, in conjunction with impact angle, has often been a subject of investigation, revealing that the alteration in erosion rate follows a power-law relationship:

$$E_r = KV_p^n f(\alpha) \tag{2.1}$$

E_r is the erosion rate, V_P is the velocity of the impacting particle (m/s), K is an empirical constant and n is the velocity exponent that depends on the particle and the surface properties. This velocity exponent lies typically in the range from 2 to 4 [25]. Higher values of the exponent tend to be associated with brittle metals [22]. thus Higher impingement velocity of course means higher kinetic energy leading to higher local erosion.

2.2.1.3 Solid particle size and shape

Particle size exerts a dual influence on the erosion process [21]. The size of particles significantly affects their trajectories within the fluid medium, consequently changing their impact locations on the target surface. This influence is due to the predominant forces acting upon the particles, including surface forces like drag and body forces such as gravity. Notably, smaller particles, characterized by their low Stokes number, tend to experience limited separation from the fluid flow [15]. Consequently, they exhibit a strong inclination to closely adhere to the flow streamlines. This behavior notably brings about substantial alterations in their impact characteristics, encompassing factors like impact frequency and the impact location, particularly when compared to larger particles.

Furthermore, the particle size plays a crucial role in determining the subsequent impact of particles on the target surface. Consequently, the effect of particle size on erosion has consistently maintained a central focus in academic research in this domain [26]. This factor directly influences the calculation of erosion rate density, where there is a direct correlation between erosion rate density and the mass of particles, as elaborated in Chapter 4. Smaller particles, characterized by their lower kinetic energy, induce comparatively lower impact stresses on the surface when contrasted with their larger counterparts. Even in the controlled conditions of erosion test rigs, where the total mass of erodent particles remains constant, it has been observed that the increased number of impacts resulting from the larger quantity of smaller particles does not offset the reduced kinetic energy associated with these smaller particles [27].

2.2.1.4 Solid particle concentration

Many researchers have revealed that higher particle concentration in the carried fluid leads to a higher erosion rate due to the increasing number of particle impacts.

2.3 CFD Modeling of Erosion in turbomachines

The particle impact characteristics, such as velocity and angle, are heavily influenced by the internal flow field within the fan's domain. conducting experiments to measure erosion rate and its subsequent effects on operating fans is both time-consuming and costly. Furthermore, it can be challenging to assess all the factors that contribute to erosion through experimental studies, particularly as some of these factors cannot be controllable or measurable during experimental investigation. However, By using computational methods in turbomachinery, engineers can gain a more flexible and cost-effective approach to exploring different design configurations and operating conditions, which may not be practical to test experimentally. Moreover, numerical simulations can provide more detailed and comprehensive data on flow features and erosion patterns, which may be challenging or impossible to measure through physical experiments. Despite these limitations, visual inspections of fan components during routine maintenance can still yield valuable qualitative insights into the extent and severity of erosion [28].

The process of conducting numerical erosion modeling using CFD typically involves the solution of the flow field of the continuous phase and the simulation of particle trajectories. Tracking these particle paths relies on numerically integrating the equations of motion governing the particles as they travel through the computational domain. Due to their inherent inertia, particles tend to diverge from the continuous phase, particularly when encountering changes in direction or during acceleration and deceleration, ultimately leading to their impact on the fan surfaces. Consequently, trajectory simulations necessitate the solution of the flow field and the surface boundaries as inputs, along with the incorporation of a model to account for particle restitution following each surface impact.

In modern practice, particle trajectory simulations have evolved to incorporate the influence of viscosity and three-dimensional flow effects, mirroring advancements in turbomachinery flowfield solutions. Notably, the solutions of 3D Reynolds-Averaged Navier-stokes (RANS) equations for turbulent flow are increasingly applied in tracking the turbulent dispersion of particles and the subsequent erosion in turbomachinery simulations [12].

From this perspective, two numerical methodologies have been developed to simulate multiphase flows. the Euleurian-Euleurian (E-E) approach and The Euleurian-

Lagrangian (E-L) approach. In the Eulerian-Eulerian approach (E-E), the Navier-Stokes equation is simultaneously solved within a cell-based framework for both the continuous phase and the solid phase. thus both fluid and solid share the same cell. Numerous investigations have been conducted to explore flow characteristics under solid-liquid two-phase conditions in pumps. These studies primarily aim to assess the impact of various factors characterizing solid-liquid two-phase flows, including the volume fraction of solid particles, particle size, and specific gravity, on aspects such as the flow field, turbulent properties, hydraulic losses, overall performance, and erosion of fan components [29–33]. In these studies, wear on pump components was investigated by employing indicators based on the distribution and volume fraction of solid particles.

In a related study, Alawadhi et al. [34] performed a numerical analysis of the erosion behavior in an industrial slurry pump. The two-phase system was addressed using the Eulerian-Eulerian approach. The governing equations for the fluid phase were solved with commercial Computational Fluid Dynamics (CFD) software (ANSYS CFX), and turbulence effects were modeled using the shear stress turbulence (SST) model. Finnie's model [15] was adopted to evaluate the erosion rate on the casing wall and blade under different solid volume fractions. A parametric examination was conducted to explore the influence of critical parameters, such as particle size, concentration, flow conditions, and cavitation, on the erosion characteristics of the pump. The results indicate that the concentration of solid particles significantly impacts the pump's erosion characteristics, followed by particle size and size distribution. Conversely, exit pressure head and cavitation exert less influence on erosion rates but significantly affect the regions with elevated erosion rate densities.

The E-E approach yields precise results, especially in situations with high particle concentrations, where the inter-phase interactions are incorporated as an additional source term in the momentum equations. Nonetheless, this methodology does not consider the dynamic behavior of individual particles, thereby hindering its ability to provide accurate predictions of particle dispersion within highly turbulent flows. In addition, given that the erosion rate is influenced by various factors, such as impact velocity and angle, as previously discussed, this particular data cannot be directly obtained using the Eulerian-Eulerian (E-E) approach. Moreover, the E-E approach becomes computationally demanding when dealing with modeling a diverse range of particle sizes and is less accurate in scenarios where particles are randomly distributed throughout the fluid domain.

In contrast, the Eulerian-Lagrangian (E-L) approach presents an alternative that can overcome some of these limitations. This method explicitly models the motion of individual particles within the Lagrangian frame, thereby accommodating the effects of particle-particle interactions. Additionally, the E-L approach is more adept at handling particles with a diverse range of sizes by tracking the trajectories of randomly seeded individual particles rather than assuming a uniform distribution throughout the domain.

The extensive use of pumps in various industrial sectors, including industrial production, mining, dredging, urban sewage treatment, and more, underscores the importance of studying how particle characteristics in solid-liquid two-phase flows impact the performance and service life of centrifugal pumps transporting solid-liquid two-phase flows. This becomes particularly challenging when considering the reliability of these pumps. To address these challenges, the Eulerian-Lagrangian (E-L) approach, also known as the Discrete Phase Model (DPM) combined with erosion models, has been widely employed in slurry pumps suffering erosion problems, especially in cases of low solid concentrations or when particle-particle collisions are of minimal significance [35–42]. However, in many industrial applications, pumps operate under conditions characterized by high concentrations of particles in the mixture, which can result in distinct performance variations. In such scenarios, the Dense discrete Phase Model (DDPM) is typically adopted. The Dense discrete phase model (DDPM) assumes a two-way coupling between the two phases, providing a more accurate representation of the interactions in these high particle concentration conditions [43, 44].

2.4 Erosion modeling in centrifugal fans

In recent years, The study of the erosion behavior of centrifugal fans has gained significant attention. This interest can be attributed to the widespread use of centrifugal fans in a multitude of industrial sectors, ranging from ventilation and air conditioning to material handling. In the subsequent section, we will explore a range of research related to erosion within the context of centrifugal fans. These comprehensive investigations include various aspects of erosion, such as the numerical prediction of erosion patterns, the examination of factors influencing erosion rates, and the assessment of the validity of different approaches and models. Furthermore, they delve into the meticulous scrutiny of the myriad factors that exert influence on erosion rates. Through these reviews, we aim to provide a comprehensive overview of the current state of knowledge in the field of erosion in centrifugal fans and to identify areas that require further exploration and research.

In a study led by Aldi et al. [45], the erosion behavior of a single-inlet centrifugal fan, operational within a cement factory, was examined in the context of its exposure to abrasive Clinker particles. The primary objective of this research was to assess the effectiveness of strategically positioned wear-resistant plates in mitigating erosion-induced damage across various sections of the fan. To establish a reliable numerical model, the research authors conducted an experimental analysis of clinker powder through Scanning Electron Microscopy to examine the morphology of the powder, along with the determination of particle size distribution using a particle sizer spectrometer. The findings unveiled that a majority of particles exhibited rounded shapes, with approximately 80% of the sample mass composed of particles with a diameter less than 5 μm. Additionally, the researchers conducted microstructural characterization of the wear-resistant hard-facing. For the numerical modeling, the Eulerian-Lagrangian (E-L) approach was adopted to model the particle-laden flow. To accurately account for turbulence and flow unsteadiness, a stochastic tracking model was employed to model the turbulent dispersion of particles. Particles were strategically seeded for various flow-field conditions corresponding to different time steps to consider the impact of flow unsteadiness on particle dynamics. 10^6 of particles were released from the intake at the same inlet gas velocity. Erosion rates were calculated using Finnie's model, with the values of model constants chosen based on experimental results from S.G. Sapate et al [46]. The accuracy of the flow field solutions was validated by comparing them with experimentally measured values, revealing a negligible discrepancy of about 3.4%. The flow behavior within the blade passage and at the impeller exit displayed a consistent pattern, largely attributed to the interaction between the impeller and the casing walls. This interaction induced a gradual distortion of the high-velocity flow, leading to substantial flow separation along the blade passage, particularly in the proximity of the blade's suction side. The results obtained through computational fluid dynamics (CFD) exhibited remarkable concurrence with actual erosion observations, underscoring the model's accuracy in replicating erosion patterns observed in the fan surfaces during visual inspections. The research outcomes shed light on the influential role of flow unsteadiness in influencing extent and erosion rates on the casing surfaces. These fluctuations were a direct consequence of alterations in flow dynamics, resulting in varying particle impact velocities and angles. Furthermore, the research findings underscored the substantial influence of particle impact angles on the erosion process affecting fan surfaces.

Traditionally, researchers have proposed methods to improve material wear resistance, often employing sacrificial plates or coatings with superior wear properties.

A recent study conducted by Aldi et al. [47] employed both experimental and numerical approaches to optimize the placement of wear-resistant plates on selected fan components. They experimentally measured the erosion rates of three wear-resistant plates using a jet-impingement test rig. This evaluation involved using particle characteristics replicating those encountered in actual industrial settings, ensuring accurate reproduction of erosion patterns and magnitudes through numerical methods. The researchers designed the test bench to characterize the erosion behavior of the wear-resistant materials at various impact angles and velocities. Preliminary tests were performed to validate the test bench's reliability, following ASTM G76 standards [48]. Three distinct wear-resistant plates, denoted as M1, M2, and M3, each possessing different chemical compositions and properties, were subjected to testing at different impact velocities and impact angles 15°, 30°, 45°, 60°, and 90°with a particle mass flow rate of 10 $gmin^{-1}$. The experimental results were fitted to the erosion rate model based on Finnie's work [49], which relates erosion to impact velocity, angle function, and erosion coefficients for particle impingement at a normal angle. Oka's model [50] was then employed to interpolate the experimental results and formulate a general expression for the angle function suitable for use in CFD analyses. The experimental outcomes indicated that the M3 wear-resistant plate exhibited the highest performance, while M1 performed the least effectively. To assess the extent of wear on the internal components of the fan, the fan surfaces were divided into zones. Erosion rate was quantified in terms of average thickness reduction over 8000 hours of operation. The study's conclusions emphasized the importance of a meticulous approach to the placement of wear-resistant plates, considering factors such as plate cost, wear resistance, and the degree of wear in specific impeller sections. The authors recommended using the most wear-resistant material (M3) in areas with significant erosion while opting for more cost-effective materials (M1 and M2) in regions with less severe wear concerns. Specifically, they proposed the use of M3 for the leading edge, a patch of the pressure side near the trailing edge, and a portion of the shroud. M2 was suggested for the center of the back plate, and the casing cut-off. The remaining part of the impeller and the casing where wear was less pronounced could be coated with the less-performing wear-resistant plate (M1) without compromising the component's longevity.

The choice of a wear-resistant plate is dependent on the particular application and the expected wear levels. Various types of wear-resistant plates are accessible in the market, each with its distinct cost and performance properties. Costs can fluctuate based on factors such as material composition and thickness. The selection and arrangement of wear-resistant plates within a fan typically involve a trade-off between the manufacturer's expertise and material expenses. However, in recent years, an intriguing approach has emerged, drawing inspiration from the morphology of desert animals to enhance the wear-resistance properties of surfaces against particle erosion [51–54].

In light of the aforementioned considerations, Zhang et al. [55] applied this concept to enhance the erosion resistance of Backward-curved blades (BC) fan blades. They drew inspiration from nature, where certain animals adapted to erosive environments have evolved effective anti-erosion strategies through unique surface morphology, micro-structures, and biological flexibility. The researchers introduced the concept of bionic fan blades, inspired by these natural designs. the studies explored the factors that influence erosion rates, including particle impact velocity, particle concentration, size, and impact angle, recognizing the significant impact of changing flow conditions on erosion. The study involved investigating the effect of various particle diameters on impact locations and the subsequent erosion rate and making comparisons between standard and bionic fan blade configurations. To simulate the solid-gas two-phase flow, the Eulerian-Lagrangian (E-L) approach was employed. The bionic blade design featured a 20 mm elliptical groove profile spacing. Different particle diameters, specifically 20, 50, and 100 μm, were considered. When examining the erosion behavior resulting from a particle diameter of $100\mu m$, it was observed that both standard fan blades and the bionic configuration experienced wear, mainly in the blade root of the pressure side. Interestingly, in this case, the bionic design exhibited a higher erosion rate than the standard blade. Conversely, the erosion behavior observed with a particle diameter of $20\mu m$ showed distinct characteristics. For conventional fan blades, erosion was evident both at the leading edge and at the exit of the pressure side. In contrast, the bionic fan blade primarily experienced erosion at its leading edge. It's worth noting that the erosion rate of the bionic blade was approximately 0.78% lower than that of the standard blade. This reduction in erosion can be attributed to the decreased impact velocities on the bionic blade surface and the dispersion of particle impact angles, which predominantly fell within a high range of angles, particularly in the 50° to 65° range. This aspect underscores the enhanced erosion resistance of the bionic fan blade surface. Consequently, the bionic fan blade experiences notably less severe erosion compared to its standard counterpart.

Recently, Ghenaiet [56] conducted a study focusing on particle trajectories and erosion in a small industrial centrifugal fan. This research employed a Lagrangian tracking method and a semi-empirical erosion rate correlation. The fan's impeller is equipped with four full forward blades and sixteen splitters, operating at a speed of 2820 rpm. The continuous phase flow field was analyzed using RANS simulation with the $K - \omega$ SST turbulence model. Particle trajectories were tracked during both Best Efficiency Point (BEP) and over-load operating conditions, involving a particle concentration range of 10 to 50 mg/m^3 and sand particles spanning sizes from 5 to 200 μm. The Lagrangian approach was employed, assuming that the particle volume fraction remained lower than 10^{-6}. Erosion rate calculations were based on experimental data from Grant and Tabakoff [16], considering quartz particles impacting an aluminum alloy (2024). The study's results highlighted that erosion in the centrifugal fan primarily occurs in specific regions characterized by high impact frequencies and kinetic energy. These regions include the axial radial bend of the hub and blade junction, the pressure side and tip of full blades, the shroud, the outer wall of the volute, and areas behind the blade pressure side, blade tip, and shroud plate facing. The non-uniformity in the erosion pattern is attributed to the complex interaction between the impeller and casing, further influenced by various operating conditions. The study emphasized the considerable sensitivity of erosion behavior to particle concentrations and flow rates, with erosion intensifying significantly under high levels. Consequently, critical fan areas experience severe erosion, leading to a rapid reduction in the fan's overall lifespan. The findings underscored the central role of impact frequencies and velocities in inducing erosion, particularly in the highlighted regions, providing insights into the mechanisms driving erosion in the centrifugal fan.

Fritsche et al. [57] conducted a study involving radial fans operating within a recycling plant dedicated to end-of-life vehicles (ELVs). These radial fans faced a highly erosive environment due to the presence of 1 mm shredded metal particles transported by a high-temperature gas flow at approximately 530°C. To address this challenge, the researchers designed a baseline impeller and a parameterized spiral volute using CFD. They explored various geometric modifications to the spiral casing and impeller blades, simulating these changes to assess their impact on erosion behavior and performance metrics. In their investigation, they considered six configurations of backward circular arc blades, each corresponding to different blade outlet angles, to examine the effect of blade shape variations on erosion characteristics for both the impellers and the reference volute. The study also delved into an alternative spiral geometry design that featured concentricity and variable pitch angles. The primary objective of this design was to reduce erosion while maintaining fan performance during actual operating conditions. The researchers conducted a comprehensive analysis of the gas flow using RANS simulation and employed the Mixing Plane model to calculate the flux between fan components. For erosion predictions, the Finnie erosion model [10] was utilized on both the impeller and spiral casing. To model particle motion, they employed a Lagrangian approach assuming a one-way coupling. The study revealed several key findings. Notably, larger casing sizes and increased spiral pitch angles resulted in lower erosion rates on the casing wall. This phenomenon was attributed to a shift in impact angles, with larger angles leading to reduced erosion rates. The investigation also examined six-blade designs corresponding to varying exit angles (10°, 40°, 70°, 100°, 130°, and 160°). While greater blade outlet angles were associated with increased total-to-static pressure output and maximum flow rates, they also led to a reduction in achievable efficiency, with up to a 20% decrease between the smallest and largest angles. Importantly, larger blade outlet angles correlated with higher erosion rates on both the blades and the volute wall. Building on their parametric study, the authors devised an optimized fan design capable of withstanding erosion while maintaining hydraulic performance. This design featured a new impeller and an optimized volute. By comparing pressure rise, efficiency, and erosion rates between the reference model and the optimized design, they demonstrated that the optimized fan achieved the required pressure with a 25% higher total-to-static efficiency compared to the baseline design. Furthermore, erosion rates on the new impeller were approximately 25% lower than those on the baseline impeller and nearly 90% lower than on the reference volute.

Multiphase flows frequently involve turbulence, and the behavior of particles is highly affected by the dynamics of turbulence, making it an essential consideration for researchers and engineers working in this field [58]. Turbulent flows are characterized by random fluctuations of flow properties, which give rise to a phenomenon known as turbulent particle dispersion. This phenomenon signifies that particles released from the same initial position but at different time intervals may follow distinct trajectories. Understanding and accurately modeling this turbulent dispersion of particles is crucial for a comprehensive analysis of two-phase flow systems.

Within the Lagrangian framework, which is commonly employed for analyzing particle behavior in turbulent flows, there are two primary methods for addressing turbulent dispersion and transport. These methods are well-established and have their respective merits and computational considerations, Single Particle Tracking (SPT) and Particle Cloud Tracking (PCT). In the Single Particle Tracking approach, a substantial number of representative particles as they travel through the computational domain. This method ensures that the results obtained are statistically independent of the number of injected particles. While it offers a high degree of accuracy in modeling particle dispersion, it comes with a significant computational cost. The computational resources required for SPT are notably higher than those needed for PCT. [59]. On the other hand, the PCT approach involves tracking statistical representations of clusters or clouds of particles. Instead of individually tracking a large number of seeded particles, this method focuses on computing the trajectories of the cloud centers to model the turbulent dispersion of particles. PCT assumes a Gaussian distribution of particles within each cloud, and it considers that each particle moves with the mean velocity of the respective cloud. This modeling approach can be computationally more efficient than SPT, making it a viable choice for simulations involving a large number of particles.

It's important to note that the choice between SPT and PCT should be made judiciously, taking into account the specific requirements of the research, and the available computational resources. Additionally, the assumptions and simplifications inherent in each method should be carefully considered in the context of the specific study. thus, selecting the most appropriate one is a critical decision in the numerical analysis of two-phase flows.

To leverage the efficiency of the Particle Cloud Tracking (PCT) model in terms of the low computer resources model in turbomachinery simulations, Cardillo et al. [60] introduced a modified version of Baxter's original PCT model from 1989 [60]. Their study focused on predicting the performance and erosion patterns of an industrial centrifugal fan using OpenFOAM. Their aim was to gain insights into the flow physics in regions with separated flow, a common occurrence in fans with cambered plate blades, to predict erosion within the fan's rotor. The fan under study is a double-inlet, double-impeller design with 11 backward-swept cambered plate blades. It featured an impeller with a 3.44 m diameter, running at 900 RPM, offering a total pressure rise of 50 kPa and a maximum flow rate of about 750 m^3/s. Numerical simulations used a steady-state "frozen rotor" approach, modeling the interface between the impeller and volute with an Arbitrary Mesh Interface (AMI). Incompressible (RANS) equations were solved, and turbulence was modeled using the standard $k-\epsilon$ model with synthetic wall treatment. The study was validated by comparing computational results with experimental data under peak efficiency and peak pressure conditions. It exclusively focused on the impeller to study the erosion process. Simulations at peak efficiency featured 55 particle clouds, each containing 5 million spherical particles with $5\mu m$ diameter. Erosion prediction relied on a semi-empirical model by Tabackoff et al. [61]. Computational results showed good agreement with experiments, with slight deviations. Underestimations were observed in numerical total pressure values (0.6% and 1.5%) for peak pressure and peak efficiency. Efficiency was overpredicted by 3% and 1%. The peak efficiency operating condition revealed recirculating flows near the blades' leading edge due to non-optimal flow alignment, while the peak pressure flow point exhibited flow separation in all blade-to-blade passages. The PCT approach highlighted non-uniform erosion rates on the impeller walls. Erosion was pronounced at the leading and trailing edges of the suction side and in the middle of the pressure side, notably affecting the hub's conical surface.

The steady simulation conducted by Cardillo et al. [60] offered a reasonable level of accuracy with less computational effort. However, this simulation did not consider the unsteady interaction between the impeller and its housing, resulting in some limitations. To address this, the same authors developed an unsteady numerical simulation based on their previous work, employing a moving mesh technique [62]. In this unsteady approach, the authors implemented a custom code to track particle cloud motion. however, in this study, they used 99 particle clouds evenly distributed at the inlet, with each cloud containing the same number of particles. Particle sizes were grouped into two categories: small particles ranging from 0.1 to 20 μm, and larger particles ranging from 160 to 760 μm. For the simulation, they assumed all clouds comprised particles of 5 μm diameter recognizing that finer particles are the most abrasive. The moving mesh approach effectively predicted total pressure rise, although it slightly under-predicted efficiency by 3.4%. Analyzing the relative velocity field at different time instants in the impeller domain, the authors found that the flow dynamics in each blade-to-blade passage remained consistent over time. This led to the conclusion that for the industrial fan design phase, a steady-state simulation suffices to predict overall performance. However, the study highlighted the limitations of this approach. The frozen rotor method did not account for changes in counter-pressure caused by the asymmetric profile of the casing, leading to non-physical deformation of flow properties within certain blade passages. Additionally, it failed to predict the unsteady flow evolution in the blade passage, which is crucial for modeling erosion. To address these issues, unsteadiness in flow was accounted for for the erosion prediction. The flow field solution at a distinct time instant was introduced as input for the particle tracking code at the corresponding time step. This approach allowed for accounting for flow unsteadiness without directly coupling flow field simulation with the cloud tracking algorithm. The results revealed similar erosion patterns on the impeller surface as in the previous study. However, predictions of the erosion pattern on the blade exhibited significant circumferential non-uniformity in affected regions. This non-uniformity was attributed to the unsteady flow characteristics inducing secondary flow motions and distortion in the blade passages due to impeller-volute interaction.

Corsini et al. [28,63,64] conducted a study using the Eulerian-Lagrangian technique with the Particle Cloud Tracking (PCT) model. Their aim was to explore particle dynamics and erosion within an induced draft fan, driven by unburnt coal and fly ash carried by exhaust gases, utilized in a coal-fired boiler system. The research involved an enhanced version of the PCT model to compute particle dispersion. This solver considered the drifting velocity gradient within the cloud, particularly near solid walls. This adaptation was crucial for addressing the impact of non-uniformities in the velocity distribution within the cloud as particles approached the wall. experimental measurements were performed, considering factors such as particle size, composition, and mass distribution. Particles were present at a concentration of 64.1 mg/m^3. Particle sizes were categorized into two main classes: small particles (1.0 to 45.0 μm) consisting mainly of silicon compounds, and larger coarse carbon-rich particles (ranging from 45.0 to 150 μm). However, the simulation exclusively focused on silicon compounds due to their significant contribution to erosion, unlike carbon-rich particles that were mainly linked to fouling occurrences. The erosion rate was modeled utilizing the empirical formula introduced by Tabakoff where the coefficients were matched to those relevant for stainless steel impacted by coal ash particles. The erosion patterns were closely aligned with those observed on an actual blade, albeit with some variations. The simulation results underscore particles with a diameter of 32.5–67.5 μm as the most erosive. The simulation results emphasized that the tip region, particularly near the stagnation point, exhibits the highest levels of erosion. Additionally, vulnerable areas on the blade PS included areas near the blade tip, leading edge, and hub. Intriguingly, a section in the blade center remains relatively unaffected by particle impacts. Meanwhile, on the suction side, the simulation indicates that erosion primarily concentrates around the tip and leading edge. Furthermore, The estimated blade deterioration rate using an average erosion rate was reasonably consistent with experimental data at nominal equivalent operative conditions. authors attributed this discrepancy to factors like load variations during operation, the modification of flow fields due to blade surface deterioration as well as other parameters that play a role in erosion prediction such as the flow temperature and the particle shape.

In conclusion, the existing body of research dedicated to erosion modeling in the context of centrifugal fans remains relatively scarce. This is somewhat surprising, given the prevalent challenges related to fan erosion within industrial applications and the eager interest within the industrial fan community to develop strategies for mitigating erosion rates by optimizing fan design. Nonetheless, numerical modeling of erosion characteristics in a centrifugal fan is challenging, influenced by many parameters already discussed in section 2.2. Importantly, many of these parameters are intrinsic to the specific geometry and flow conditions of the fan. Consequently, it's imperative to recognize that predictions made for one particular fan design may not be universally applicable to other fan geometries. This highlights the need for further exploration and tailored approaches in the domain of centrifugal fan erosion research to address the specific and unique challenges associated with various fan configurations.

Chapter 3

Fan design and characteristics

3.1 Centrifugal Fans with Backward-curved blades

Centrifugal fans can be classified into six types based on their impeller blade shapes and blade angles: fans with (BC), Airfoil (AF),backward-inclined blades (BI),Radial-tip blades (RT),forward-curved blades (FC) and Radial-blades (RB) impellers (See Figure 3.1). Each of these fan types has its unique advantages and disadvantages, making them suitable for specific applications [65].

Essentially, these fans impart energy to the fluid as it traverses the blade passage, engaging with the rotating impeller. The change in angular momentum of the fluid in the blade passage results in a net torque in the axis of rotation. Therefore, the operation of centrifugal fans involves a combination of centrifugal force effects and the deflection of airflow from a radial direction to a spiral flow pattern at the circumferential cross-sectional area, with the blade tip playing a significant role. This flow deflection effect greatly impacts the performance and flow pattern of forward-curved blade fans. In contrast, the predominant effect in backward-bladed fans is the centrifugal force [66].

Centrifugal fans equipped with (BC) demonstrate moderate pressure increase, placing them between forward and radial blade configurations. Nevertheless, they offer the best efficiency compared to these alternatives due to minimal alterations in fluid direction as it enters and exits the blade passages [68]. Fan efficiency is evaluated using Equation 3.1, where efficiency stands as a critical performance metric.

$$\eta_{t/s} = \frac{Q \, \Delta P_{t/s} \, T}{M \, 2\pi} \tag{3.1}$$

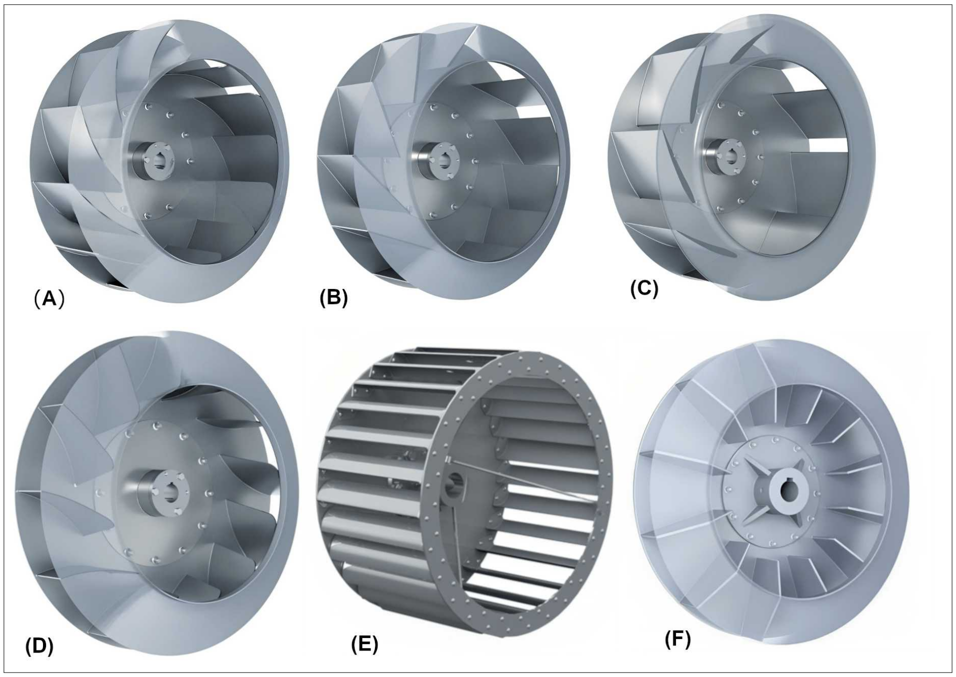

Figure 3.1: Main types of centrifugal Fans; (A) Backward Curved,(B) Backward Inclined,(C) Airfoil,(D) Radial Tip,(E) Forward Curved,(F) Radial Blade [67].

$$\Delta P_s = P_{out} - P_{in} \quad ; \quad \Delta P_t = (P + \frac{\rho\, v^2}{2})_{out} - (P + \frac{\rho\, v^2}{2})_{in} \tag{3.2}$$

where: Q is the volume flow rate, M is the total torque, T is the impeller period, $\Delta \mathrm{P_s}$ is the static pressure rise.$\Delta \mathrm{P_t}$ is the total pressure rise, ρ is the fluid density, v is the fluid velocity. (η_t) is the total efficiency calcultaed using ΔP_t, while the static efficiency (η_s) is calcultaed using ΔP_s.

Centrifugal fans equipped with BC and BI blades were once renowned for their efficiency, but they were surpassed by AF centrifugal fans. AF fans are often considered the top-tier option among centrifugal fans. They share a similar design to BC and BI fans, featuring hollow airfoil steel blades that give them exceptional structural strength, allowing them to run at higher rotational speeds. Nevertheless, they are typically employed for applications involving clean air [65]. AF fans exhibit stable performance and achieve the highest efficiencies among all fan types, typically reaching efficiency levels of around 85% [69].

Centrifugal fans featuring forward-curved blades, also known as Squirrel cage fans or Sirocco fans, typically consist of numerous blades with small surface areas curved in the direction of rotation. These fans are commonly used in low-pressure applications and operate at lower speeds compared to other fan types [70]. Centrifugal fans with forward-curved blades excel at generating a constant high static pressure across a broad range of volume flow rates. However, this advantage comes with the trade-off of lower maximum efficiency when compared to their backward-curved (BC) and backward-inclined (BI) counterparts. They serve as a cost-effective but less efficient alternative in scenarios where a more expensive and efficient airfoil fan (AF) is warranted. Nevertheless, it's essential to note that forward-curved (FC) fans are not suitable for applications involving dusty or fume-laden air streams. Due to the shorter blade length and curvature, they tend to accumulate dirt and allow particulates to adhere to their surfaces, leading to potential balance issues.

When contrasted with squirrel cage fans, backward-curved blade fans feature a reduced number of blades, each with a more larger surface area, and the relative velocity at the trailing edge (V_{2r}) opposes the direction of rotation. This distinction results in a non-overloading characteristic for backward-curved blade fans, making them well-suited for applications with highly variable load conditions [70]. However, it's worth noting that backward-curved blade fans experience high circulatory flow losses due to the non-uniform tangential component (V_t) of the absolute velocity vector, which decreases in the gaps between blade passages and on the circumferential cross-sectional area at the outlet. Conversely, forward-curved blade fans with numerous blades lead to excessive flow blockage losses, also known as passage losses, which in turn reduce the fan's net head and efficiency [68].

Centrifugal fans equipped with radial blades, exhibit a straightforward and uncomplicated geometry. The blades extend directly from the shaft, with a greater depth, while the rotor tends to be relatively narrow in comparison to its diameter. This design allows this type of fan to generate the highest pressure rise among the three fan types across a wide range of volume flow rates. However, it's essential to note that they are the least efficient option, and their pressure rise exhibits a rapid decline after reaching the point of maximum efficiency [68].

Radial and backward-curved centrifugal fans are the choice for situations requiring a narrow range of volume flow rates and pressure rises. However, if a broader range in volume flow rates and pressure rises are necessary, the capabilities of radial fans and backward-curved fans might not align with the updated demands [68].

3.2 Cement Production Process and Fan Systems: A Comprehensive Overview

The cement industry is not only a cornerstone of a country's economic development but also a critical sector in the global construction and infrastructure landscape. This industry involves a series of well-defined steps, starting with the mining of essential raw materials, These raw materials are then processed and milled to form a homogenous mixture. Subsequently, the next stage involves subjecting this mixture to high temperatures in a kiln, which leads to the formation of clinker, a vital intermediate product in cement manufacturing. This clinker is then finely ground along with various additives to produce the final cement product (refer to Fig.3.2).

The cement production process initiates at the quarry, where raw materials like limestone, clay, and sand are extracted, gathered, and transported. After crushing and milling, these raw materials are refined into a gravel-like substance known as raw meal. These components are blended with other substances in specific mineral proportions. Following this, the raw meal undergoes high-temperature treatment in a kiln, inducing a chemical reaction that results in the formation of clinkers. However, prior to this stage, a preheating process of the feed material is essential. This is achieved by utilizing the hot gases emitted from the kiln process, necessitating the use of a preheater ID-Fans to ensure a continuous flow of these gases.

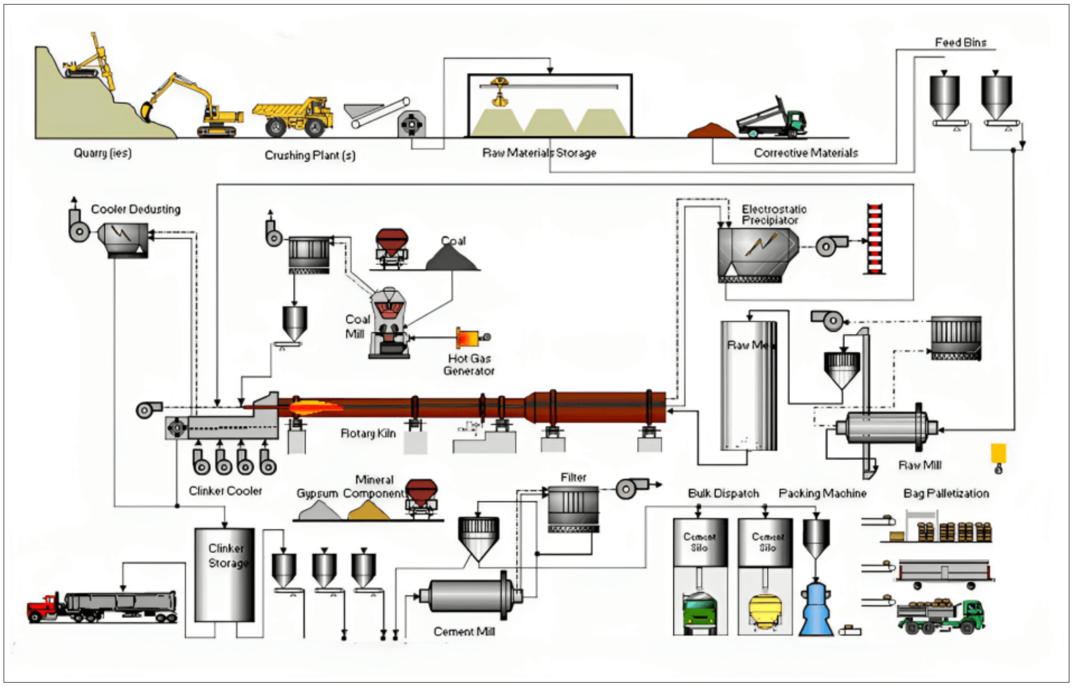

Figure 3.2: Cement manufacturing process.

The most efficient choice for a preheater-ID Fan used in the preheating process is the backward-curved blade design. However, it's important to note that this blade design comes with a potential issue of material accumulation on the blade's suction side, which can lead to a significant imbalance and rotor vibration. This problem is linked to the blade's concave shape, which causes flow separations near the blade surface. Within these areas, the boundary layer experiences low-velocity conditions, allowing materials to settle and build up. In contrast, when employing RB design, this concern about material accumulation is not present. RB design offers the advantage of being highly efficient at self-cleaning and preventing material buildup. The only design more efficient in this regard would be a full airfoil blade, but it comes with the risk of severe erosion [71].

In the Kiln process, calcium carbonate (in the form of limestone) undergoes a series of transformations and reactions with other components. These reactions result in compounds that partially fuse at extremely high material-burning temperatures, which can reach up to 1450°C [72]. Throughout this phase, Forced Draft Fans are responsible for providing the necessary air supply for fuel combustion, while induced-draft Fans ensure the flow of exhaust gases. As the Kiln process nears its conclusion, the clinker reaches an exceptionally high temperature. To preserve the quality of the clinker, a cooling process is implemented, designed to lower the clinker's temperature from its exit point at around 1200°C to less than 100°C.

This cooling process is achieved through a continuous airflow facilitated by the use of clinker coolers and exhaust fans. Consequently, the fans employed in cement plants must meet fundamental requirements for reliability and durability, given the continuous and demanding nature of the production cycles.

After completing the cooling process mentioned earlier, the subsequent step is to acquire the clinker product. This clinker is then subjected to the subsequent grinding stage. In this grinding process, gypsum and other essential additives are introduced to produce the end product: cement. The details of this process phase are elaborated on in the following section.

3.2.1 Role of the FN-280 Centrifugal Fan in the Cement Mill Process

The cement milling process utilizes a variable-capacity Raw-mill for material handling. To manage this process efficiently, a dust collector is utilized to capture and collect the dust carried by air during this process. The collected dust is then reintroduced into the final product, while clean air is discharged through a chimney into the environment.

The clinker grinding system in the past has typically depended on ball mills, whether used in open-circuit setups or in conjunction with separators in closed-circuit configurations. However, the challenge of achieving low milling efficiency has prompted the introduction of more energy-efficient alternatives. These alternatives encompass combinations of ball mills with separators, high-pressure roll presses, vertical roller mills, direct grinding high-pressure roll presses, and horizontal roller mills, often referred to as horomills [73]. Figure 3.3 provides a representative schematic flow of a closed-circuit ball mill system with two compartments (mechanical and static separator).

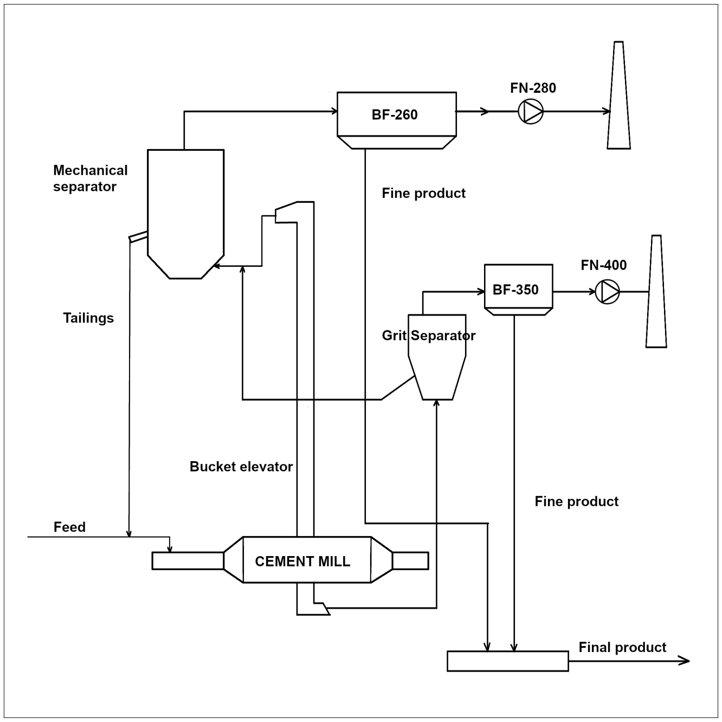

Figure 3.3: Cement-milling process.

Achieving the desired fineness and particle size distribution in the cement grinding system is controlled by adjusting the separator. In cement mill setups, various separator types are used. The primary goal is to minimize the entry of fine particles below the desired size into the tailings and vice versa. Within the separator, mixed particles enter a classification zone where they experience centrifugal and air drag forces. Depending on the direction of these forces, particles are sorted into coarse or fine streams.

Static separators also referred to as grit separators, operate by utilizing cyclonic airflow generated through the use of guide vanes. Fine products are steered into a smaller cyclone due to air pressure, while the coarser materials are sent back to the mill. A baghouse system with large filters and tubular bags (BF-350) is employed to eliminate dust particles produced during the grinding process. These bags are designed to capture particles as small as 45 μm, which can be considered a final product (see Figure 3.3). Induced draft fans (FN-400) aid in moving dust-laden air (depicted in Figure 3.4) through a sequence of fabric bags before it returns to the cement silo for storage. Despite these enhancements, static separators still fall short of achieving an efficiency level of 70% [73].

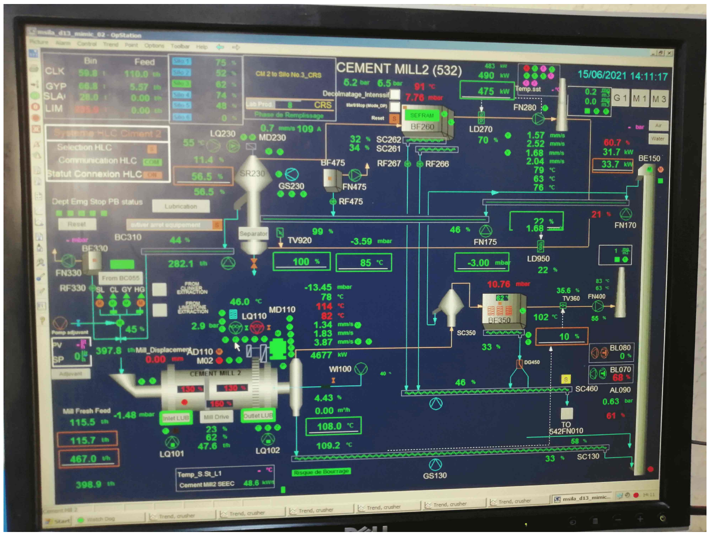

Figure 3.4: FN-280-PROCESS

In contrast, mechanical separators feature a rotating distribution disc designed to evenly distribute feed particles within the classification zone. This design incorporates a centrally driven fan that ensures the necessary air circulation, an auxiliary fan, a system for returning air to reclassify tailings, and a product discharge cone. The setup's configuration can be observed in Figure 3.3. The coarser product, known as tailings, is reintroduced at the mill's feed end. On the other hand, the finer material, matching the desired product size, is conveyed to the Bag-Filter (BF-260) for a dedusting process, which is effectively achieved with the assistance of the centrifugal fan (FN-280).

Subsequently, this finely ground material is directed to the product silo for storage [73].

Fans employed within cement plants are typical of the centrifugal fan type, with options including single or double inlet configurations [69]. These fans can feature blade designs of either a profiled shape or a single-thickness plate. Furthermore, variable speed systems are frequently utilized to enhance their operational flexibility. In the context of cement plants, centrifugal fans play a pivotal role in the exhaust system, with a particular emphasis on the dedusting stage. Their primary function is to extract dust-laden air originating from the cement mill and subsequently convey it to the bag filter. This process serves the dual purpose of effectively removing particulates and facilitating material handling in the dedusting procedure.

The dust collector is typically comprised of a bag of filters, typically positioned before the fan's inlet. The filter bags are constructed from materials specifically designed to capture and retain fine particles, ensuring that the air entering the fan is clean and free from particulate matter. This collector consists of a series of fabric bags or cartridges arranged within a housing, allowing the airstream to pass through them. Despite the presence of the bag filter, it is possible for some particles to find their way into the fan. This can occur due to various factors, including potential bag leaks, insufficient maintenance, or variations in operating conditions. In this process, the air stream's circulation is facilitated by Induced Draft Fans, also known as Cement-mill Fans. These fans are crucial for generating a negative pressure flow, which is essential for the efficient operation of the dedusting process. Figure 3.5 provides a visual representation of a cement mill fan installed on-site.

Figure 3.5: Exterior View of the FN-280 Centrifugal Fan in Cement Milling process

The fan under investigation ,FN-280, is a single-inlet centrifugal fan. The fan's impeller is equipped with 16 backward-curved S-shaped blades and operates at a rotational speed of N = 985 rpm. The reference velocity pressure (p_{ref}) based on the impeller tip speed U_2, is equal to 5459.04 Pa. The corresponding rotational frequency (RF) and impeller period (T) are calculated as RF = N/60 = 16.41 Hz and T=1/RF = 0.060913s, respectively. The aerodynamic performance of the studied fan was experimentally derived in accordance with the industrial fan testing standard ISO 5801 requirements [74]. Table 3.1 provides the most important fan design specifications.

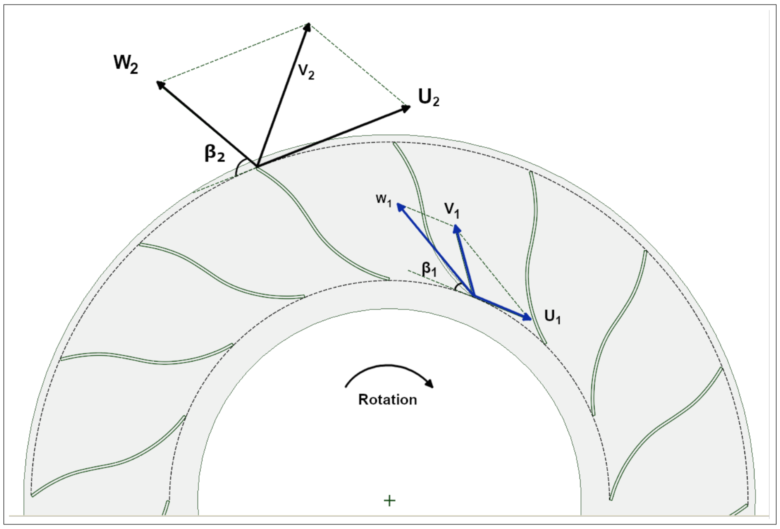

Figure 3.6: Illustration of theoretical velocity vector diagrams in FN-280.

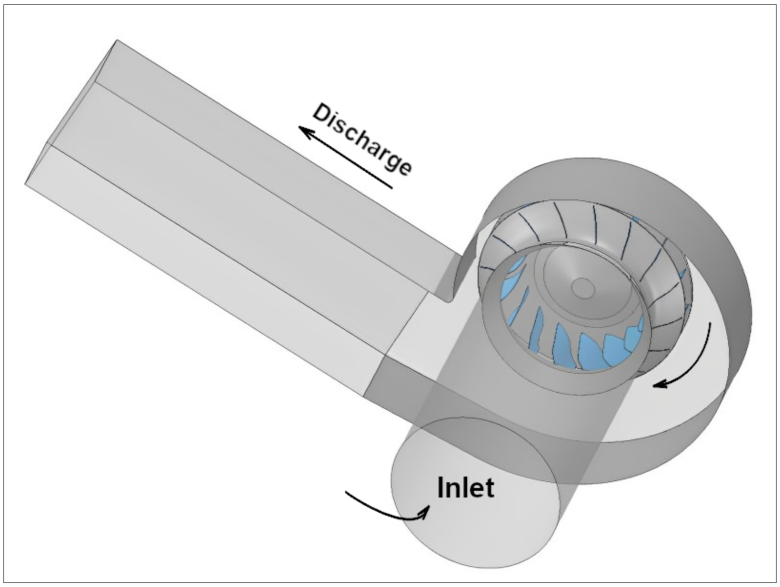

Figure 3.7: Backward-Curved S blade fan design.

Main parameters	value
Impeller outlet diameter, D_2	2240 (mm)
Impeller inlet diameter, D_1	1190 (mm)
Volute width	900 (mm)
Impeller blade count	16
Blade thickness	8 (mm)
Rotational speed, N	985 (rpm)
Impeller tip speed, U_2	115.46 (m/s)
Impeller outlet blade span	280 (mm)
Impeller-tongue gap	110 (mm)
Q_d (design flow rate)	53.9 (m^3/s)
ΔH_d (design Total pressure rise)	6148 (Pa)

Table 3.1: Main design parameters of the fan.

3.3 Reverse Design Engineering: Reconstructing the Blade CAD

3.3.1 Overview

In this study, a technique known as reverse design engineering was utilized to overcome the specific challenge of recreating the blade CAD model of the centrifugal fan. Reverse engineering involves the creation of a geometric model of an existing part using 3-D point data acquired through scanning, without the need for detailed technical specifications like drawings.

The blade design is certainly a pivotal factor that significantly influences various flow parameters, including pressure distribution, velocity profiles, turbulence characteristics, and, ultimately, the overall performance of the fan. Conducting CFD simulations required the availability of the original fan geometry in CAD format. While the drawings of the fan components such as the casing and the rotor were available, the blade design was the missing piece. Given the absence of the original blade drawings, reverse engineering the blade's design became the preferred approach. For regular and straightforward shapes, the manual reverse engineering method using primitive geometries, where part data is acquired through manual measurements, is a feasible process. However, as the complexity of the object's shape increases, this approach demands considerable effort. In cases where basic primitive parts are no longer suitable, especially for free-form surfaces, a more specialized approach becomes necessary [75]. To tackle this challenge effectively, we opted for reverse design engineering with the aid of a Coordinate Measuring Machine (CMM). The primary objective was to reconstruct the blade's CAD model in a manner that accurately replicated the original design. This was vital to ensure the precise alignment of the reconstructed blade CAD model with the remaining fan components.

Through this overview, we have established the rationale and significance of utilizing reverse design engineering to ensure the exact replication of the original fan design. This sets the stage for the subsequent subsections, we give insight into the specific aspects of the reverse design engineering process, where we walk through the process of obtaining the CAD model of the impeller blade through the application of obtaining point cloud by using CMM and reconstructing the CAD model of the blade using software tools that can handle scan data.

3.3.2 Reverse design Methodology

Reverse Design is a technology that converts 3D scan data of a physical object into a Computer-Aided Design (CAD) model, facilitating its use in manufacturing. The process typically involves three phases: Data Acquisition (scanning), Preprocessing, and Geometric Model Development (Figure 3.8). These phases may overlap, depending on project requirements [76].

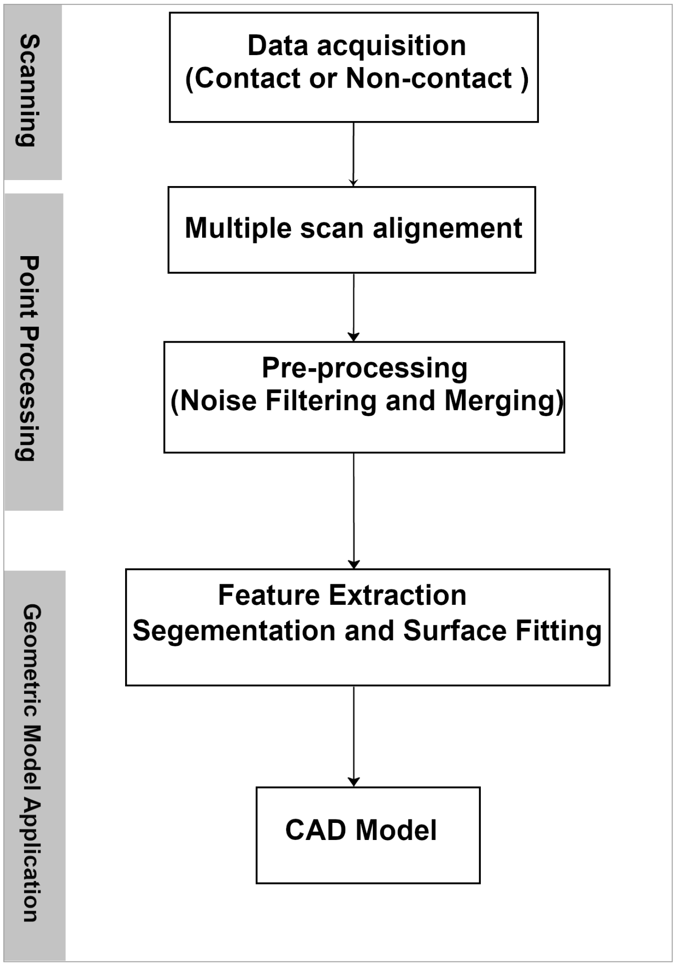

Figure 3.8: Reverse engineering Process

- Scanning Phase:

  The scanning phase involves gathering data from the 3D surface of an object. In this phase, the scanning process begins with a strategy that includes selecting and preparing the part for scanning, followed by the actual scanning operation. The aim is to capture the main solid body and all the geometrical features of the object, including details such as Gussets, steps, slots, Ribs, holes and Angles. This is typically achieved by recording numerical data in the form of 3D coordinates, resulting in point cloud matrices. During the scanning process, 3D scanners equipped with probes are utilized to move across the part's surface. Two primary types of scanners are distinguished: contact scanners and non-contact scanners. Contact scanners, often integrated with Coordinate Measuring Machines (CMMs), employ contact probes that automatically trace the physical surface contours. In contrast, non-contact scanners collect data without any physical contact with the part. They use lasers, optics, and charge-coupled device (CCD) sensors for data capture. Non-contact scanners excel in collecting substantial data in a relatively short time compared to contact scanners. However, they have a wider tolerance range, making them less suitable for surfaces parallel to the laser's axis or exceptionally shiny surfaces. The choice between contact and non-contact scanning methods depends on the specific requirements and challenges of the object being scanned.

- Point cloud Processing Phase:

  The Point Cloud Processing Phase in reverse design engineering is a crucial step in which the collected cloud data is imported and refined. This phase serves to enhance the data's quality. It involves several key tasks, including noise reduction and downsizing the number of data points. To achieve these objectives, various predefined filters are applied. Moreover, this phase facilitates the integration of multiple scan data sets, especially when it's necessary to capture all essential features of the part accurately. The ultimate goal is to produce a well-organized, noise-free, and merged point cloud data set in a convenient format, setting the stage for subsequent stages in the reverse engineering process [75].

- Application Geometric Model Development Phase:

  Generating CAD models from point data represents a challenging task in reverse surface engineering (RE). This complexity arises from the need for powerful surface-fitting algorithms that can accurately translate the 3D point cloud data sets into CAD models [77]. The outcome of this phase typically results in a geometric model in one of the various formats such as IGES, VDA, STL, DXF, OBJ, VRML, etc. The nature of this phase depends significantly on the specific objectives of the reverse engineering project.

3.3.3 Impeller Blade Reverse Design workflow

- **Scanning and post-processing phase of the blade :**

  In our case, the Coordinate Measuring Machine (CMM), depicted in Fig 3.9, employed for gathering point cloud data is of bridge type. It features a measurement range of (X=1.2m, Y=1.9m, Z=1m), and a precision of 1µm in the X, Y, and Z-axis. The CMM operates by generating 3-D coordinate points as its probe traverses the part's surface. Operators have the flexibility to operate the CMM manually, where they manipulate the probe to collect coordinate measurements by hand, or they can utilize programmed sequences to automate the probe's movement across the part [78].

  The resulting 3-D scan data comprises both a point cloud and a mesh. The point cloud represents a collection of three-dimensional vertices, where each vertex corresponds to a specific location on the blade's surface. In contrast, the mesh is composed of vertices, edges, and faces. The transformation of the point cloud into a mesh is executed by the scanning embedded software, PC-DMIS, integrated into the Coordinate Measuring Machine (CMM).

  To begin the scanning process, it is crucial to prepare the workspace. Blade alignment involves the alignment of both the CMM's coordinate system and the blade, as illustrated in Figure 3.10. The data collection occurs through a mechanical method utilizing a touch-trigger probe. This probe acquires data by making contact with the surface along the entire part's profile, ensuring a continuous stream of data. Consequently, the selection of the probe, control of its position, the trajectory it follows, and the angle at which it engages with the surface all hold significant importance during the scanning phase.

Figure 3.9: Coordinate Measuring Machine (CMM) for 3D Scanning in the Scanning Phase.

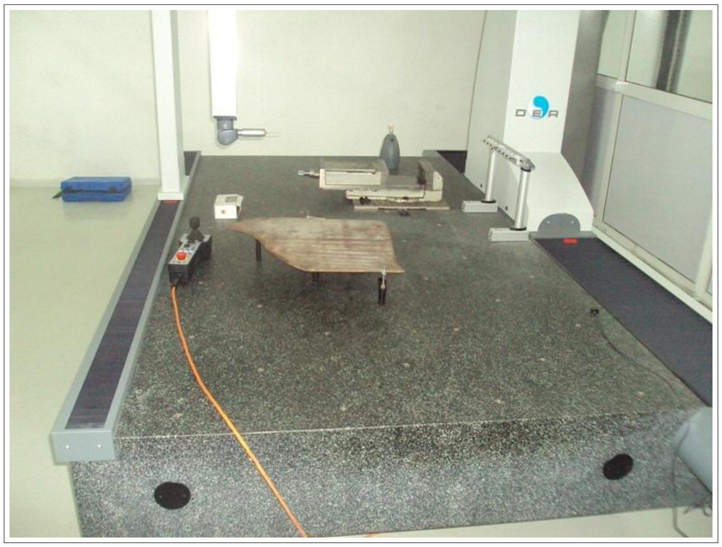

Figure 3.10: Blade alignment.

All information collected during the scanning is converted into digital data (point cloud data) through (PC-DMIS) software. Raw scan data is essentially unprocessed information, and it's essential to optimize the mesh before utilizing the 3D scan data generated by the scanning machine. In our case, we employed the features offered by Geomagic Design X for this purpose to ensure global mesh optimization. Figure 3.11-b provides a visual representation of the blade's point cloud data after undergoing the optimization process.

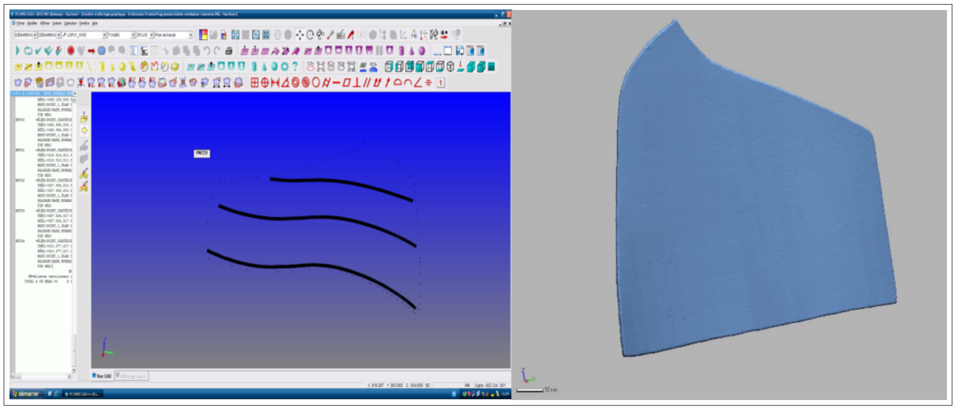

Figure 3.11: (a) the trajectory of the cloud data obtained according to the PC-DMIS software,(b) Optimized point Cloud data of the blade.

- **3D scan data to CAD model Conversion:**

  The collected data, represented in the form of a point cloud, lacks critical topological information, making it unsuitable for downstream applications. As a result, it's often necessary to process and transform this data into a more usable format. This typically involves converting it into a triangular-faced mesh or a set of NURBS surfaces, depending on the specific requirements of the reverse design process. The approach chosen for reverse modeling depends on various factors, including the type of scan data, the complexity of the model's shape, and the design objectives. In the case of the FN-280 fan blade section, where non-uniformity and surface deformities are present due to the nature of the blade, a Hybrid modeling approach is employed. This approach combines parametric modeling with surface fitting methods to effectively address the specific challenges posed by the scan data.

Mesh segmentation, most important in reverse modeling engineering, is a multifaceted process that involves breaking down the original data points into distinct subsets associated with specific primitive surfaces. Typically, this segmentation process relies on estimating both first- and second-order surface properties. The first-order segmentation, primarily guided by surface normal vectors, serves as an initial division of the surface and is effective in identifying sharp edges and distinguishing flat or highly curved areas. The second-order segmentation, on the other hand, subdivides the surface based on principal curvatures, providing a solid foundation for categorizing simple algebraic surfaces [79]. To facilitate this process, as illustrated in Figure 3.12, mesh regions on the surface mesh of the blade's pressure and suction sides are defined. This segmentation is performed to enable the application of surface fitting techniques in subsequent steps.

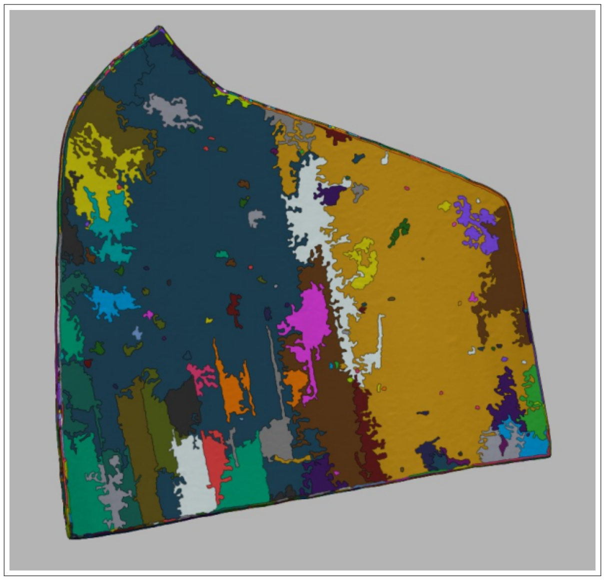

Figure 3.12: Partitioning the Blade Surface into Mesh Regions for Pressure and Suction Sides.

The application of surface fitting technology is a powerful method for constructing freeform surfaces based on specific regions within a mesh [80]. The Mesh Fit tool was used to generate surfaces for both the blade's suction and pressure sides. As depicted in Figure 3.13-a, these surfaces were created with an allowable deviation set at 0.0008mm, using 70 control points to enhance control over Iso-lines while minimizing smoothness, ensuring maximum coverage of the entire mesh region. Figure 3.13-b illustrates the deviation from the mesh, demonstrating that it falls within an acceptable range.

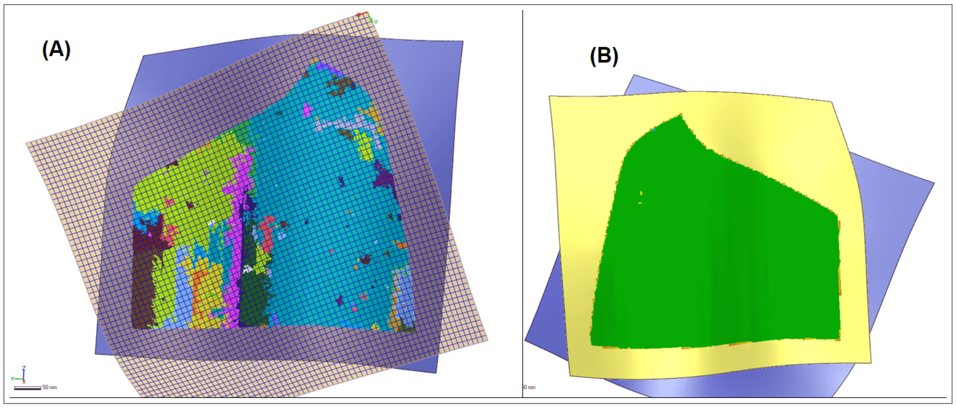

Figure 3.13: surface fitting of pressure and suction side.

We generated a three-dimensional mesh sketch curve with nodes exclusively connected to concave mesh areas. Subsequently, we created an offset curve with a width of 0.03mm to produce the surface sections for both the shroud and the leading edge. The deviation of the mesh, assessed with the accuracy analyzer, and the resulting surfaces are presented in Figure 3.14.

The impeller CAD model is ultimately derived by trimming all the generated surfaces and planes. To ensure the model's accuracy, an accuracy analyzer is employed to monitor its deviation from the mesh model. Figure 3.15 illustrates all the surfaces and planes involved in the CAD model creation process, and the final CAD model of the impeller blade. In summary, the application of reverse design engineering offered a viable solution for recreating the centrifugal fan blade's CAD model when the original blade drawings were unavailable.

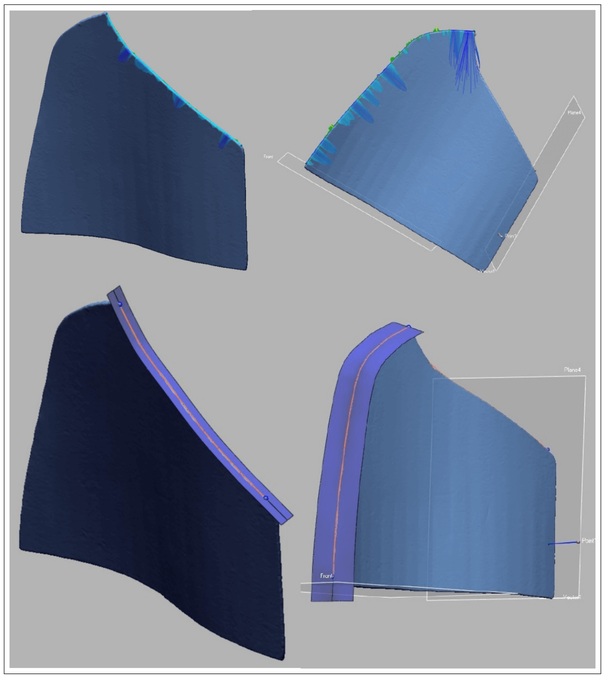

Figure 3.14: surface-cut of the blade tip and leading edge.

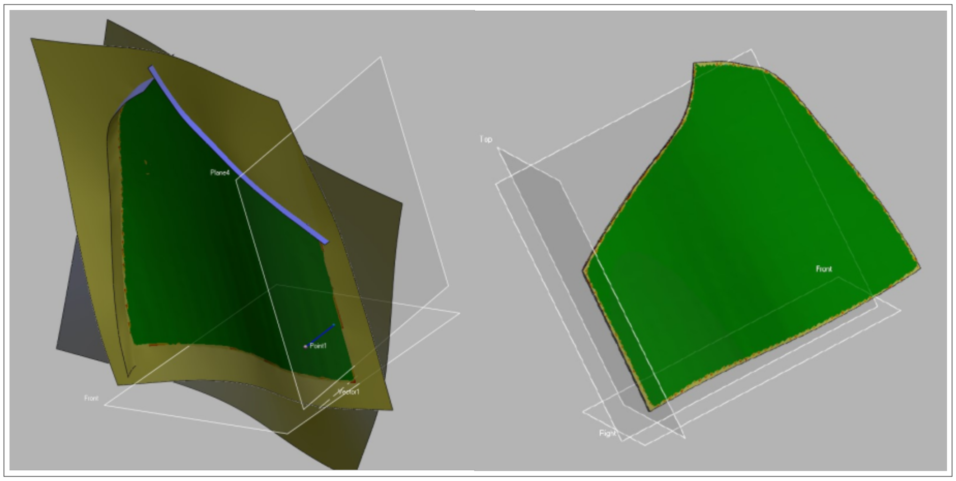

Figure 3.15: Final CAD model of the blade.

Chapter 4

CFD methodology of multiphase flows

The process of understanding any physical phenomenon commences with the meticulous selection of suitable fundamental physical principles, which is subsequently applied to a relevant physical model. This procedure culminates in the formulation of governing equations that faithfully represent and elucidate the fundamental physical processes. In the realm of real-world fluid dynamics, even when dealing with apparently straightforward geometries, the complexities involved often render analytical solutions unattainable. The use of analytical techniques proves inadequate in addressing the intricacies of these systems. Consequently, a numerical approach, such as CFD, is not merely beneficial but indeed a must for gaining insights and predicting behavior in such scenarios. CFD, a numerical simulation method, uses the computational capabilities of modern computers to solve the differential equations governing fluid dynamics. This technique offers a tool to acquire valuable insights into fluid behavior in diverse applications, such as turbulence, multiphase flows, and heat transfer. this is achieved by discretizing the domain into smaller computational elements and solving a system of equations iteratively. using CFD enables us to effectively bridge the gap between complex real-world fluid dynamics and our ability to analyze and predict their behavior.

In CFD, obtaining numerical solutions typically involves two main steps. First, we formulate Partial Differential Equations (PDEs) based on fundamental conservation principles. Second, generating the geometry and discretizing the computational domain, setting up boundary conditions, and applying numerical methods to find solutions to these equations. Furthermore, when analyzing particle-laden flows for erosion prediction with CFD, we break the process down into three submodels: flow field solving, tracking particle trajectories, and Erosion Modeling [8].

In this chapter, we begin by exploring the foundational equations that govern the behavior of turbulent fluid flows, encompassing discussions on turbulence modeling. Subsequently, we delve into the intricacies of modeling particle-laden flows. To solve the flow field and predict particle dispersion through the fan domain, CFD solver of the continuous phase and Lagrangian transport model were employed. For the CFD solver, the commercial CFD software ANSYS-CFX was used, while grid generation was conducted by ICEM-CFD. Our investigation covers an assessment of the impact of different boundary conditions, encompassing considerations of time-stepping, grid refinement, and the number of particles released.

4.1 Governing Equations of fluid motion

4.1.1 Conservation principles

The underlying principles governing the physical aspects of fluid flows are the conservation of mass, momentum, and the conservation of energy. These foundational principles are typically represented through mathematical equations, taking the form of partial differential equations [81]. These conservation laws are derived by considering a fixed amount of matter referred to as the Control system (CS) and encompassing extensive properties. This approach is well-suited for particle mechanics, where identifying the control system is straightforward. However, in the context of continuous media like fluids, comprising an infinite number of particles and undergoing continuous deformations due to shear stress, it becomes impractical to track individual particles or matter parcels as they evolve.

To address this challenge, a more practical strategy, known as the control volume approach, is to focus on the flow within a specific spatial region referred to as a control volume (CV) instead of monitoring individual parcels passing through the region of interest [82]. To effectively analyze fluid flows, it is essential to express all the conservation equations, originally developed for fixed mass and identity (CS), in terms of the relevant physics applicable to a control volume (CV).

The mass and momentum conservation equations in the (CS) can be expressed as:

$$\frac{dm}{dt} = 0 \tag{4.1}$$

$$\frac{d(m\mathbf{v})}{dt} = \sum \mathbf{F} \tag{4.2}$$

The transformation of the conservation equation from CS form to CV form is given by the Reynold transport theorem (RTT), which can be written as:

$$\left[\frac{d\Phi}{dt}\right]_{cs} = \frac{\partial}{\partial t}\int_{V_{CV}} \rho\,\phi\,dV + \int_{S_{CV}} \rho\,\phi\,(\mathbf{v_r}.\mathbf{n})\,dS \tag{4.3}$$

Where ϕ in Equation 4.3 is an intensive property. ϕ represents the conserved property per unit mass. This equation signifies that the rate of change of the property within a System is equal to the rate of change of the property within the CV, in addition to the net flux of the property across the S_{CV}, which is commonly referred to as the convection or advection term. The extensive property, denoted as Φ, can be defined as:

$$\Phi = \int_{V_{cv}} \rho\,\phi\,dV \tag{4.4}$$

Where: V_{CV} represents the volume occupied by the control volume (CV), S_{CV} is the surface that encloses the CV, and 'n' is a unit vector oriented outward and normal to S_{CV}. V_r denotes the fluid velocity relative to the moving CV.

1. Conservation of Mass

The integral form of the continuity equation can be derived directly from the RTT by substituting ϕ with 1:

$$\frac{\partial}{\partial t}\int_{V_{CV}} \rho\,\phi\,dV + \int_{S_{CV}} \rho\,\phi\,(\mathbf{v_r}.\mathbf{n})\,dS = 0 \tag{4.5}$$

By transforming the surface integral of the convection term into a volume integral using Gauss' divergence theorem for any choice of CV and for a non-deformable CV, the integral form gives a differential coordinate-free form of the continuity equation :

$$\frac{\partial \rho}{\partial t} + \nabla \cdot (\rho \mathbf{v}) = 0 \tag{4.6}$$

2. Conservation of Momentum

When the control system and the control volume coincide as the time interval tends to zero, using (Eq. 4.2) and replacing ϕ by $\mathbf{v}$ in (Eq. 4.3) leads to the following expression:

$$\sum_{CV} \mathbf{F} = \frac{\partial}{\partial t}\int_{V_{CV}} \rho\,\mathbf{v}\,dV + \int_{S_{CV}} \rho\,\mathbf{v}\,(\mathbf{v_r}.\mathbf{n})\,dS \tag{4.7}$$

where the right-hand side is the total external forces acting on the CV, and the intensive property $\mathbf{v}$ is expressed in a stationary reference frame. the total force that may act on the control volume can be classified as surface forces and body forces.

- Surface forces that act on the S_{CV} arise from the pressure exerted by the surrounding fluid on the CV. Secondly, they result from the stress distributions, including shear and normal stress, resulting from the friction between the fluid and the CV's surface. On a molecular scale, these surface forces due to pressure and stresses represent microscopic momentum transfers across a surface [82].
- External body forces are distributed over the extent of the volumetric mass of the fluid element, such as gravitational, buoyancy, Coriolis, electromagnetic forces, etc.

by applying Cauchy's law, the integral form of the momentum conservation equation becomes:

$$\int_{S_{CV}} \tau \cdot \mathbf{n}\, ds + \int_{S_{CV}} \rho\, \mathbf{b}\, dV = \frac{\partial}{\partial t} \int_{V_{CV}} \rho\, \mathbf{v}\, dV + \int_{S_{CV}} \rho\, \mathbf{v}\, (\mathbf{v_r}.\mathbf{n})\, dS \tag{4.8}$$

where $\mathbf{b}$ is the body forces per unit mass, τ is the viscous stress tensor which maps the outward normal vector of a surface to the traction vector acting on that surface. the differential form of the dynamic equilibrium (Navier's equation) in a coordinate-free form is obtained by applying Gauss' divergence theorem to the convection and diffusion flux terms:

$$\frac{\partial(\rho \mathbf{v})}{\partial t} + \nabla \cdot (\rho \mathbf{v}\mathbf{v}) = \nabla \cdot \tau + \rho \mathbf{b} \tag{4.9}$$

In most cases of interest where fluid can be regarded as a continuum, the stress tensor can be divided into the hydrostatic and deviatoric parts. For a special case of Newtonian fluids, the deviatoric part of the stress tensor should be a linear function of the rate of deformation tensor D_{ij} [83]. under the assumption of Homogeneous fluid, isotropic fluid and Newtonian fluid and the viscous stress tensor τ, can be written:

$$\tau_{ij} = -p + \lambda \frac{\partial u_k}{\partial x_k} \delta_{ij} + 2\mu D_{ij} \tag{4.10}$$

In (Eq. 4.10), δ_{ij} is the Kronecker delta function ($\delta_{ij} = 1$ if $i = j$ and $\delta_{ij} = 0$ if $i \neq j$), P is the static pressure and D_{ij} is the rate of deformation tensor defined as follow:

$$D_{ij} = \frac{1}{2} \left(\frac{\partial u_i}{\partial u_j} + \frac{\partial u_j}{\partial u_i} \right) \tag{4.11}$$

Using the continuity (Eq. 4.6) and substituting equation 4.11 and equation 4.10 in equation 4.9 yields the Non-conservative Navier equations form:

$$\rho \frac{Du_i}{Dt} = -\frac{\partial p}{\partial x_i} + \frac{\partial}{\partial x_i} \left[(\lambda + \mu) \frac{\partial u_k}{\partial x_k} \right] + \frac{\partial}{\partial x_j} \left(\mu \frac{\partial u_i}{\partial x_j} \right) + \rho\, b_i \tag{4.12}$$

The Stokes hypothesis states that the mechanical pressure is identical to the thermodynamic pressure. the mechanical pressure P_mech is given as follows:

$$p_{mech} = -p + \left(\lambda + \frac{2}{3}\mu\right)\frac{\partial u_k}{\partial x_k} \tag{4.13}$$

for p_{mech}=p this implies that $\lambda = -\frac{2}{3}\mu$. the use of Stokes' hypothesis yields the Navier-stokes equations in a cartesian coordinate:

$$\rho\frac{Du}{Dt} = \frac{\partial}{\partial x}\left[-p + \frac{\mu}{3}\frac{\partial u_k}{\partial x_k}\right] + \frac{\partial}{\partial x}\left(\mu\frac{\partial u}{\partial x}\right) + \frac{\partial}{\partial y}\left(\mu\frac{\partial u}{\partial y}\right) + \frac{\partial}{\partial z}\left(\mu\frac{\partial u}{\partial z}\right) + \rho b_x \tag{4.14a}$$

$$\rho\frac{Dv}{Dt} = \frac{\partial}{\partial y}\left[-p + \frac{\mu}{3}\frac{\partial u_k}{\partial x_k}\right] + \frac{\partial}{\partial x}\left(\mu\frac{\partial v}{\partial x}\right) + \frac{\partial}{\partial y}\left(\mu\frac{\partial v}{\partial y}\right) + \frac{\partial}{\partial z}\left(\mu\frac{\partial v}{\partial z}\right) + \rho b_y \tag{4.14b}$$

$$\rho\frac{Dw}{Dt} = \frac{\partial}{\partial z}\left[-p + \frac{\mu}{3}\frac{\partial u_k}{\partial x_k}\right] + \frac{\partial}{\partial x}\left(\mu\frac{\partial w}{\partial x}\right) + \frac{\partial}{\partial y}\left(\mu\frac{\partial w}{\partial y}\right) + \frac{\partial}{\partial z}\left(\mu\frac{\partial w}{\partial z}\right) + \rho b_w \tag{4.14c}$$

4.2 Turbulence modeling

In both engineering applications and everyday life, various types of flows, ranging from simple ones to more complex three-dimensional flows, undergo a transition to an unstable state, deviating significantly from laminar flows. This transition is characterized by a state of motion marked by a chaotic change over time and position of flow properties [84]. The pioneering research on turbulence dates back to 1883 when Osborne Reynolds conducted systematic experiments on pipe flow. His investigations revealed that flow becomes turbulent or irregular when the nondimensional Reynolds number ($Re = UL/\nu$) exceeds a critical value, denoted as Re_{crit}. This parameter, describing the relative significance of inertia forces compared to viscous forces in a flow, has since been established as the key factor determining the dynamic similarity of viscous flows [85, 86].

In experimental observations of fluid systems, when the Reynolds number (Re) remains below Re_{crit}, fluid flows are laminar, where adjacent fluid layers slide past one another in an orderly fashion, and the flow remains steady as long as the boundary conditions remain constant. However, when the Reynolds number surpasses the critical threshold, a complex sequence of events unfolds, eventually leading to a radical alteration in the flow's nature. The motion inherently becomes unsteady, even when boundary conditions are consistently applied. All flow properties exhibit random and chaotic variations, as exemplified in Figure 4.1, which illustrates the time history of the instantaneous velocity component, denoted as U. The horizontal line represents the mean velocity, symbolized as $\overline{U}$. Notably, the velocity U displays substantial fluctuations around $\overline{U}$, and the time history exhibits variations across a wide range of timescales, rather than following a periodic pattern.

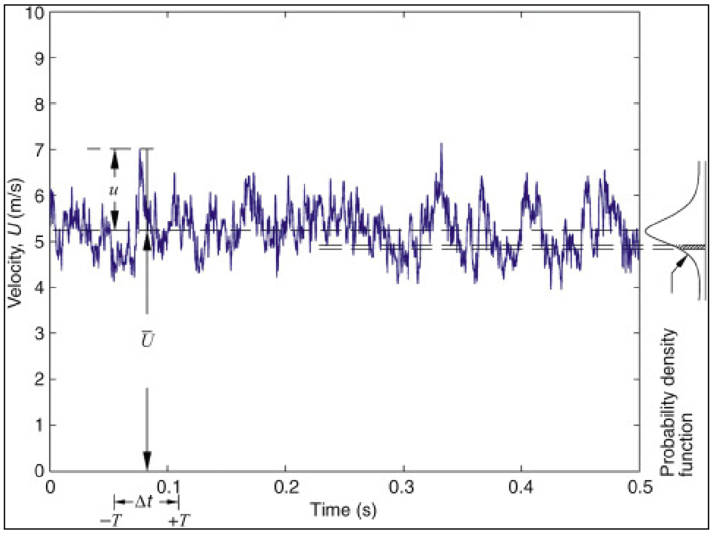

Figure 4.1: Time history of the velocity fluctuations about the mean value [1]

Turbulent flow is distinguished by the efficient transport and mixing of fluids. this feature is of prime importance in many applications involving fluid stream mixing. Turbulence is also effective at mixing energy between fluid molecules and solid walls. The disorderly motion of molecules results in an intensive mixing of the fluid's viscous layers. Consequently, turbulent flows give rise to higher skin friction and heat transfer in comparison to laminar flows. Similarly, due to the heightened momentum exchange between fluid-fluid interfaces relative to laminar flow, the rates of heat and mass transfer at liquid-gas interfaces are greatly enhanced in turbulent flows [87].

From this standpoint, turbulence is not purely a matter of theoretical curiosity. The primary drive for investigating turbulent flows lies in the fact that the vast majority of flows exhibit turbulence, and turbulence significantly accelerates the transport and mixing of various factors, including matter, momentum, and heat. This enhanced transport and mixing holds substantial practical significance. Consequently, fluid engineers require access to reliable tools that can accurately depict the impacts of turbulence. Laminar flows are described by the equations presented in (Section 4.1.1) without any simplifications. In simple cases, it's possible to solve the continuity and Navier–Stokes equations analytically. When dealing with more intricate flows, numerical approaches such as the finite volume method can be applied without the need for extra approximations.

However, turbulence modeling in CFD has been a persistent challenge for decades. Complex flows require varying assumptions, and no single model can predict all turbulent flows accurately. Ideal models balance accuracy and simplicity, though they introduce uncertainties by closing governing equations. These solutions deviate from exact representations, prompting evaluation through experimental data.

Different principal methods for solving turbulent flow numerically which can be categorized into three main groups:

- **Turbulence models for Reynolds-averaged Navier–Stokes equations:** The primary emphasis lies in analyzing the impact of turbulence on the mean flow properties. Before numerically simulating turbulent flow through CFD techniques, the Navier-Stokes equations are subjected to an averaging procedure. This procedure introduces additional terms into the flow equations. Traditional turbulence models are employed to characterize these additional terms. The computational resources required for precise flow computations are not exceptionally demanding, rendering this approach a widely utilized method in engineering flow calculations for the last three decades [88].

- **Large eddy simulation (LES):**

  Large Eddy Simulation addresses the complexities of eddies of varying sizes. Large eddies, due to their nonisotropic nature and intricate behavior, are responsible for the majority of diffusive processes, making their simulation highly desirable. LES aims to resolve and represent the dynamics of the larger eddies while modeling the smaller ones. The method includes a spatial filtering step applied to the unsteady Navier-Stokes equations prior to computation, effectively retaining the larger eddies while filtering out the smaller ones. To account for the influence of the smallest, unresolved eddies, a sub-grid scale model is employed. It's worth noting that unsteady flow equations must be solved, which places significant demands on computing resources in terms of storage and computational volume. This positions LES between (RANS) and (DNS) approaches in terms of computational requirements [89, 90].

- **Direct numerical simulation (DNS)**

  The larger eddies in turbulent flows have a velocity scale (ϑ) and length scale (ℓ) that is comparable to the velocity and length scales of the mean flow. Thus (Re_ℓ) is similar in magnitude to the Reynolds number of the mean flow,(Re_L). As a result, larger eddies are primarily affected by inertia effects. in contrast, The Reynolds number Re_η of the smallest eddies, based on Kolmogorov microscales Eq.4.15a-Eq.4.15c (expressed in terms of the rate of energy dissipation of a turbulent flow and the fluid viscosity), is equal to 1 so that the inertia and viscous effects are of equal strength in smallest eddies.

$$\tau_\eta = \left(\frac{\nu}{\epsilon}\right)^{1/2} \tag{4.15a}$$

$$\eta = \left(\frac{\nu^3}{\epsilon}\right)^{1/4} \tag{4.15b}$$

$$\upsilon_\eta = (\epsilon\,\nu)^{1/4} \tag{4.15c}$$

DNS is the most accurate numerical approach to characterize turbulent flows which computes the mean flow and all turbulent velocity fluctuations without averaging. This implies that all the turbulent scales are resolved by the numerical grid on which the flow is computed and by the temporal integration of the discretized equations [91]. However, to resolve all turbulent structures, it is required that the simulation domain is large enough to contain the large-scale motions of the order of the physical problem domain, while at the same time, the spatial resolution should be small enough to resolve the Kolmogorov scale η. Furthermore, the integration time step t should be small enough to resolve the Kolmogorov timescale τ_η [66], while the total integration should be continued sufficiently long to cover a certain number of integral timescales T.These calculations are highly costly in terms of computing resources, and therefore DNS has been primarily limited to rather low to moderate Reynolds numbers and simplified flow geometries which allow the use of periodic boundary conditions (BC) in one or more principal directions [91].

4.2.1 Reynolds Averaged Navier-Stokes (RANS) Equations

Owing to the stochastic nature of turbulent flows, any properties of the turbulent flow can be described by the average value $\bar{\varphi}$ along with certain statistical properties of their fluctuations φ' superimposed upon it.

$$\varphi(x,t) = \bar{\varphi}(x,t) + \varphi'(x,t) \tag{4.16}$$

In most encountered turbulent flow applications, the focus is on statistical quantities like mean and standard deviation of flow variables, rather than all the flow details. Reynolds decomposition and averaging are crucial concepts in turbulent flow modeling. The averaging operator (indicated by a bar in equation 4.16) must meet specific conditions (detailed in Appendix A.1 and A.2) before application in the averaging process. Three main averaging methods exist. Time averaging is suited for stationary turbulence; spatial averaging is applicable to homogeneous turbulence; and ensemble averaging is the most general approach for time-dependent flows with changing statistical properties.

To account for the fluctuations of the flow properties on the mean flow, the equations in 4.6 and 4.14 are modified by substituting the instantaneous components for the flow variables. In the context of a compressible flow with constant viscosity, applying the time-averaging procedures to the instantaneous continuity equation results in the continuity equation for the mean flow.

$$\nabla \cdot U = 0 \tag{4.17}$$

Applying a similar procedure to the momentum equations results in time-averaged momentum equations:

$$\rho\left[\frac{\partial U}{\partial t} + \nabla \cdot (U\,\mathbf{U})\right] = -\frac{\partial P}{\partial x} + \nabla \cdot (\mu\,\nabla U) + \nabla \cdot \left(-\rho\overline{u'\mathbf{u'}}\right) \tag{4.18a}$$

$$\rho\left[\frac{\partial V}{\partial t} + \nabla \cdot (V\,\mathbf{U})\right] = -\frac{\partial P}{\partial y} + \nabla \cdot (\mu\,\nabla V) + \nabla \cdot \left(-\rho\overline{v'\mathbf{u'}}\right) \tag{4.18b}$$

$$\rho\left[\frac{\partial W}{\partial t} + \nabla \cdot (W\,\mathbf{U})\right] = -\frac{\partial P}{\partial z} + \nabla \cdot (\mu\,\nabla W) + \nabla \cdot \left(-\rho\overline{w'\mathbf{u'}}\right) \tag{4.18c}$$

The equation set in 4.17 and 4.18 a-c is termed the RANS equations. Through the averaging process, new terms have been introduced into the momentum equations, known as the Reynolds stresses [91]. These stresses are the products of fluctuating velocities and signify a convective transfer of momentum caused by turbulent eddies.

This additional momentum transfer is viewed as an extra turbulent stress acting on a surface. In this context, the variance of velocity fluctuations, such as $\overline{u'^2}$,$\overline{v'^2}$ and $\overline{w'^2}$, represents additional normal stresses, while the second moments, which capture correlations between different velocity components (e.g., $\overline{u'v'}$, $\overline{u'w'}$, and $\overline{v'w'}$), correspond to additional shear stresses.

So far, RANS equations were derived assuming a constant fluid density. However, density can exhibit turbulent fluctuations. in such flows and if density fluctuations cannot be ignored, it's advisable to use Favre decomposition for specific quantities in Equations 4.6 and 4.14 instead of Reynolds averaging (see Appendix A.2 for averaging methods). Failing to do so would complicate the averaged governing equations with additional correlations involving density fluctuations. A practical approach is to apply Reynolds averaging for density and pressure while using Favre averaging for other variables [92].

It has been observed that turbulent stresses tend to rise with the increase in the mean rate of deformation. In 1877, Boussinesq suggested that Reynolds stresses might be directly proportional to mean rates of deformation:

$$-\rho\overline{u_i'u_j'} = 2\,\mu_t\overline{S_{ij}} - \frac{2}{3}\rho k\delta_{ij} \tag{4.19}$$

Where $\rho\overline{u_i'u_j'}$ is the Reynolds stress tensor ,μ_t is eddy viscosity. k is the turbulent kinetic energy per unit mass (Eq.4.20), $\overline{S_{ij}}$ is the mean strain-rate tensor (Eq.4.21).

$$k = \frac{1}{2}\left(\overline{u'^2} + \overline{v'^2} + \overline{w'^2}\right) \tag{4.20}$$

$$\overline{S}_{ij} = \frac{1}{2}\left(\frac{\partial U_i}{\partial x_j} + \frac{\partial U_j}{\partial x_i}\right) \tag{4.21}$$

RANS turbulence models are typically categorized based on the number of additional transport equations that must be solved alongside the RANS equations. These additional equations are essential for predicting the extra Reynolds stresses and scalar transport terms needed to close the RANS equation system. Models that employ the

Boussinesq hypothesis fall under the category of eddy viscosity models. On the other hand, models that don't depend on this hypothesis and instead derive precise equations for Reynolds stress are known as Reynolds stress or stress-equation models [66].

Mixing length models provide simplified algebraic equations for μ_t to represent Reynolds stresses. In contrast, Two-Equations models consider the effect of turbulence property transport through convection and diffusion, production, and dissipation rate of turbulent kinetic energy ϵ. All these models assume isotropic μ_t, which can lead to inaccuracies in some flows. Reynolds stress equations (second-order closure) models, on the other hand, solve seven transport equations for each Reynolds stress and the dissipation rate ϵ, this significantly increases the computational resources. It's essential to note that the Reynolds stress equation models are an active area of research and less validated compared to mixing length and two-equation models.

Zero-equation models consistently rely on the Boussinesq assumption to calculate the Reynolds stress tensor. One of the most effective algebraic models, proposed by Prandtl, is based on the mixing-length hypothesis for eddy viscosity calculation. This hypothesis is rooted in dimensional analysis and the idea that the kinematic turbulent viscosity, denoted as ν_t, can be represented as the product of a turbulent velocity scale (ϑ) and a turbulent length scale (ℓ) using the equation:

$$\mu_t = \rho\, C\, \vartheta\, \ell \tag{4.22}$$

where C is a dimensionless constant of proportionality. The hypothesis aims to link the characteristic velocity scale of the largest eddies with mean flow properties. When a single velocity and length scale effectively describe turbulence and the primary mean velocity gradient is $\partial U/\partial y$, Prandtl's mixing length model for thin boundary layers can be interpreted as follows:

For 2-D thin shear layers : $$\mu_t = \rho\, \ell_{mix}^2 \left| \frac{\partial U}{\partial y} \right| \tag{4.23}$$

For 3-D thin shear layers :

$$\mu_t = \rho\,\ell_{mix}^2 \left[\left(\frac{\partial U}{\partial y} \right)^2 + \left(\frac{\partial W}{\partial y} \right)^2 \right]^{0.5} \tag{4.24}$$

where ℓ_{mix} is the Prandtl's empirical mixing length.

Turbulence in different flow scenarios, such as wall boundary layers, jets, and wakes, impacts the evaluation of ℓ_{mix} in the mixing-length model [93]. For simpler turbulent flows, like free turbulent flows and wall boundary layers, ℓ_{mix} can be described using straightforward algebraic equations. However, near solid boundaries, turbulence behaves differently, and the mixing length requires a different approach. Prandtl originally proposed that, near solid boundaries, the mixing length is proportional to the distance from the surface, aligning with the well-known law of the wall (Equation 4.25), observed in a wide range of turbulent flows near solid boundaries.

$$u^+ = \frac{1}{\kappa} \ln y^+ + C \tag{4.25}$$

where C is a dimensionless integration constant and κ is defined as the von Kármán constant. The correlation of measurements indicates $C \approx 5.0$ for smooth surfaces and $\kappa \approx 0.41$ for smooth and rough surfaces [94].

The parameter y_+ is the dimensionless wall distance defined according to equation 4.26. y_+ is a function of the friction velocity u_τ and y, the normal distance from the cell centroid to the wall in wall adjacent cells.

$$y^+ = \frac{u_\tau y}{\nu} \tag{4.26}$$

The dimensionless velocity u^+ is defined as the ratio of the local velocity to the friction velocity u_τ, a velocity scale representative of velocities close to a solid boundary, [94]. According to Eq.(4.27), The friction velocity is a function of the instantaneous surface shear stress and density at the wall.

$$u_\tau = \sqrt{\frac{\tau_w}{\rho}} \tag{4.27}$$

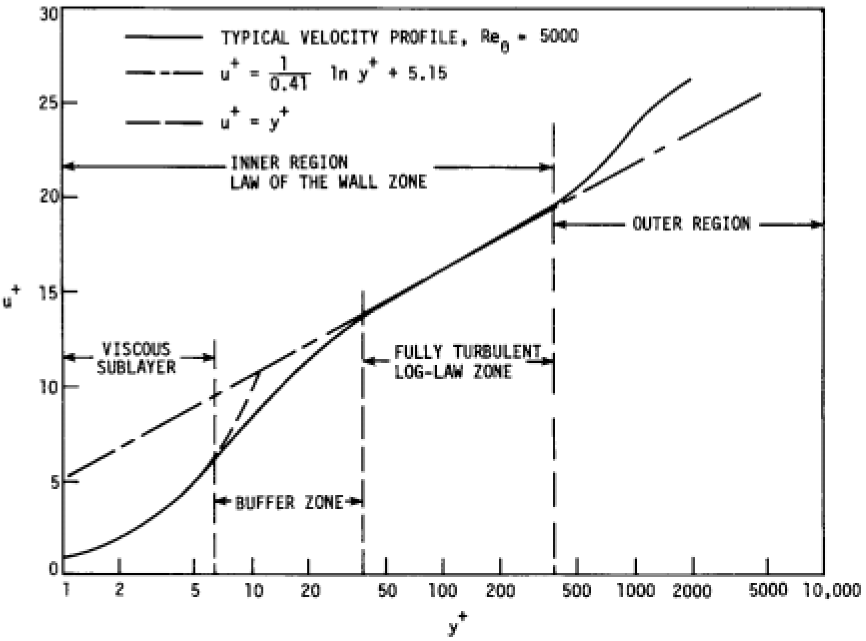

Figure 4.2: Typical velocity profile in the turbulent boundary layer for a typical incompressible flow over a smooth flat plate. [93]

The first key modification was devised by Van Driest who proposed that the mixing length ℓ_{mix} should behave according to equation 4.28 [94], where a damping function is used to bridge the gap between the fully turbulent (log-law zone) region and the viscous sublayer. these two zones are indicated in Figure 4.2, which depicts a typical velocity distribution for an incompressible turbulent boundary.

$$\ell_{mix} = \kappa\, y \left(1 - e^{-y^+/A^+}\right) \tag{4.28}$$

$$\frac{\partial(\rho k)}{\partial t} + \nabla \cdot (\rho k \mathbf{U}) = \nabla \cdot \left(-\overline{p'\mathbf{u'}} + 2\,\mu \overline{\mathbf{u'} s'_{ij}} - \rho \frac{1}{2}\overline{u'_i \cdot u'_i u'_j}\right) - \rho\,\epsilon - \rho\,\overline{u'_i u'_j} \cdot S_{ij} \tag{4.29}$$

The left-hand side in equation 4.29 represents the rate of change and transport by convection of k, and the right-hand side groups the transport of k by pressure, viscous stress, and Reynolds stress,(terms in parentheses), and the rate of dissipation and production of k. where ϵ is the rate of dissipation of turbulent kinetic energy per unit mass defined as:

$$\epsilon = 2\nu \, \overline{s'_{ij} \cdot s'_{ij}} \tag{4.30}$$

Standar $K - \epsilon$ model:

The k-ϵ model is the most widely used and validated turbulence two-equation model. Two transport equations, one for the turbulent kinetic energy k (Eq. 4.32) and a further one for the rate of dissipation of turbulent kinetic energy ϵ (Eq 4.33) are solved. In the k–ϵ model,the kinematic eddy viscosity ν_t is expressed as the product of a velocity scale $\vartheta = \sqrt{k}$ and a length scale $\ell = \frac{k^{3/2}}{\epsilon}$. Dimensional analysis yields :

$$\mu_t = \rho C_\mu \frac{k^2}{\epsilon} \tag{4.31}$$

$$\frac{\partial(\rho k)}{\partial t} + \nabla \cdot (\rho k \mathbf{U}) = \nabla \cdot \left[\left(\mu + \frac{\mu_t}{\sigma_k} \right) \nabla k \right] - \rho \, \epsilon + 2\mu_t \, S_{ij} \cdot S_{ij} \tag{4.32}$$

$$\frac{\partial(\rho \epsilon)}{\partial t} + \nabla \cdot (\rho \epsilon \mathbf{U}) = \nabla \cdot \left[\left(\mu + \frac{\mu_t}{\sigma_\epsilon} \right) \nabla \epsilon \right] + C_{1\epsilon} \, f_1 \frac{\epsilon}{k} 2\mu_t S_{ij} \cdot S_{ij} - C_{2\epsilon} f_2 \rho \frac{\epsilon^2}{k} \tag{4.33}$$

The turbulent transport terms are grouped using gradient diffusion. the transport of k by pressure is accounted for within the gradient diffusion term. Prandtl numbers σ_k and σ_ϵ connect the diffusivities of k and ϵ to the eddy viscosity μ_t. .Production and destruction of turbulent kinetic energy are always closely linked.

The two transport equations for k and ϵ in (Eq.4.32) and (Eq.4.33) are a modified version of the standard $k - \epsilon$ model. These modifications help the model avoid integrating equations all the way to the wall and enable it to handle low Reynolds number flows [95]. This adaptation relies on the universal behavior of near-wall flows, as defined in Equation 4.25, which involves adding a damping function to maintain accuracy in the viscous sublayer near solid walls. This ensures that viscous stresses become more dominant than turbulent Reynolds stresses.

The equations contain five adjustable constants issued by comprehensive data fitting for a wide range of turbulent flows: C_μ, σ_k, σ_ϵ, $C_{1\epsilon}$ and $C_{2\epsilon}$. The most obvious modification for low Reynolds formulation, which is universally made, is to include the molecular viscosity μ in the diffusion terms in equation 4.32 and 4.33 and the constants C_μ,$C_{1\epsilon}$ and $C_{2\epsilon}$ are multiplied by wall-damping functions f_1 and f_2 respectively, which are themselves functions of the turbulence Reynolds number.

The k–ϵ model provides accurate results for a broad range of flows where Reynolds shear stresses are most important, including recirculating and confined ones. Nevertheless, research has pointed out several limitations. In low Reynolds number flows, the k and ϵ equations need to be integrated into the wall because the use of a log-law-based wall function is not precise. This necessitates a finer grid resolution to accurately represent the distribution and dissipation of turbulent kinetic energy in the buffer layer, along with a non-linear wall-damping function to transition from fully turbulent to a viscous-sublayer zone. Consequently, this can affect solution convergence. The standard k–ϵ model struggles in complex flows where the gradient of normal turbulent stresses is significant, which is a consequence of Boussinesq's hypothesis related to its prediction of isotropic normal Reynolds stresses. This inaccuracy becomes more apparent in cases with strong adverse pressure gradients and recirculation regions, stemming from the isotropy of predicted normal Reynolds stresses. Additionally, effects, like streamline curvature, rotation, and external forces, introduce further interactions between mean strain rates and Reynolds stresses, which standard two-equation models fail to capture [88].

- Two-layer $k - \epsilon$ model:

  the two-layer model represents an advanced treatment of the near-wall region at a low Reynolds number. the improvement consists of sub-dividing the boundary layer into two regions. to avoid the numerical instability associated with the use of non-linear wall-damping functions to integrate both k and ϵ equations to the wall, the model uses the standard $k - \epsilon$ model only for the fully-turbulent region, for the viscous region however, only the k-equation is solved in this region and a length scale is prescribed for the evaluation of the rate of dissipation with and the eddy viscosity. The two-layer model is less grid dependent and more numerically stable than the earlier low Reynolds number k–ϵ models and has become quite popular in more complex flow simulations where integration to the wall of the flow equations is necessary.

- Realizable $k - \epsilon$ model:

  One notable advancement over the standard k- model is the realizable $k - \epsilon$ model. It was developed to address the limitations of existing models in accurately representing near-wall eddy viscosity behavior. Unlike the standard model, the realizable model incorporates a variable model coefficient based on mean flow and turbulence properties, ensuring it complies with mathematical constraints related to normal stresses and turbulence physics. The concept of a variable model coefficient is also consistent with experimental data in boundary layer flow. As a result, the realizable $k - \epsilon$ model is generally more accurate and reliable than the standard model in various applications [66].

- RNG $k - \epsilon$ model:

  The main difference between the standard $k - \epsilon$ model and the RNG $k - \epsilon$ model is their dissipation equation formulation. In the RNG $k - \epsilon$ model, an extra term is included to counteract the excessive dissipation seen in the standard model, which tends to dampen effective viscosity, particularly in recirculating flows. The RNG model is more responsive to rapid strain and curved geometries, making it better suited for swirling flows. However, it falls short in predicting jets and plumes compared to the standard k- model. The RNG model's constants differ slightly from the empirically determined constants in the standard $k - \epsilon$ model, as it's derived using a mathematical renormalization group technique from the Navier-Stokes equation [96].

Wilcox* $k - \omega$ *model:

The k–ω model attracted attention and has proven to be superior in numerical stability to the $k - \epsilon$ model primarily in the viscous sublayer near the wall because integration to the wall does not require wall-damping functions in low Reynolds number applications. the $k-\omega$ model proposed by Wilcox [97] uses the turbulence frequency $\omega = \epsilon/k$ (dimensions s^{-1}) as the second determining variable to express the dynamic eddy viscosity ν_t instead of The rate of dissipation of turbulence kinetic energy ϵ.If we use this variable, the eddy viscosity is given by :

$$\nu_t = \frac{\rho\, k}{\omega} \tag{4.34}$$

The Reynolds stresses are computed with the Boussinesq expression The transport equation for k and ω for turbulent flows at high Reynolds is as follows:

$$\frac{\partial\left(\rho k\right)}{\partial t} + \nabla\cdot\left(\rho k \mathbf{U}\right) = \nabla\cdot\left[\left(\mu + \frac{\mu_t}{\sigma_k}\right)\nabla k\right] + P_k - \beta^{*}\rho k\omega \tag{4.35}$$

$$\begin{aligned}\frac{\partial\left(\rho\omega\right)}{\partial t} + \nabla\cdot\left(\rho\omega\mathbf{U}\right) = \nabla\cdot\left[\left(\mu + \frac{\mu_t}{\sigma_\omega}\right)\nabla\omega\right] - \beta_1\rho\omega^2 \\ + \gamma_1\left(2\rho S_{ij}\cdot S_{ij} - \frac{2}{3}\rho\omega\frac{\partial U_i}{\partial x_j}\delta_{ij}\right)\end{aligned} \tag{4.36}$$

where P_k is the rate of production of turbulent kinetic energy with the model constants are : $\sigma_k = 2.0$, $\sigma_\omega = 2.0$, $\gamma_1 = 0.553$; $\beta_1 = 0.075$, $\beta^{*} = 0.09$.

Menter SST $k-\omega$ ***model:***

Shear Stress Transport (SST) $k-\omega$ turbulence model combines different elements of existing models and was developed to overcome the strong sensitivity to the assumed values of ω in the free stream of the original $k-\omega$ model of Wilcox. Menter [98] noted that the results of the k–ϵ model are much less sensitive to the assumed values in the free stream, but its near-wall performance is unsatisfactory for boundary layers with adverse pressure gradients. this led him to suggest a hybrid model using a transformation of the k–ϵ model into a k–ω model in the near-wall region and the standard k–ϵ model in the fully turbulent region far from the wall [88]. The (SST) $k-\omega$ model gives similar results to those of the original $k-\omega$ and is identical to the Wilcox model in the inner 50*percent* of the boundary layer but changes gradually to the high Reynolds number $k-\epsilon$ model towards the boundary-layer edge. It is based on the BSL model but has the additional ability to account for the transport of the principal shear stress, this ability shows to give excellent agreement with experimental data in adverse pressure gradient boundary layers [99, 100]. The Reynolds stress computation and the k-equation are the same as in Wilcox's original k–ω model, but the ϵ-equation is transformed into an ω-equation by substituting $\epsilon = k\omega$.

4.3 Simulation setup

In turbomachinery simulations, the rotating impeller introduces mesh motion, resulting in inherently unsteady conditions. To address this, the unsteady Navier-Stokes equations are solved at each time step, demanding substantial computational resources. An alternative approach involves transforming these motion equations from an unsteady to a steady state with respect to a moving reference frame. This transformation is achieved by incorporating Coriolis and centripetal acceleration terms into the momentum equations. By making this transformation, a common strategy known as the Single reference frame (SRF) can be applied. In the SRF approach, the entire computational domain is solved within a single moving reference frame, typically modeling a single blade passage with periodic boundary conditions, significantly reducing the computational effort. However, when dealing with centrifugal fans, the geometry doesn't align with the SRF approach requirements [101]. Consequently, the entire fan rotor must be considered, and the computational domain is divided into multiple zones separated by interfaces to account for the coupling between the rotating and stationary parts. This approach is known as the Multiple reference frame (MRF) or Frozen Rotor approach and is widely used in industrial fan simulations due to its time and resource efficiency.

It's important to note that adding Coriolis and centripetal terms to the momentum equations in the rotating frame constitutes an approximation of the flow field physics, which may impact the accuracy of numerical results. To accurately model flow instability and related phenomena, a three-dimensional numerical simulation of the unsteady flow field throughout the entire centrifugal fan domain is necessary. This is achieved using a sliding mesh technique where the impeller domain physically moves relative to the stationary parts. As a result, this approach demands increased computational effort compared to the MRF method [59].

Based on the above discussion, the modeling approach in this study consists of two steps. First, a steady-state simulation based on RANS simulation is conducted using the MRF approach. Then, the converged solution obtained from this step is utilized as the initial solution for the unsteady simulation, which employs the sliding mesh technique.

4.3.1 Spatial Discretization

Discretization involves approximating differential equations using a set of algebraic equations for variables at specific discrete points in space and time. For spatial discretization, there are three primary methods: Finite difference methods (FDM), Finite element methods (FEM), and Finite volume methods (FVM). In general, FEMs and FDMs serve as fundamental tools for solving partial differential equations. In contrast, Finite Volume Methods (FVM) have gained popularity in recent years in computational fluid dynamics (CFD) due to their straightforward data structure, and their formulations draw from both FDM and FEM approaches [102].

Spatial discretization of the governing equations can be accomplished using either structured or unstructured grids. In structured grids, each grid point is identified by indices (i, j, and k) and their respective Cartesian coordinates. These grid systems feature regularly aligned grid that lines in two or three directions, providing efficient access to neighboring grid points in computer memory. This simplifies tasks like gradient calculations, flux evaluations, and handling boundary conditions, making structured grids advantageous [92]. However, structured grids have limitations when dealing with intricate geometries. In such scenarios, a multiblock approach, as discussed in [103] and [104], can be employed. This approach involves dividing the grid into multiple blocks, which increases the complexity of the flow solver, as it necessitates the exchange of physical quantities or fluxes between these blocks.

In many modern industrial CFD applications, the computational domain's geometry tends to be highly complex. Consequently, unstructured grids are extensively utilized to fit these complex shapes. In an unstructured mesh, grid cells and grid points lack specific ordering or identification based on indices [92]. This results in a non-regular structure for the matrix in the algebraic equation system, requiring sophisticated data structures for the solver. This, in turn, can demand higher computational resources compared to structured schemes. with the various cell shapes available in most of the meshing software (e.g., triangles, tetrahedrons, prisms, pyramids, and polyhedrons), Unstructured meshes offer a high degree of flexibility in handling complex geometries. Nevertheless, when dealing with mixed grids near solid walls for boundary layer resolution, challenges arise, and generating mixed grids can be a challenging task. However, it's worth noting that the time required to construct an unstructured, mixed grid for a complex configuration is still significantly less than what's needed for a multiblock structured grid.

The computational domain of the fan was spatially discretized using ANSYS ICEM-CFD, employing unstructured tetrahedral grids for the fan's core region. The suitability of the cell shape used in this study has been validated for three-dimensional fan simulations, as confirmed by previous works such as [105–109], and for simulations of rotating machines, as demonstrated by [110, 111].

In order to address the interaction between the intake, rotating impeller, and stationary casing domain, the computational domain was divided into multiple zones using sliding interfaces. These interfaces enable the passage of flux through non-conformal mesh connections during unsteady simulations. As illustrated in Figure 4.3, one of the interfaces spans across the region between the inlet cone and the impeller entry, while the second interface encompasses the area between the impeller and the casing discharge area. Additionally, consideration was given to the gap between the intake cone and the impeller inlet section to permit the passage of flux through this gap.

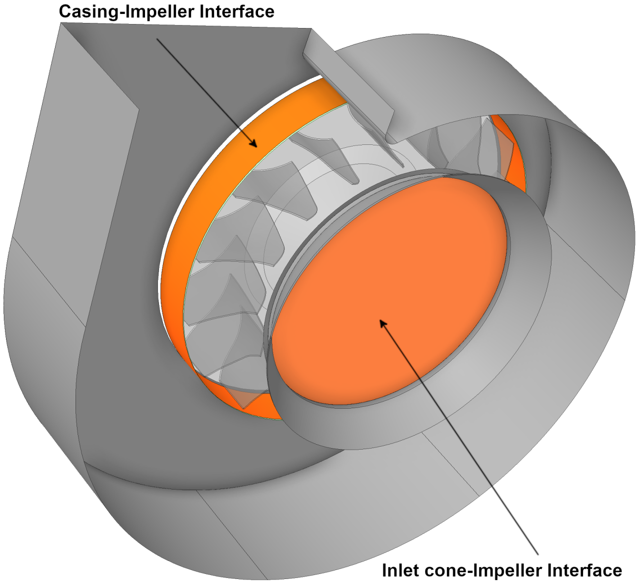

Figure 4.3: Placement of sliding interfaces (orange surfaces) relative to the fan parts

A crucial aspect of mesh generation involves the careful selection of the appropriate size for the mesh elements. The primary requirements are to ensure there are no gaps between grid cells and that they do not overlap [112]. Additionally, the grid must exhibit smoothness, with refinement strategically placed in regions featuring high variable gradients or other significant fluid flow phenomena of interest [92]. With these considerations in mind, this study followed an iterative procedure, involving successful mesh refinement and RANS simulations, to determine an optimal grid configuration for achieving grid-independent results. This grid configuration aimed to faithfully capture all the essential physical details and core aspects of the flow. The ongoing challenge remained achieving higher solution accuracy while minimizing simulation time.

To assess the suitability of the grid configuration for conducting transient simulations, the power shaft (W_{shaft}) and total pressure rise were monitored during steady-state simulations at the design flow rate and a fixed blade pitch position. The mesh refinement process primarily focused on the blade tips, blade passage, and casing throat area, ensuring a seamless transition from low to high grid density. This smooth transition between fan regions is critical as it is essential for accurately simulating the unsteady flow exiting the rotating impeller to the casing discharge. Table 4.1 provides data on the power shaft and total pressure variations at the impeller inlet with different grid densities.

Number of nodes (million)	W_{shaft} (kW)	ΔP_t (Pa)
4.3	495.3	6253.23
5.1	492.1	6156.18
5.57	488.4	6141.55
5.58	488.1	6130.22
5.98	487.9	6110.25

Table 4.1: Grid density sensitivity of (W_{shaft}) and (ΔP_t) .

Grid refinement was deemed unnecessary when the grid size exceeded 5.57 million for the sake of computational efficiency. A total of 5,574,675 unstructured tetrahedral cells were used for a mesh-independent solution. A sectional view at the blade mid-span of the mesh is depicted in Fig. 4.4.

An issue that commonly arises when using unstructured meshes is how to handle near-wall boundaries, particularly when precise predictions of near-wall flow are needed due to the steep gradient in flow variables. To address this challenge in unstructured grids, a solution involves creating multiple thin inflation layers, often referred to as prism layers, perpendicular to the boundary surfaces. The mesh resolution of the core flow is then constructed based on the last prism layer, as illustrated in Figure 4.5, which displays the generation of prism layers orthogonal to the blade surface.

Various turbulence models have specific requirements for near-wall mesh resolutions, and some are applicable only within a certain range of y^+ values.The value of y^+ is

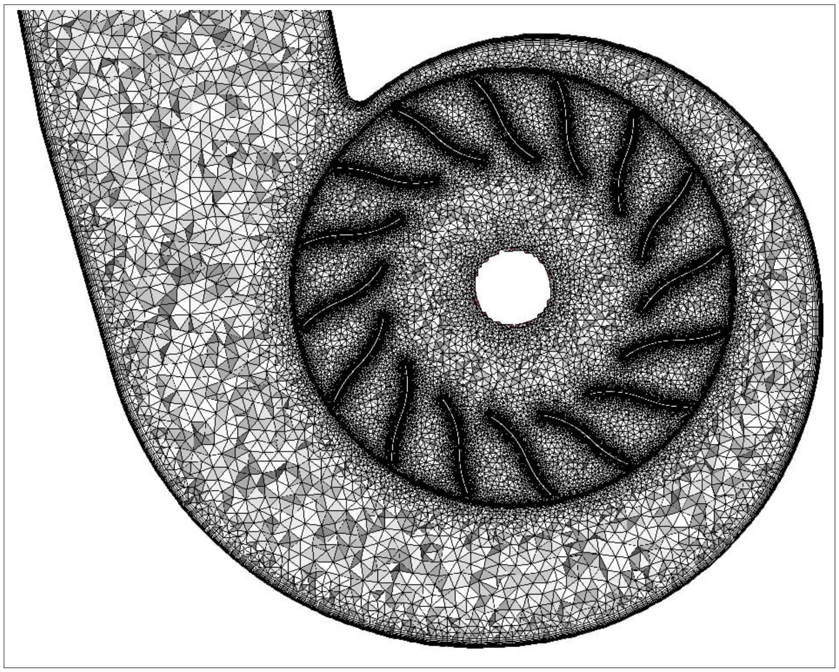

Figure 4.4: Cut plane of the mesh normal to the axis of rotation.

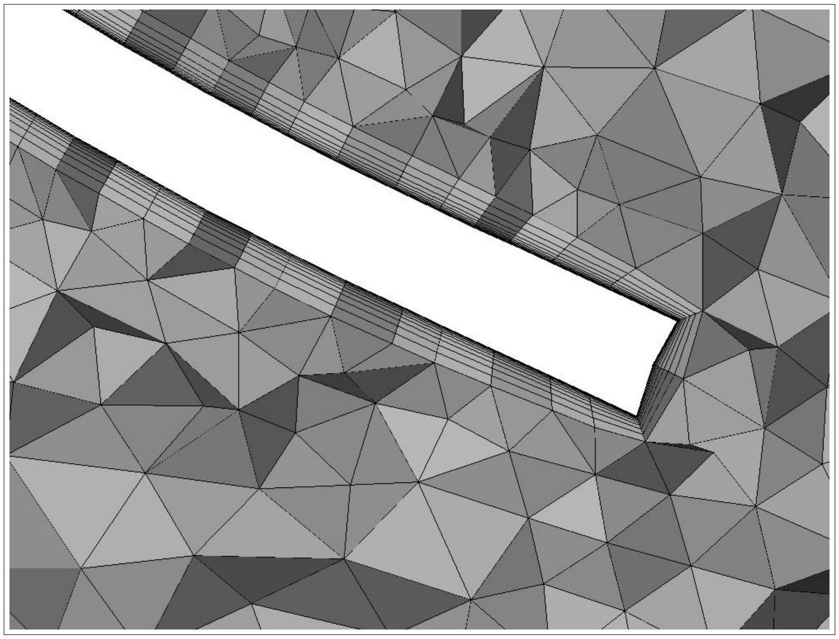

Figure 4.5: Near wall mesh resolutions on the blade surface.

an important factor for ensuring a good mesh resolution, especially in turbulent flow simulations. However, it's not the only factor to consider. Both the geometric growth ratio and the number of normal cells also play crucial roles in achieving an accurate and reliable simulation. For turbulent flows, maintaining a low value of y^+ (around 1) is recommended to meet the requirements of the SST k-ω model and accurately model the viscous sublayer and the turbulent boundary layer. The process of selecting these grid parameters involves a balance between accuracy and computational cost. Here's the approach adopted in the study:

The first step is to estimate the height of the first layer of prism cells normal to the surface wall boundaries (Y_h) to ensure that the non-dimensional parameter y$^+$ was less than or equal to one for both stationary and rotating domains. Y_h is a function of y^+ and the frictional velocity u_τ according to Eq 4.26. The first estimate value of (Y_h) was calculated from Eq. 4.26 by specifying the target value of y^+.

the frictional velocity u_τ was calculated using Eq. 4.27, where the wall shear stress, τ_w can be calculated from skin friction coefficient, C_f, such that:

$$\tau_w = \frac{1}{2} \cdot C_f \cdot \rho \cdot U^2 \tag{4.37}$$

where U is the free stream velocity. The value of C_f was estimated using the Empirical formula in Eq. 4.38 and the Reynolds number is based on the characteristic scales of our geometry Eq.4.39

$$C_f = 0.027\, Re_L^{-1/7} \tag{4.38}$$

$$Re = \frac{UL}{\nu} \tag{4.39}$$

where U is the free stream velocity, L is the characteristic length scale, and ν is the fluid kinematic viscosity.

The value of σ_{99} corresponding to Re and L was calculated from the following equation [68]:

$$\sigma_{99} = \frac{0.38L}{Re_L^{1/5}} \tag{4.40}$$

the value of the boundary layer thickness was set to be equivalent to the total prism layer height Y_T and the maximum geometric growth ratio (G) which determines the increase in cell size as you move away from the wall was computed employing the relation provided in Equation 4.41. therefore, Choosing an appropriate growth ratio ($1.1 \sim 1.3$) is important to ensure that the grid captures the gradual transition from the near-wall region to the outer flow. If the growth ratio is too high, potentially missing important flow features. If it's too low, the grid might become overly refined near the wall, leading to unnecessary computational costs.

$$Y_h \frac{1 - G^N}{1 - G} \tag{4.41}$$

The total number of normal cells affects how well the boundary layer is resolved and how accurately turbulent flow features are captured. Having an appropriate number of normal cells is important to ensure that the flow's behavior is accurately captured from the wall to the free stream. Too few normal cells might not sufficiently resolve the flow physics near the wall, and too many cells could result in excessive computational requirements without a significant improvement in accuracy. the growth ratio was solved by setting the minimum recommended value of N for a resolved boundary layer (e.g. $Y^+ \sim 1$) to 15.

However, it's important to note that the formula 4.40 is typically used for estimating the momentum thickness in flat plate boundary layers. however, in the context of a centrifugal fan simulation, the flow is significantly different due to the fan's geometry and the rotational effects. thus, The flow near the fan blades is likely to be more complex and affected by centrifugal forces, which can result in different flow characteristics compared to a flat plate scenario. Thus an iterative process was used to achieve the desired Y^+ value and select the appropriate grid parameters. The iterative process involved the estimation of Y_h. the second step is to compute the growth ratio required. step (3) involves the solution and postprocessing of y$^+$ from the obtained solution. this process is repeated until a satisfactory result is achieved. the main problem when creating a prism layer is that the aspect ratio of the prism cells increases if one uses coarse mesh and the volume transition between the final inflation layer and the freestream cells should not be steep. thus, The mesh was refined and smoothed until quality metrics such as skewness, aspect ratio, and orthogonal quality were satisfactory (See Table 4.2, ensuring numerical stability and convergence.

The resulting range of the y$^+$ distribution on critical regions such as the impeller and the casing is presented in Figure 4.6. The mesh resolution as well as the first prism height was adjusted for each operating condition simulation to ensure that y$^+$ is within the recommended limit, which is acceptable for accurately solving the flow.

Zones	Total nodes		Skew	Aspect ratio	Orthogonal quality
Impeller	4806381	Min	0.33	2	0.13
		Max	1	21.99	1
		Average	0.94	4.37	0.77
Casing	748484	Min	0.4	2	0.31
		Max	1	10.28	1
		Average	0.94	4.31	0.778
Intake cone	19810	Min	0.71	2	0.201
		Max	0.99	17.016	0.99
		Average	0.93	4.39	0.769

Table 4.2: summary of the quality statistics unstructured grids generated for simulations

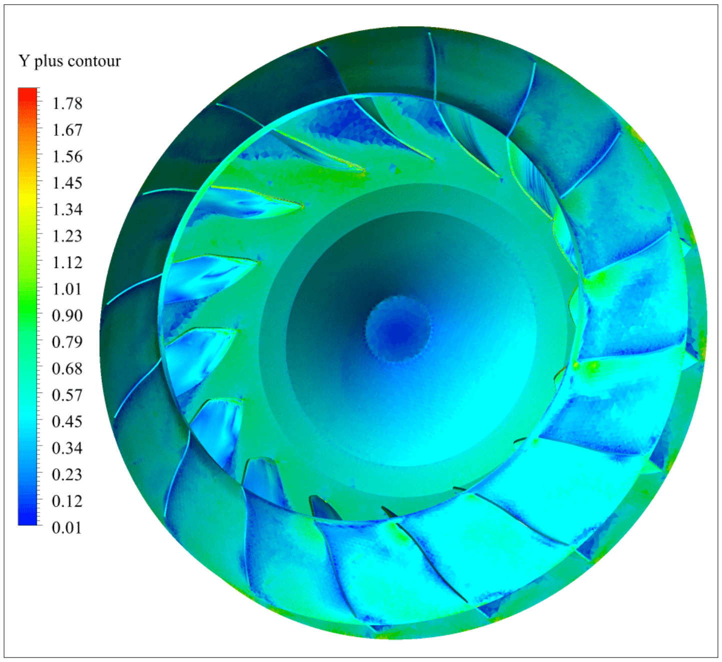

Figure 4.6: Y^{+} distribution on the impeller.

4.3.2 Boundary condition and time-step

To model the Boundary conditions, a constant volume flow rate was specified by imposing a velocity profile at the fan intake and constant static pressure at the fan outlet. The simulation involved examining different flow rates, specifically: $0.74\mathrm{Q_d}$ ($40\,\mathrm{m^3/s}$), $0.89\mathrm{Q_d}$ ($48\,\mathrm{m^3/s}$), the design flow rate ($\mathrm{Q_d}$-$53.9\,\mathrm{m^3/s}$), ($1.33\mathrm{Q_d}$) ($72\,\mathrm{m^3/s}$) and $1.78\mathrm{Q_d}$ ($96\,\mathrm{m^3/s}$). for each flow rate, A uniform velocity profile was imposed at the inlet section of the fan, and atmospheric pressure was applied at the outlet section of the fan. To specify turbulence parameters, uniform and medium turbulent level values of turbulence quantities were specified at the boundaries, with two turbulent quantities defined, namely a turbulent intensity of 5% and a viscosity ratio of ten. No-slip boundary condition was set for all of the wall surfaces. the impeller was set to rotate at 985 rev/min.

In the context of transient simulations, the evolution of the solution and the rate at which transient data is recorded from the initial time to the specified final simulation time is controlled by the time-step Δt. The complexity of the flow and the underlying physics are key factors in determining the appropriate size of the time step. Generally, for complex flows such as turbomachine simulations, it's recommended to use a smaller time-step size along with an adequate number of inner iterations to capture all essential flow characteristics, ensure numerical stability, and provide enough time to resolve the unsteady interactions between the rotating blades and the casing walls.

Opting for smaller time steps might lead to delayed solution convergence, subsequently extending the total simulation duration. An effective time-saving strategy is to initiate unsteady simulations with larger time steps and progressively decrease them as the solution advances. This approach can be complemented by modifying the impeller's rotational speed. Initially, the simulation begins with a lower rotational speed (in rpm), which is gradually increased to the actual speed as the solution progresses. Simulation outcomes reveal that these techniques significantly cut down computational time, enhance convergence, and uphold the final result's accuracy.

in this study, Time marching is controlled by an implicit second-order backward Euler scheme. the time-step is proportional to the impeller period and was chosen in a way that a blade passage is resolved at least by 20 time-step. the smallest time step used in this study is equal to $\Delta \mathrm{t} = \mathrm{T}/1440 = 4.23012\ 10^{-5}$ s, where T is the impeller period (s). this time step size corresponds to an impeller rotation of 0.25°. The number of iterations at every time step is adjusted to reduce the residuals to the value of 10^{-6} for the continuity equation and 10^{-5} for the momentum and turbulence quantities. time-step is changed from the coarse to the fine at the end of the first impeller revolution according to Table 4.3. To achieve the specified residual level, the maximum inner iterations per time-step are adjusted for every time-step size.

Time-steps (s)	Time-steps per blade passage	Impeller rotation (degree)	Max inner-iterations
$1.69204\ 10^{-4}$	22.5	1	12
$8.46024\ 10^{-5}$	45	0.5	8
$4.23012\ 10^{-5}$	90	0.25	6

Table 4.3: Summary of time steps employed in this study

4.4 Particle-laden flow modeling

Particle-laden flows are complex two-phase systems in which a fluid, whether it's a liquid or gas, carries solid particles. Such flows find extensive use across various industrial processes. Therefore, optimizing the design and management of particle-laden flow systems requires special attention and a deep understanding of modeling these complex flow systems. Due to the available high-performance computer hardware and numerical algorithms, CFD has become a powerful tool to model such complex flows and can provide both qualitative and quantitative results. In order to make precise predictions about the behavior of the solid particles in the system, it is essential to select a numerical method that can effectively incorporate the complex physics associated with particle-fluid interactions, interactions between particles and walls, for various particle size distribution [113].

Various multiphase models have been subject to numerical investigations, with each model having its own set of advantages and disadvantages. It's important to note that there is no general model that can effectively simulate all types of multiphase flows commonly encountered in practical systems. The choice of which model to use depends on many factors, such as the desired accuracy of results, computational time constraints, and suitability for large-scale systems [114].

Multiphase flows can be approached through two common methods: the Eulerian-

Eulerian (EE) approach and the Eulerian-Lagrangian (EL) approach [113]. In the E-E approach, also known as the two-fluid model (TFM), both phases occupy the same computational cells and are treated as continuous. This involves representing the dispersed phase using separate sets of conservation equations, which include interaction terms that describe the coupling between the two phases [115, 116]. The model is derived through volume or ensemble averaging of the governing equations, and the constitutive relations for the solid phase are typically closed using the kinetic theory of granular flow (KTGF) [117]. The averaging process introduces a volume fraction function, defined as the probability of finding a particular phase in a fixed control volume in both space and time [8]. One advantage of the E-E approach is that it generally demands fewer computational resources compared to the Eulerian-Lagrangian approach because the dispersed phase is considered as another continuum alongside the continuous phase. It is also computationally efficient for two-way coupling simulations. However, one limitation is that, due to the continuum description of the dispersed phase, the discrete nature of solid particles is not fully captured in the E-E method. This approach also requires separate treatment for particles of varying shapes and sizes, resulting in increased computational expenses in terms of both storage and processing time [118].

In the Eulerian-Lagrangian (E-L) approach, the fluid phase is represented as a continuum by solving the Navier-Stokes equations, while the solid phase is described in a Lagrangian framework, treating each individual particle as a single point. The modeling procedure typically involves computing the fluid flow field initially, followed by solving equations of motion for each particle, allowing for solving individual particle trajectories. The Lagrangian technique offers a more straightforward method to describe phenomena such as particle turbulent diffusion and particle interactions with solid boundaries [115]. Although (E-L) approach can provide highly accurate solutions, they frequently necessitate the tracking of a significant number of individual or stochastic particles as they traverse the computational domain to ensure that the numerical outcomes remain independent of the total particle number. In E-L simulations, it's common to consider a large computational particle equivalent to the number of physical particles or a reduced number to minimize computational costs [119]. However, it's essential to acknowledge that tracking the exact number of particles in the real system is impossible, and thus some level of error may be acceptable, especially when dealing with a relatively low volume fraction of the solid phase [8, 120].

4.4.1 Particle equation of motion

Dispersed two-phase flows can be broadly categorized into two flow regimes: the dilute regime and the dense regime. In the dilute regime, the spacing between solid particles is relatively large, making interactions between them infrequent. Consequently, their movement is primarily influenced by forces from the continuous phase, such as drag and lift. On the other hand, in dense dispersed systems, the spacing between particles is smaller, and inter-particle interactions become significant [96].

Identifying the coupling regime between the fluid and solid phases is crucial for selecting an appropriate modeling approach for particle-laden flows. In dispersed flows, where individual particles are mainly influenced by fluid forces rather than interactions with each other, three coupling regimes are evident: one-way, two-way, and four-way. In a one-way coupling regime, solid particles don't significantly impact the continuous phase, and only fluid-induced forces on particles are considered. Conversely, the two-way coupling regime incorporates a source term in fluid momentum equations to account for the particles' presence, addressing their influence on flow dynamics. In the four-way coupling regime, particle-particle interactions affect the dynamics of both phases.

One important parameter that is used to characterize dispersed two-phase flows is the volume fraction of the dispersed phase expressed in (Eq. 4.42) [96].

$$\alpha_p = \frac{\sum_{i=1}^{N} V_p^i}{V_T} \tag{4.42}$$

where V_T is the total volume, which includes both phases, and V_p^i is the volume of a single particle. N is the total number of injected particles. the volume fraction of the continuous phase α_f can be defined in a simple relation:

$$\alpha_p + \alpha_f = 1 \tag{4.43}$$

If the volume fraction of the solid phase, denoted as α_p, is not significantly high, typically below 10^{-3}, particle-particle collision can be disregarded, and the two-phase system can be treated as dilute [121]. Within this range, when $\alpha_p \leq 10^{-6}$, the impact of particles on the fluid flow is negligible, allowing for the use of a one-way coupling modeling approach. However, when the volume fraction becomes substantial enough to affect the mixture's average density, the particle on the fluid flow cannot be ignored, and two-way coupling models should be employed. For volume fractions of the dispersed phase exceeding 10^{-3}, inter-particle interactions become significant, categorizing the two-phase system as dense, thus necessitating the adoption of a four-way coupling model [58].

This study will investigate various particle concentrations across three distinct operating conditions. However, for the specific applications under examination, the maximum order of magnitude of α_p typically falls below the threshold of 10^{-6}. Consequently, the research employs the Eulerian-Lagrangian method to model the behavior of the two phases within the centrifugal fan domain, assuming a one-way coupling regime. This assumption is reasonable for multiphase flows with a low volume fraction and introduces only a small margin of error.

In the Eulerian-Lagrangian method, the fluid phase is solved first in the Eulerian reference frame, and then the individual trajectories of solid particles are tracked as they are driven by the flow of the continuous phase in a Lagrangian reference frame. the particle trajectory is computed by solving a set of ordinary differential equations that determine the position and velocity of each particle over time. if particles are surrounded by a moving fluid, then all forces acting on a particle are due to the relative motion of the surrounding fluid and particle, body forces, and forces that act on any object immersed in fluid irrespective of either particle or fluid motion.

The motion of the particle will depend on the balance of the forces acting on it. and if all these forces can be quantified, The equation of motion of the particles can be deduced from Newton's second law. The particle momentum equation that determines the behavior of individual particles as they are driven by the fluid flow was derived by Basset, Boussinesq, and Oseen which can be expressed as [122]:

$$\frac{d\mathbf{V}_p}{dt} = \mathbf{F}_D + \mathbf{F}_B + \mathbf{F}_R + \mathbf{F}_{VM} + \mathbf{F}_P \tag{4.44}$$

The path line of the particle through the discretized domain can be tracked by integrating the particle velocity over time:

$$\frac{dx_p}{dt} = V_P \tag{4.45}$$

Where $\mathbf{V}_{\mathrm{p}}$ is the particle velocity vector, x_P is the particle spatial position.

Equation (4.44) equates the total forces exerted by the fluid on the particle and its inertia. The right-hand side of the equation groups the total forces including the drag force per unit mass F_{D}, the buoyancy force per unit mass F_{B}, F_{R} is the forces that arise due to domain rotation e.g. (centrifugal and Coriolis forces added in the rotating reference frame of the impeller domain), an additional forces that are compounded by the virtual mass force F_{VM} which arises from the fact that the particle has to accelerate the surrounding fluid, and the pressure gradient force per unit mass F_{P} which results from a significant fluid pressure gradient around the particle.

Drag force, F_D:

In most particulate flows, the drag force per unit particle mass F_{D} acting on a spherical particle is the dominant force [56]. the drag force is defined as:

$$F_D = \frac{18\,\mu}{\rho\, d_p^2} \frac{C_D\, Re_p}{24}\,(V_f - V_p) \tag{4.46}$$

Where V_f is the fluid velocity, μ is the fluid dynamic viscosity, V_p is the particle velocity, ρ is the particle density, d_p is the particle diameter, C_D is the dimensionless drag coefficient and Re_p is the relative particle Reynolds number defined as:

$$Re_p = \frac{\rho}{\mu_f} d_p\, |V_f - V_p| \tag{4.47}$$

an important nondimensional parameter to characterize fluid-particle flows is the Stokes number, it can describe the intensity of the particle-fluid interaction. It is defined as the ratio of the particle fluid response time to an appropriate turbulence time scale :

$$Stk = \frac{\tau_p}{\tau_t} \tag{4.48}$$

where τ_p is the particle response time, defined as the time required for a particle to respond to changes in the flow velocity. and τ_t is the characteristic time scale of the flow field's (characteristic eddy lifetime). If the Stokes number is significantly smaller than unity, particles will have enough time to adjust to variations in flow velocity, resulting in particle and fluid velocities being almost equal. thus, particles with small Stk when introduced in a turbulent flow will remain under the influence of a particular eddy during the lifetime of that eddy before it goes under the influence of another eddy [122]. Conversely, if the Stokes number is much larger than one, particles won't have sufficient time to react to changes in fluid velocity, causing little impact on the particle velocity. An estimated correlation between the ratio of particle to fluid velocity, based on the Stokes number, can be derived from the "constant lag" solution [123]:

$$\frac{V_p}{V_f} = \frac{1}{1 + Stk} \tag{4.49}$$

the inertial effect of particles, defined as the strength of the velocity fluctuations of the particle (rms) compared to the fluctuations of the surrounding fluid, is characterized by the particle response time which can be mathematically expressed as:

$$\tau_p = \frac{24\,\rho_p\,d_p^2}{18\mu_f\,C_D\,Re_p} \tag{4.50}$$

The drag coefficient in Equation (4.46) is a function of the particle Reynolds number. In the case of creeping flow $Re << 1$, where the nonlinear advection term in the momentum conservation equation may be neglected in comparison to the viscous term, Stokes 'law provides an analytical definition of the drag coefficient for flows of low particle Reynolds number (Stokes regime) when $Re_p < 0.1$: $CD = 24/Re_p$. At finite Reynolds numbers, Experimental observations have shown that a wake is formed behind the sphere even at low Reynolds numbers and the inertia of the flow around the sphere overcomes the viscosity effects on the surface of the sphere. thus the nonlinear advection term must be retained in the solution of the equations.

determination of the hydrodynamic force on a sphere at finite Reynolds numbers was first solved by Oseen (1913) [124] using a simple perturbation method to calculate a first-order correction for the steady-state drag coefficient [123]:

$$C_D = \frac{24}{Re_p}\left(1 + \frac{3}{16}Re_p\right) \tag{4.51}$$

the same method was employed along with the expansion of the stream function and the approximation of the velocity field around the sphere to calculate the second-order correction for the steady-state drag coefficient [125]. these expressions may be used with accuracy for small relative Reynolds numbers up to 0.7. In the transitional zone $(0.1 < Re_p < 10^3)$ where both viscous and inertial effects are important, it is advisable to use empirical or semiempirical expressions for the steady-state drag coefficient. thus, experimental investigations are needed to derive the relationship between the drag coefficient and the related Reynolds number. the average value of different data which are extensively referenced in the literature was tabulated as Standard Drag Curve data by Lapple-Shepherd [126], the plot of these data is shown in (Fig. 4.7) and considered by Schlichting as the Standard Drag Curve (SDC) for spheres [127].

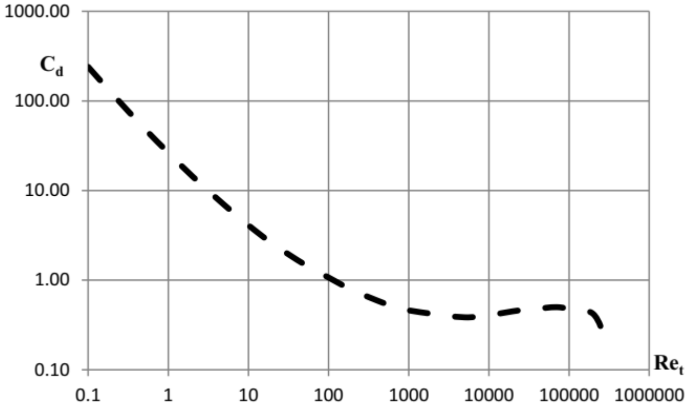

Figure 4.7: Standard drag curve for rigid spherical particles [127]

In the present study, the empirical correlation of Schiller and Naumann [128] is applied to determine the particle drag coefficient. this correlation is recommended to be used in the range $2 < \mathrm{Re}_p < 800$ and is expressed in the following form:

$$C_D = \frac{24}{Re_p}\left(1 + 0.15 Re_p^{0.687}\right) \tag{4.52}$$

To the extent that the particle's Reynolds number is sufficiently high ($1000 < Re_p < 2.10^5$), It is apparent in the figure that the steady-state drag coefficient becomes independent of the Reynolds number and approximately equal to 0.44.

Buoyancy force, F_B:

The gravitational force or buoyancy force per unit mass, denoted as $\mathrm{F_B}$, acts in the downward vertical direction. This force is directly proportional to the particle's mass and is determined by the disparity in density between the particle and the surrounding fluid:

$$F_B = \left(1 - \frac{\rho_f}{\rho_p}\right) g \tag{4.53}$$

In the rotating frame of reference, the additional rotation force can be expressed as:

$$F_R = (-2\boldsymbol{\Omega} \times \mathbf{V_p} - \boldsymbol{\Omega} \times \boldsymbol{\Omega} \times \mathbf{r_p}) \tag{4.54}$$

Virtual mass force, F_{VM}:

If the particle is accelerating through a fluid, it can cause the surrounding fluid to accelerate. In other words, more mass is accelerated compared to the mass of the particle itself. Consequently, there is a corresponding acceleration of the fluid which is at the expense of the work done by the particle [118]. the force needed to accelerate the virtual mass of the fluid in the volume occupied by the particle is referred to as the Virtual or Apparent Mass Force. The virtual force per unit particle mass leads to an additional drag expressed as follows [129]:

$$F_V = \frac{1}{2} m_f \frac{D}{dt} (V_f - V_p) \tag{4.55}$$

Pressure Gradient force, F_P:

the pressure gradient force per unit mass is important in regions exhibiting large pressure gradient which is defined as:

$$F_p = -\frac{m_f}{\rho_f} \nabla P \tag{4.56}$$

Both the virtual mass and pressure gradient forces are important if the fluid density is comparable to the particle density.

Turbulent Dispersion of Particles:

To account for the turbulent dispersion of particles, an additional force is considered by applying a particle dispersion model. In the RANS turbulent flow model, the instantaneous velocity of the continuous phase is decomposed into statistical mean and fluctuating components. The vector velocity of the flow field surrounding the solid particle, which is used in the momentum Equation (4.44) to calculate the forces exerted on the solid depends on the type of particle tracking. When the turbulent dispersion model is applied, the random nature of the instantaneous velocity is taken into account, and consequently, the trajectory of the individual particle within the continuous fluid may follow a different path if it was released from the same temporal and spatial conditions. The effect of turbulence on the particle dispersion within the continuous phase is predicted by a stochastic approach using Gosman and Loannides model [130]. the model assumes that the interaction between the turbulent eddy and particle occurs over a time interval which is the minimum of the eddy lifetime and the residence of the particle in the eddy. during this time interval, the velocity fluctuating components are added to the mean components to account for the effect of turbulence on the particle motion, where the latter is calculated using the local turbulent kinetic energy (K), [?, ?] and is defined as follows:

$$V_f' = \Gamma \left(\frac{2k}{3} \right)^{0.5} \tag{4.57}$$

Where Γ is a random number with a normal distribution that accounts for the randomness of turbulence about a mean value. Due to this randomness, each component of the changing velocity throughout each eddy may have a different value.

4.4.2 Particle solver control

the particle integrator operates independently of the standard CFD solver, necessitating the use of distinct control parameters. The crucial control aspect involves establishing the connection between the flow field solution and the particle trajectories integration [131].

4.4.2.1 Number of integration steps per element

This parameter governs the time step used for particle tracking integration. The time step is determined at a local level, computed by dividing the element length scale by the particle's velocity and the number of integration steps per element. Increasing the number of integration steps can enhance integration precision but comes at the cost of longer computation times. In the simulations conducted in this study, a value of 15 has been employed.

4.4.2.2 Maximum Tracking Time and distance

The maximum Tracking Time represents the actual time period over which particle integration takes place, while the maximum tracking distance pertains to the distance over which particle integration occurs. It's essential to configure these two parameters with sufficiently long and sizeable values to allow particles to traverse the geometry successfully. However, setting them excessively large could lead to an excessive computational burden when tracking particles that might get trapped in recirculation zones. In this research, particles were tracked for durations of up to 80 seconds and distances of up to 50 meters.

4.4.2.3 Maximum number of integration steps

The maximum number of integration steps can serve as a means to halt the tracking of particles that might become stuck in recirculation zones. It is determined by multiplying the number of integration steps per element by the count of elements that a particle crosses. In this particular investigation, this value has been set to 1000000 to allow sufficient time for particles to escape certain recirculation zones.

4.4.3 Erosion model

The exact form of the erosion rate equation is dependent on the properties of the impacting particle and target surface. However, for most metals, the erosion rate (E_r) can be generally expressed as a function of the impact velocity, angle, and properties of both the target surface and the impacting particle according to the relationship:

$$E_r = V_p^n f(\alpha) \tag{4.58}$$

Erosion is affected by the physical properties of the target material and erodent particles, such as particle concentration, shape, diameter, and impact. many experimental studies have been conducted to evaluate the erosion process, and data were used to develop an empirical correlation. The model due to Tabakoff and Grant is used to model the erosion rate in this study [61, 132]. The established empirical correlation estimates the erosion rate in terms of the ratio of the removed mass of the surface target to the mass of the impacting particles (mg/g):

$$E = K_1 f(\alpha) V_p^2 \cos^2\alpha \left(1 - R_T^2\right) + f(V_{PN}) \tag{4.59}$$

where:

$$f(\alpha) = \left[1 + K_2 K_{12} \sin\left(\alpha \frac{\pi/2}{\alpha_0}\right)\right]^2 \tag{4.60}$$

$$R_T = 1 - K_4 V_p \sin\alpha \tag{4.61}$$

$$f(V_{PN}) = K_3 \left(V_P \sin\alpha\right)^2 \tag{4.62}$$

$$K_2 = \begin{cases} 1 & \text{if } \alpha \le \alpha_0 \\ 0 & \text{if } \alpha > \alpha_0 \end{cases} \tag{4.63}$$

Where k_{12}, k_1, k_3, k_4 and are constants of the model and depend on the target surface and erodent particle combination; α is the angle between the impacting particle and the target surface; is the particle impact velocity; is the tangential recovery ratio; α_0 is the angle corresponding to the maximum erosion. The value of the constants contained in the Tabakoff and Grant model are listed in Table 4.4.

Tabakoff and Grant Constant	Value
k_{12}	0.293328
k_1	$6.53311 \,.\, 10^{5}$
k_3	$6.44096 \,.\, 10^{-11}$
k_4	$5.58 \,.\, 10^{-3}$
α_0	30°

Table 4.4: Coefficients used in Tabakoff and Grant model for Sand-steel combination.

The total erosion rate density resulting from all impacting particles on a specific area is related to the erosion rate computed from Equation (4.58) or from the exact erosion rate Equation (4.59) through the following formula:

$$E_R = \frac{1}{A} \sum_{p=1}^{N_{particle}} E \, \dot{n} \, m_p \tag{4.64}$$

Where $\dot{n}$ (s^{-1}) is the particle number rate; A is the mesh unit area (m^2); m_p is the particle mass; E (mg/g) is the erosion rate. The total erosion rate density E_R ($kg/m^2\,s$) is computed by recording all the impacting representative particles on a single mesh cell.

4.4.4 Particle Characterization and injection

The erodent particles consist of cement powder entrained by the fluid within the fan under investigation. These particles exhibit a range of distinct geometrical properties, necessitating an analysis of their size distribution.

To determine the size distribution of these particles, a discrete number frequency distribution is employed. In this research, the Mastersizer 3000 particle size analyzer is utilized to precisely characterize the particle size distribution (see Fig 4.8). This device relies on laser diffraction technology, which measures the size distribution of particles within a sample based on the principles of light scattering. The Mastersizer 3000 comprises several key components, including a primary optical unit and dry dispersion units (Aero S). These dispersion units serve the dual function of ensuring a uniform dispersion of dry powder and a consistent supply of the dry sample to the measurement cell via a continuous stream of air. The instrument's measurement cell is where the actual analysis occurs. Notably, the Mastersizer 3000 is capable of measuring particles within a size range that spans from 0.01 to 3500 μm. This wide measurement range allows for the comprehensive characterization of particle sizes present in the cement powder sample.

Figure 4.8: differential and cumulative particle size distribution.

The particle size distribution obtained using this method is volume-based [133]. The Mastersizer employs an equivalent volume approach to provide a singular number

Measurment Parameters	Values
Particle name	Cement
Dispersant Name	Dry Dispersion
Particle Refractive Index	1.68
Dispersant Refractive Index	1.00
Particle Absorption Index	0.1
Scattering Model	Mie
Weighted Residual	0.63%
Laser Obscuration	2.07%

Table 4.5: Analysis Report of the measurement data

representing irregularly shaped particles. This is accomplished by determining the diameter of an imaginary sphere that has an equivalent volume to the original particle.

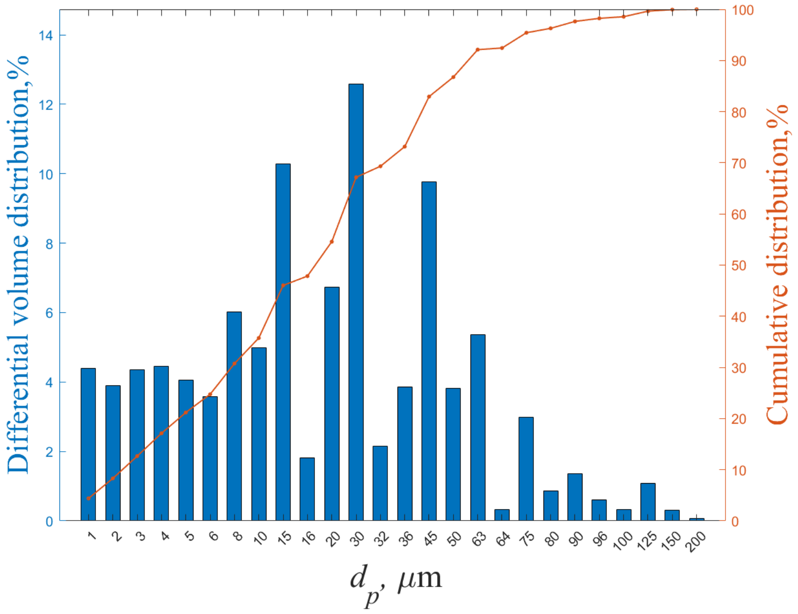

Figure 4.9: Differential and cumulative particle size distribution.

Figure 4.9 displays both the differential and cumulative particle volume distributions of the powder sample as a function of particle diameter. The cumulative size

Measurment Results	Values
Concentration	0.0011 %
Span	2.554
Uniformity	0.803
Specific Surface Area	445.9 m^2/kg
Dv (10)	2.4 μm
Dv (50)	16.2 μm
Dv (90)	60.7 μm
D [3,2]	4.27 μm
D [4,3]	17.8 μm

Table 4.6: Results of the measurement data

distribution curve provides essential insights, revealing that approximately 73% of the sample is composed of particles with a diameter smaller than 45,μm. To accurately represent the actual composition of the cement powder responsible for erosion, a polydisperse particle transport simulation is carried out. This simulation is based on the size distribution data depicted in Figure 4.9, and it incorporates the experimentally determined particle density ρ_p, set at 3150, kg/m^3.

the mass flow rate of injected particles at each particle tracking simulation was determined by taking into account the particle's concentration, the total volume flow rate of the carrier fluid, and the particle size distribution. under typical operating conditions, the concentration of particles is kept below 30 mg/m^3, but it can increase to high levels if the tissue in the bag filter upstream of the fan is damaged. for this reason, a numerical simulation was performed with a particle load ranging from 30 to 180 mg/m^3 to examine how the particle load alters the fan's erosion pattern and severity. the particle mass flow rates corresponding to a particle concentration of 30 mg/m^3 at the design flow rate, 0.74 $\mathrm{Q_d}$d and 1.78 $\mathrm{Q_d}$ are listed in Table 4.7:

Volume flow rate (m^3/s)	Particle mass flow rate (Kg/s)
$0.74Q_d$	0.0012
Q_d	0.001617
$1.78Q_d$	0.00288

Table 4.7: mass flow rate of injected particles for particle load of $30\,mg/m^3$.

The simulation of turbulent particle dispersion employs a stochastic method, necessitating the determination of an appropriate number of seeded particles to ensure statistically independent results. A thorough analysis of various aspects of particle dynamics, including impact location, frequency, and erosion patterns, is conducted to uphold result accuracy. It is crucial to acknowledge that, due to computational constraints, it is impractical to simulate the actual number of particles entrained within the fan domain. Consequently, the simulations consider a representative particle sharing the same geometrical and physical properties as the sampled particles. Each representative particle is characterized by a particle number rate denoted as N (1/s), representing the number of particles within a representative particle.

To assess the sensitivity of the results to the number of injected particles, the model is rerun for various particle numbers, starting from 300,000 injected particles, considering the experimental particle size distribution in this sensitivity analysis. The sensitivity analysis evaluates the ratio of the number of particles that impact the blade to the total injected particles and the erosion pattern on the blade pressure side. The analysis reveals a strong influence of the number of injected particles on all key parameters, including the erosion pattern on the blade pressure side (refer to Appendix A.8). Furthermore, erosion rates decrease as the number of injected particles increases, attributed to the decrease in number rate N (1/s) as per Eq. 4.64.

Through multiple simulation runs, it was determined that tracking a total of 1.5×10^6 particles is sufficient, justifying the additional computational cost of simulating more particle trajectories for each particle transport simulation. Additionally, to encompass the entire range of particle sizes, the number of representative particles assigned to each particle diameter category is defined as a fractional distribution based on the size distribution data.

Particles were injected randomly into the fan inlet section, applying a no-slip boundary condition that allows the particle to be released with the same inflow local velocities. It was assumed that particles colliding with surfaces would rebound, potentially striking the same surface or different ones. To account for the loss of particle momentum resulting from impact with walls, restitution coefficients of less than one were applied to all surfaces. In particular, when calculating the rebound velocity of particles, normal and tangential restitution coefficients were set at 0.8 and 0.9, respectively.

Chapter 5

Numerical simulation of the flow field and erosion process

5.1 Numerical results of the flow field

5.1.1 Numerical Validation of the Reference model

The numerical results of unsteady simulations were obtained by averaging time-varying values over the last revolution. To assess the convergence of the time-periodic results, Unsteady quantities such as the power shaft ($\mathrm{W_{shaft}}$) and the total pressure were monitored. Figure 5.1 depicts the time evolution of the total pressure at the impeller inlet section and the power shaft during the unsteady simulation at ($1.33\mathrm{Q_d}$). These graphs indicate that the unsteady solution starts to exhibit periodic behavior after at least 1.5 rotations of the impeller, following an initial period of instability.

Figure 5.2 and Figure 5.3 provide a visual representation of the comparison between the numerical and experimental aerodynamic performance of a centrifugal fan. The parameters under examination include the total pressure rise ($\Delta\mathrm{H_{total}}$), power shaft ($\mathrm{W_{shaft}}$), and total efficiency (η_{total}). The accuracy and reliability of our modeling approach are assessed by quantifying the discrepancies between the numerical results and the experimental data for the centrifugal fan investigated in this study. It is important to note that the computational demands of this specific case were substantial. The fine time-stepping and mesh employed necessitated an extensive computational effort, approximately 360 hours per operating point, using a computational system featuring

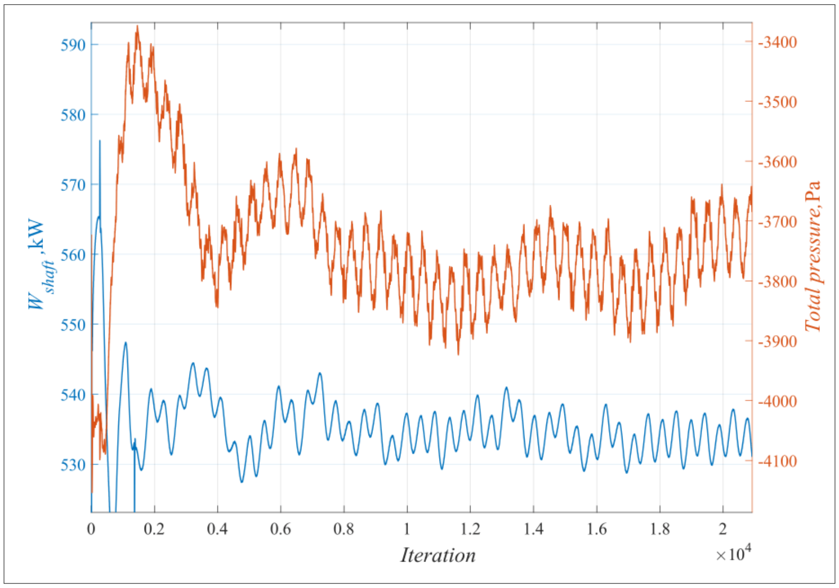

Figure 5.1: Time evolution of W_{shaft} and inlet total pressure

a 12-core CPU and 64 GB of RAM.

The mass-weighted average total pressure is computed by subtracting the total pressure at the impeller intake from that at the casing outlet. Furthermore, the fan's total efficiency is determined using (Eq.3.1), where the total torque involves the integration of the total moment along the axis of rotation (Z-axis), accounting for the combined effects of pressure and friction forces acting on all impeller wall surfaces.

The numerical results obtained through the unsteady simulation demonstrated a strong alignment with the experimental performance curve, indicating the validity of the numerical approach used for modeling the flow within the centrifugal fan. While the simulation results generally exhibited good agreement with the experimental data, certain disparities were noticeable. Specifically, the time-averaged total pressure rise was not accurately predicted for the design flow rate and off-design operating conditions. In cases of over-load operating conditions, the simulation tended to overestimate the total pressure rise, whereas it underestimated the numerical total pressure rise for flow rates below the Best effeciency point (BEP) operating range. Moreover, the power

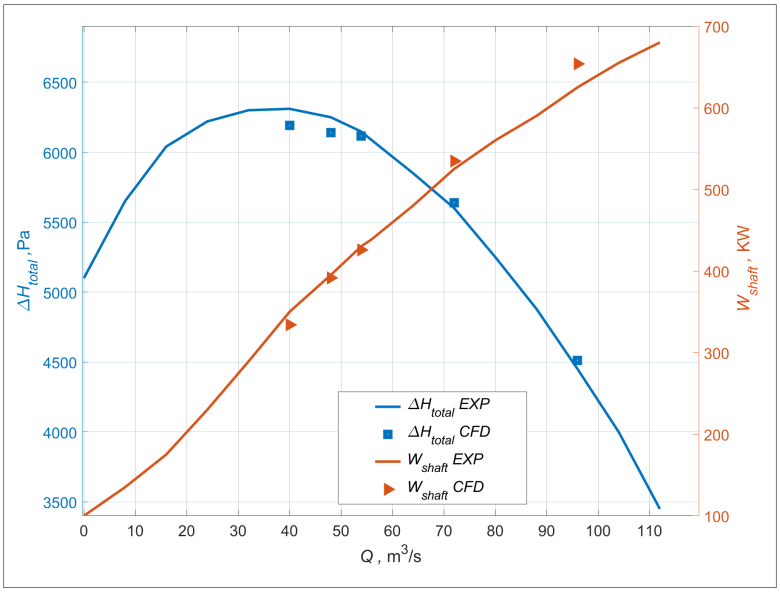

Figure 5.2: Numerical and experimental performance curve; ΔH_{total}, W_{shaft}.

shaft was overestimated, with a maximum deviation of 4.6% at a flow rate of $1.78Q_d$. Figure 5.2 offers further insights into the predicted power output, W_{shaft}, and reveals a noticeable correlation between the deviation in power output and the flow rate. The overestimation of W_{shaft} can be attributed to some significant oscillations, as depicted in Figure 5.1.

This observation highlights that while the numerical simulation captured the general trends in fan performance, it had some limitations when dealing with specific operating conditions, especially those deviating from the BEP. It's essential to emphasize that the discrepancies between the power shaft and total pressure rise, as calculated by the frozen-rotor simulation and the experimental data, are notably more significant when compared with the results obtained through the sliding mesh approach. The comparison is presented in Table 5.1 showing the power shaft values obtained from the steady simulation employing the frozen-rotor method.

As depicted in Table 5.1, the power output was consistently overestimated, with a peak deviation of 8.21% occurring at a flow rate of ($1.78Q_d$), and an average over-

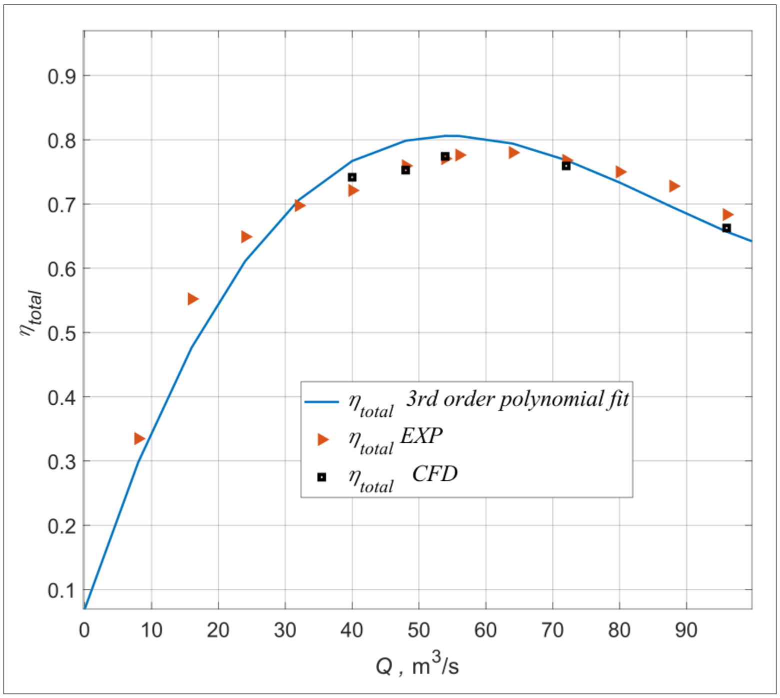

Figure 5.3: Numerical and experimental total efficiency ($\eta_{\mathbf{total}}$) curve of the fan.

estimation of 7.34%. These findings indicate that the computational modeling of the flow dynamics within the blade passage was not accurately resolved. While the primary drawback associated with employing the sliding mesh technique pertains to the increased computational demands necessitated by addressing rotor-stator interactions, the simplification of flow physics reveals important insights into the limitations of numerical accuracy when utilizing the frozen-rotor simulation for the prediction of overall fan performance. These observations lead to the conclusion that the steady simulation, particularly using the Frozen-Rotor approach, may not be considered reliable and sufficient, especially when examining the performance of typical large-sized centrifugal fans, where rotor-stator interactions are important. Consequently, it is inferred that solely relying on unsteady simulations becomes imperative for obtaining accurate predictions of aerodynamic performance within an acceptable margin of error in such cases.

Flow rate , [m^3/s]	40	48	53.9	72	96
power output, [Kw]	372.56	423.64	459.79	566.523	676.34
power output exp, [Kw]	350	395	430	525	625
Relative error, [%]	6.44	7.25	6.92	7.9	8.21

Table 5.1: Calculated power shaft with the Frozen-Rotor approach

5.1.2 Flow field characteristics

To illustrate various properties distribution of the flow field, a cross-sectional plane perpendicular to the axis of rotation is generated at the mid-span of the impeller outlet area (at a distance Z$_1$=0.14m from the impeller hub) as visualized in Figure 5.4. The pressure distribution is specifically presented in section Z$_1$ at the design flow rate (Q_d) because both the time-averaged and instantaneous static pressures exhibit nearly identical patterns across different sections of the impeller's span.

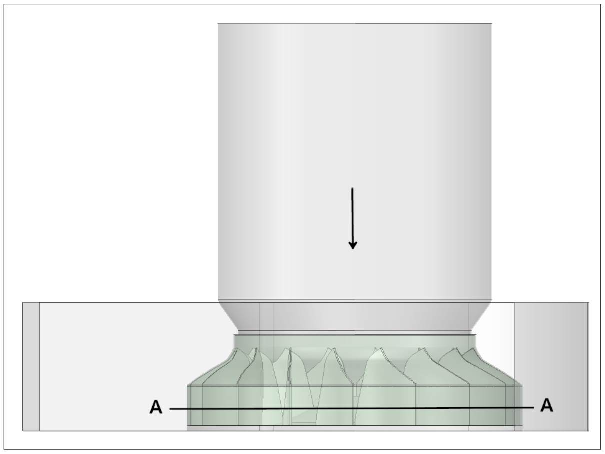

Figure 5.4: Cross section at mid-span of the blade (Z$_1$).

The time-averaged static pressure distribution within section Z$_1$ depicted in Figure 5.5 reveals an increase in static pressure as one moves from the impeller intake towards the casing outlet. This pressure rise occurs due to the transformation of dynamic pressure, generated by the impeller's rotation, into static pressure along the casing, accompanied by a sharp pressure gradient in the radial direction. This representation offers valuable insights into the evolving diffusion processes governed by the impeller, as well as the recovery of static pressure within the casing.

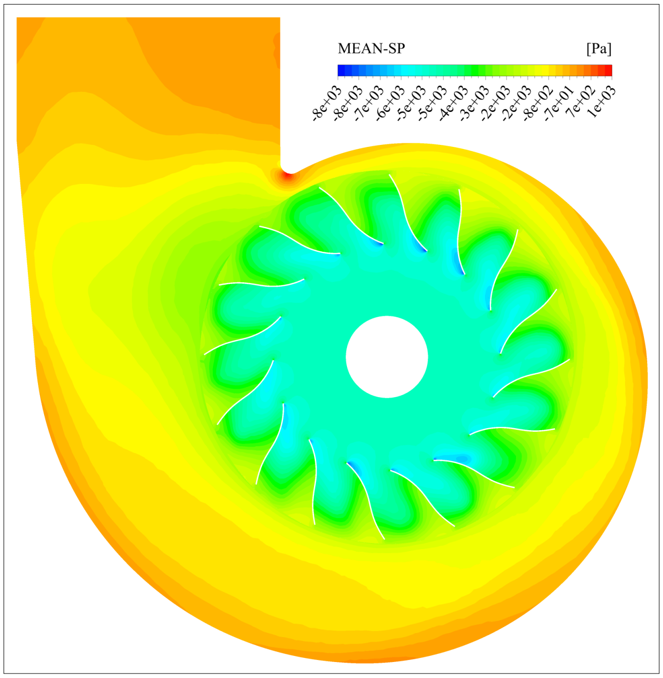

Figure 5.5: Time-averaged static pressure at Q_d

Within the hub region, a noticeable reduction in static pressure is observed. This can be attributed to the alteration of flow direction, transitioning from axial to radial, as well as the absence of flow guidance in this particular region. As the axial flow enters the hub region, it undergoes a radial turning, creating an adverse pressure gradient, leading to a decrease in pressure in the radial direction. This effect arises from the need for fluid particles to change their momentum to follow the curved path, which requires additional work to be done. Furthermore, the absence of flow guidance in the hub region allows the flow to expand and accelerate, further contributing to the reduction in static pressure. This is due to the fluid particles being unconstrained by walls or obstacles, permitting them to disperse and travel at higher velocities.

Conversely, at the tongue tip, the static pressure reaches its maximum value, coinciding with the occurrence of flow stagnation. Along the impeller blade passage, the static pressure is consistently higher on the blade's pressure side compared to the suction side. This gradient gradually intensifies from the impeller entry to the impeller outlet. Notably, the static pressure reaches its lowest value at the blade's leading edge tip, where the fluid's relative velocity attains its highest magnitude.

The instantaneous static pressure distribution shown in Figure 5.6 unveils a distinctive behavior. As the fan blade past the casing tongue, a noticeable trend emerges: there exists a comparatively elevated static pressure on the blade's pressure side. This pattern, however, experiences a transition as the blade continues its rotation from the casing throat to the wider discharge section of the volute. During this phase, the static pressure on the blade's pressure side undergoes a decrease. This non-uniformity in pressure distribution along the blades is primarily attributed to the geometrical asymmetry of the volute. These variations in the volute's design result in differing pressure levels encountered by the blade as it rotates, giving rise to the observed pressure fluctuations.

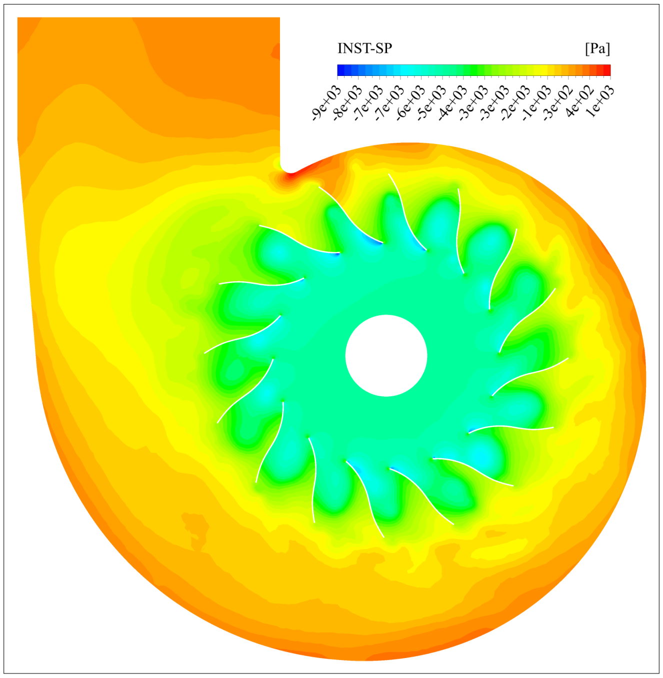

Figure 5.6: Instantaneous static pressure at Q_d.

The analysis of the unsteady dynamic interaction between the impeller and the casing involves the assessment of the root-mean-square of the static pressure field, labeled as P_{rms}, within section Z_1 at Q_d. Figure 5.7 visually illustrates the distribution of P_{rms}, and its mathematical representation is provided as follows:

$$P_{rms} = \sqrt{\sum_{i}^{n} \left(P_i - \bar{P}\right)^2 / n} \tag{5.1}$$

where: P_i is the static pressure fluctuation over the time history of one revolution, P is the time-averaged static pressure over a single revolution, and n is the number of samples. It's crucial to distinguish between the statistical mean derived from Reynolds decomposition and the mean employed in Equation 5.1. The root-mean-square value, denoted as P_{rms}, serves as an indicator of the extent of fluctuation attributed to the dynamic interaction between the impeller and the casing, rather than turbulence fluctuations.

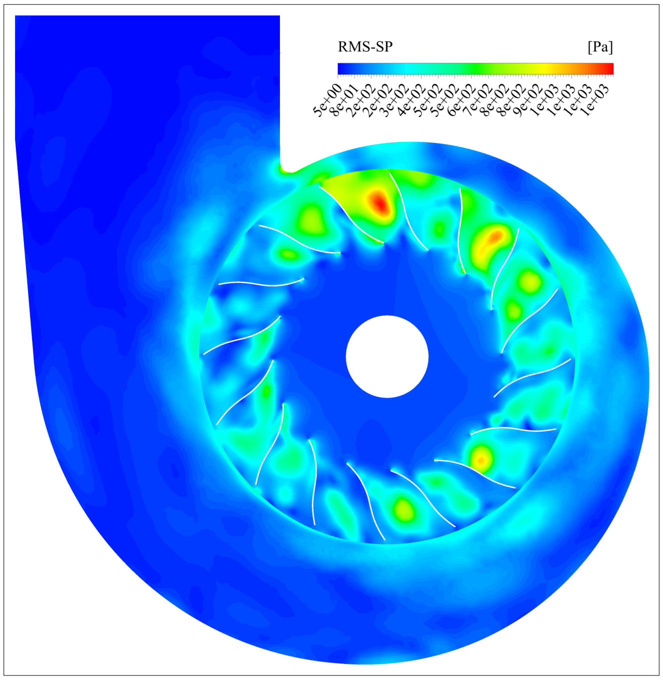

Figure 5.7: P_{rms} distribution at Q_d.

The distribution of P_{rms} exhibits higher values within the impeller blade passage and the casing throat region. Importantly, these values are not uniformly distributed throughout each blade passage. The most significant static pressure fluctuations are observed within the impeller blade passage, particularly on the blade's suction side, where there is a prominent occurrence of flow separation and recirculation. Additionally, substantial fluctuations are noted at the blade's leading edge, where the relative velocity of the incoming flow is highest. These pronounced fluctuations are most noticeable in the blade passages downstream of the casing tongue, where the interaction between the rotating impeller and the stationary volute is most pronounced. The root-mean-square of static pressure can reach a maximum value, of approximately 23 % of the reference pressure (p_{ref}). The pressure distribution and the fluctuation strength within the blade passage are influenced by the unsteadiness resulting from these interactions, a behavior that cannot be adequately captured using the frozen-rotor approach.

Figures 5.8-5.10 provide graphical depictions of the instantaneous velocity field contours, along with superimposed normalized velocity vectors, within section Z_1. These visualizations correspond to flow rates of $40\,\mathrm{m^3/s}$, $\mathrm{Q_d}$ ($53.9\,\mathrm{m^3/s}$) and 96 $\mathrm{m^3/s}$. Additionally, 2D streamlines, within the impeller domain, are also shown within section Z_1. The velocity data is presented with respect to the appropriate frames of reference. This includes displaying contours of relative velocity magnitude within the impeller domain, considering the moving reference frame, as well as the absolute velocity magnitude concerning the inertial reference frame within the casing domain.

The evolution of 3D flow dynamics within the impeller region displays consistency across the three distinct operating conditions. At the entrance of the impeller, the flow exhibits a radial direction, and the distribution of volume flow rates is symmetrical. Nevertheless, interactions between the impeller and the volute walls introduce fluctuations in the flow field within each blade-to-blade passage. These fluctuations give rise to distinctive flow characteristics stemming from the asymmetrical geometry of the volute. As the blades rotate, the flow experiences alterations in counter-pressure within each blade passage, contingent upon the blade's angular position relative to the volute

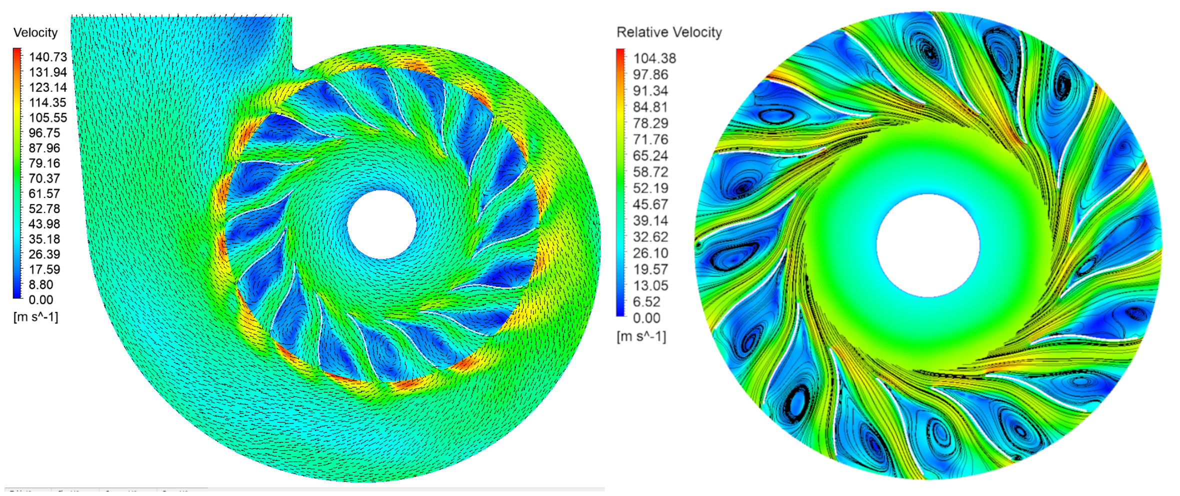

Figure 5.8: Relative velocity contour and streamlines on the section Z1 at $0.74Q_d$.

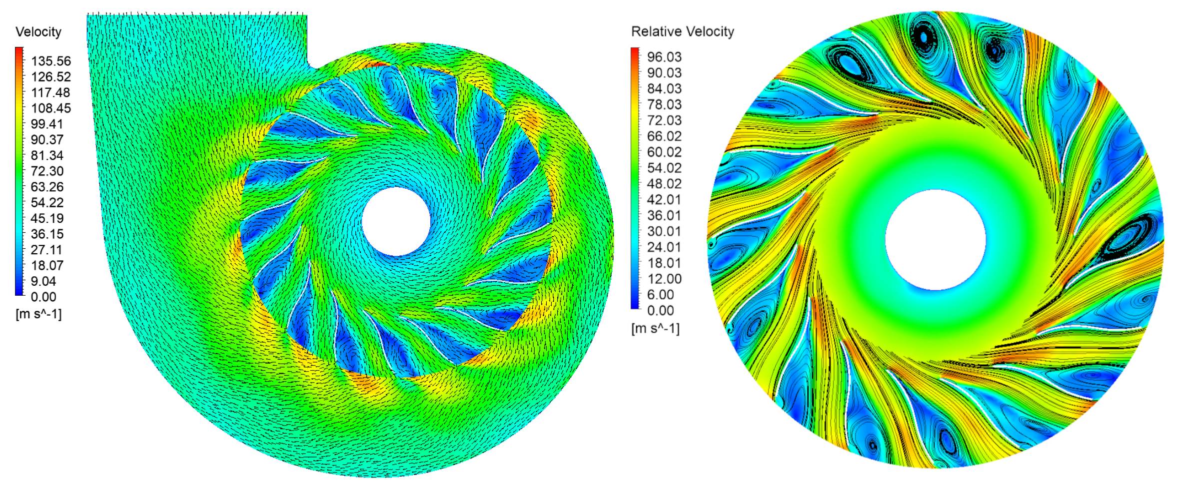

Figure 5.9: Relative velocity contour and streamlines on the section Z1 at Q_d.

tongue. This asymmetry in the volute geometry is responsible for these variations, which manifest as discernible features in the flow dynamics.

The velocity characteristics of the flow within the casing domain exhibit consistent behavior across the three flow rates. This behavior is characterized by a notable velocity

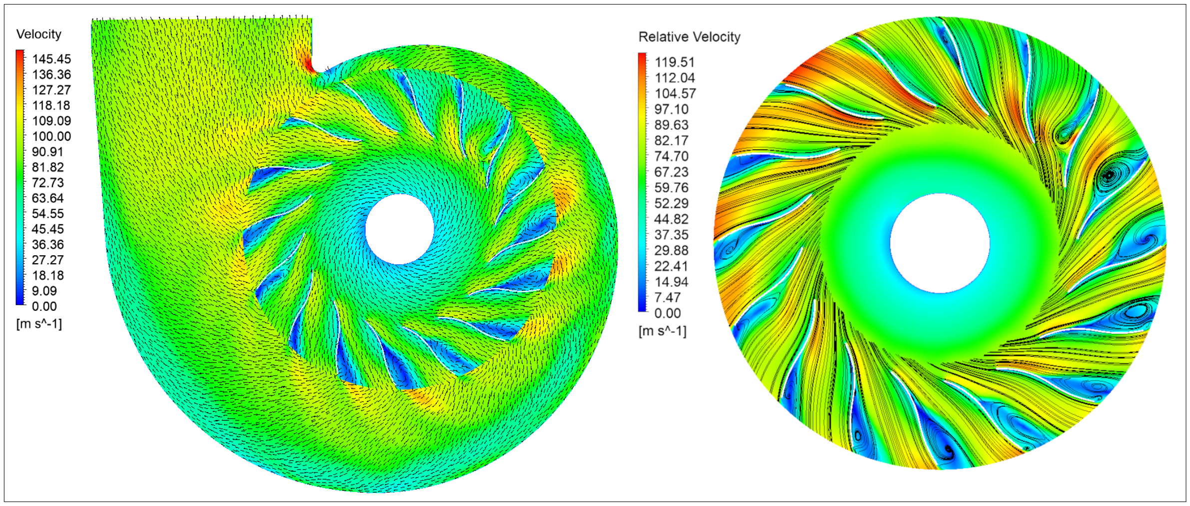

Figure 5.10: Relative velocity contour and streamlines on the section Z1 at $1.78\mathbf{Q_d}$.

gradient in the radial direction, with a pronounced flow acceleration occurring near the trailing edge at the interface between the impeller outlet and the casing domain. This acceleration results in exceptionally high local velocities, reaching values of up to $1.2U_2$. As the flow enters into the volute, there is a gradual decrease in velocity, as the kinetic energy of the flow is converted into static pressure. It's important to highlight that, the stagnation point for the flow rate of $96\,\mathrm{m}^3/\mathrm{s}$ is shifted towards the casing throat compared to the Q_d and $40\,\mathrm{m}^3/\mathrm{s}$ operating points. Specifically, the blade channel that passes in front of the volute tongue exhibits a progressive distortion of the high-velocity flow at the impeller outlet. This dynamic instability becomes more pronounced with higher flow rates, particularly evident in the overload operating point.

The velocity contours also indicate that there are areas where the flow separates in the blade passage near the blade suction side for all three working conditions. These areas, which affect most of the blade passage at the design flow rate and at the part-load operating point, are characterized by low velocity and recirculating flows. The blade inlet angle and blade curvature strongly influence the flows at the impeller entry and blade passage, leading to inevitable flow separation primarily near the blade suction side. However, it is noteworthy that at the overload operating regime (as shown in Figure 5.10), the extent of the flow separation is attenuated in the passages near the casing tongue that face the larger cross-section of the volute and the casing throat. The blade passage upstream of the volute tongue, in contrast, does not experience any flow separations.

5.2 Particle dispersion and Erosion process

5.2.1 Particles trajectories

This section explores the analysis of particle trajectories tracked along their paths. The particles were injected based on particle diameter and mass distribution, as introduced in (Section 4.4.4), to explore the impact of particle size on their dynamics within the fan domain. Solid particles were injected into the instantaneous flow field solution under three operating conditions (i.e., $0.74Q_d$, Q_d, and $1.78Q_d$). The path lines of particle samples were color-coded according to particle velocity. Two size classes were delineated for illustrative purposes: Small Size Particles (Small-Size particles (SSP)) with particle diameters $d_p < 30, \mu m$ and Large Size Particles (Large-Size particles (LSP)) with diameters ranging from $30, \mu m$ to $200, \mu m$. Figure 5.11 demonstrates the trajectories of SSP through the blade passage, highlighting their dynamic interactions with the impeller blade and impeller back plate surface. Likewise, Figure 5.12 portrays their path lines through the impeller and casing domains. Similarly, Figures 5.13 and 5.14 depict the trajectories of LSP across the blade passage and the entire fan domain, respectively.

It is noteworthy that, based on the particle trajectories observed for both diameter classes, particle transport varies significantly, particularly in the blade passage and the casing domain. Nevertheless, irrespective of particle size, the airflow drives particles in an axial direction from the inlet cone to the rotating impeller domain. For particles situated closer to the inlet cone wall surface, they enter the blade passage directly from the top near the shroud surface, impacting the top fore part of the blade pressure side (near the blade-shroud junction). Following rebound, they undergo further impact over the blade pressure side at mid-span before being deflected to exit the impeller without causing additional impacts on the trailing edge aft. In contrast, particles within the inlet core flow rotate with the turning fluid in the impeller hub domain before entering the blade passage.

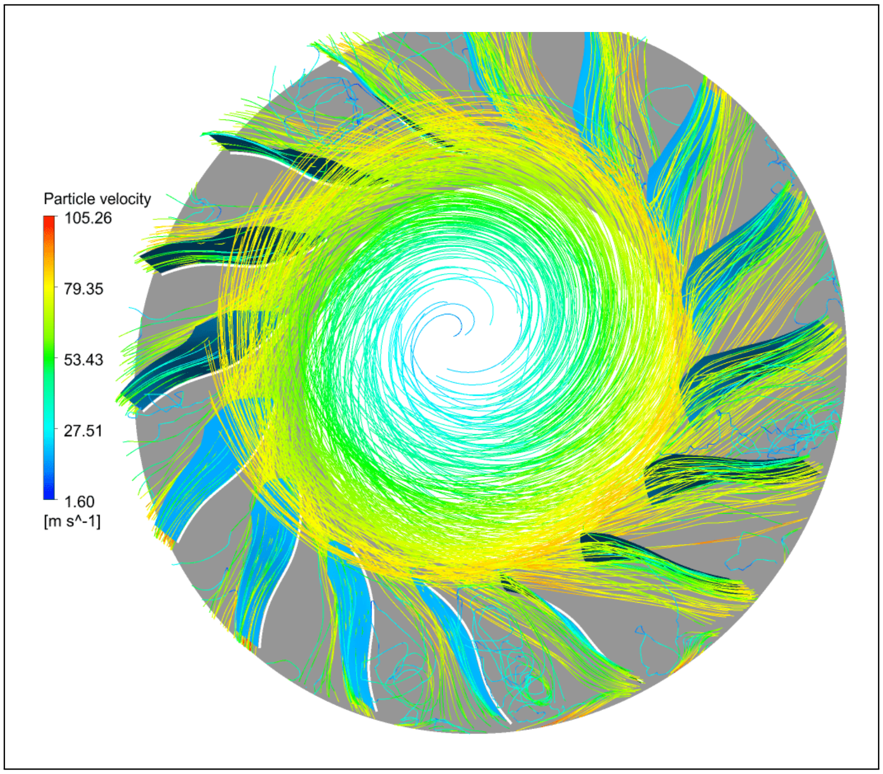

Figure 5.11: Samples of particle trajectories (SSP) through the blade passage at Q_d.

The deviation of particle trajectories from the airflow streamlines is determined by the predominant forces acting on them, and this is influenced by both their size and inertia. The size of the particles can be correlated with the turbulent Stokes number (Stk), which represents the ratio of the time a particle takes to respond to changes in fluid flow to the characteristic time scale of the fluid flow. This crucial

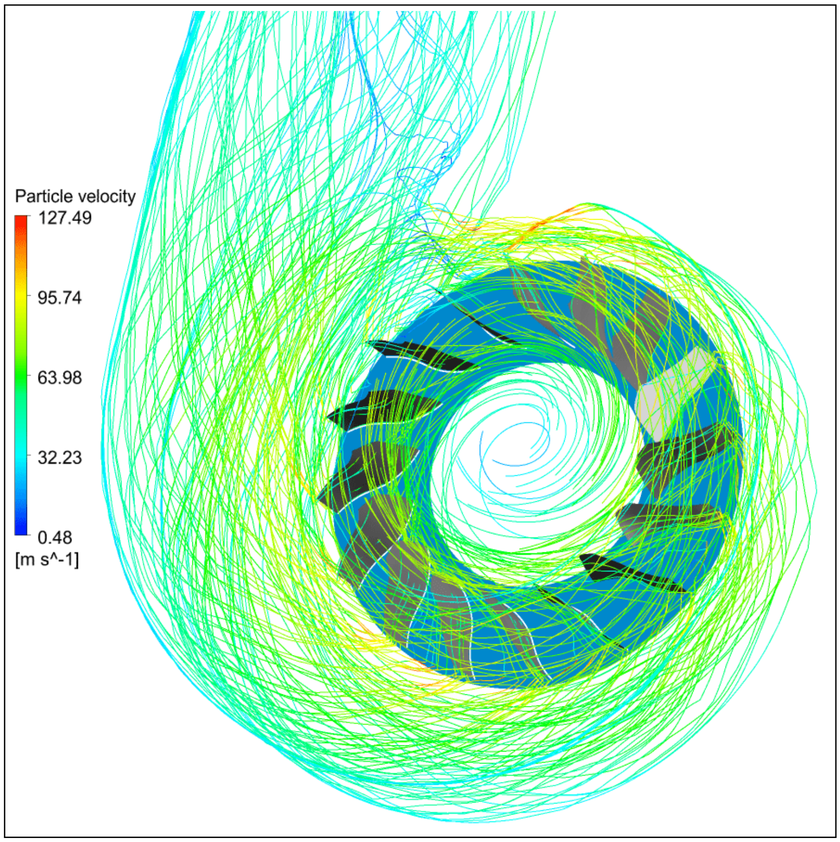

Figure 5.12: Samples of particle trajectories (LSP) through the fan domain at Q_d.

parameter indicates the extent to which the particle path deviates from the flow of the fluid. The behavior of particles with various Stokes numbers in turbulent flows is intricate and relies on specific flow conditions and particle characteristics. Nevertheless, the turbulent Stokes number serves to characterize the relative significance of particle size and turbulence in governing particle transport and dispersion. When a particle possesses a Stokes number approaching unity, it is strongly influenced by the fluid and can closely adhere to the flow path.

Small-size particles (SSP) traveling the fan domain exhibit a small turbulent Stokes number, typically ranging between 2 and 5, attributable to their low inertia. This characteristic renders them notably susceptible to viscous drag, resulting in a pronounced tendency to adhere closely to the airflow path. As depicted in Figure 5.11, SSP enter the blade passage from the hub to the shroud of the blade channel. The predominant particle flux makes direct contact with the entire surface of the blade's pressure side, with numerous incident particles impacting the blade's fore and mid-sections before rebounding and causing additional impacts at a low angle prior to reaching the trailing edge at a velocity of approximately 80,m/s, following a momentum loss from their impact. While certain incident particles travel in proximity to the blade pressure surface and strike the blade aft along the trailing edge before exiting the impeller without further impact, several particles manage to traverse the blade passage without causing impacts on the blade's pressure and suction side surfaces before exiting the impeller at a velocity of about $0.9, U_2$, owing to the high local fluid velocity. The trajectories of small particles are significantly influenced by the flow recirculation occurring in the blade passage near the blade suction side. In these regions,the particles behave like a passive scalar and are driven downwards from the shroud to the impeller hub by the flow vortex, potentially resulting in a high Impact frequency (IF) near the blade suction side where flow recirculation is strong.

After traversing the blade passage and entering the interface between the impeller and the volute,(SSP) promptly respond to alterations in the flow field as they shift from the rotating to the stationary frame. They undergo a change in direction and experience acceleration, attaining high velocities at the impeller exit. As illustrated in Figure 5.12, the efflux of particles collected at the trailing edge can achieve maximum values of up to $1.1, U_2$. The particles are influenced by the flow field within the casing domain while progressing from the volute's throat to its larger section. They undergo a directional shift with respect to the inertial frame, either colliding repetitively against the casing wall or following the fluid flow to the casing outlet without causing any impact. Due to their elevated speed in the casing throat region, they impact the volute's facing surface with substantial velocities. However, their velocity diminishes in the larger section of the volute, characterized by a steep velocity gradient toward the radial direction, resulting in infrequent impacts and low velocities on these casing surfaces. Ultimately, the particles decelerate to a velocity of 50 m/s or even lower at the casing outlet.

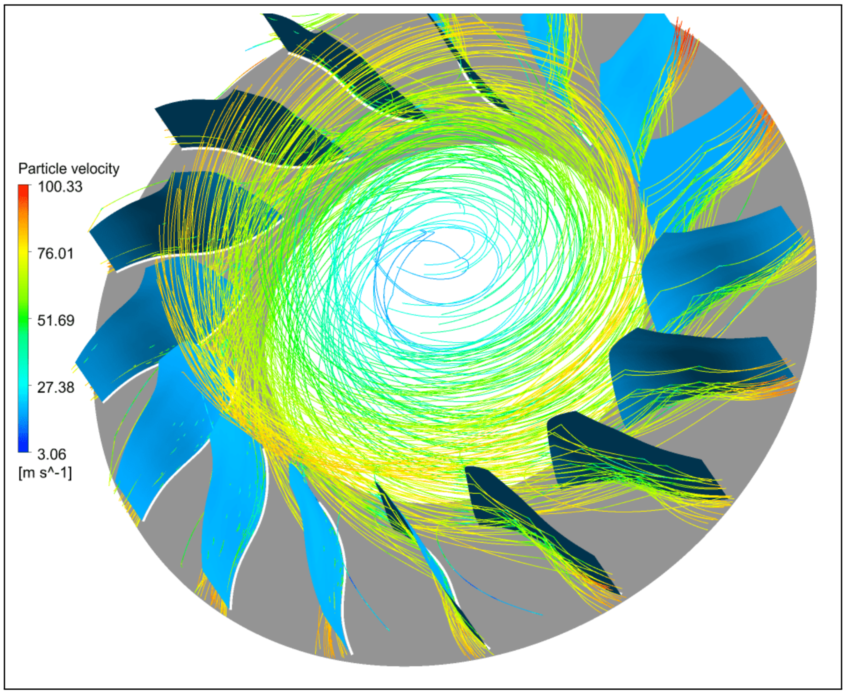

Figure 5.13: Samples of particle trajectories (LSP) through the blade passage at Q_d .

In contrast to small-size particles, large-size particles (LSP) undergo more significant centrifugation and inertia, leading to substantial deviations from fluid pathlines and downward deflection within the blade passage. As depicted in Figure 5.13, the blade mid-span near the hub, the fore part of the blade pressure side, and the blade leading edge are particularly susceptible to particle impacts. When larger particles enter the blade passage close to the blade suction side, they are directed toward the subsequent blade pressure side at 50% of the blade chord with a moderate incidence angle before being deflected to the impeller outlet without additional impacts. However, particles entering the blade passage near the blade pressure side strike the blade surface at a low angle of incidence. The primary particle flux is observed to impact the blade pressure side and the impeller hub before exiting the impeller, with several particles striking the blade leading edges at a high impact angle before returning to the blade channel. Particles with a low impact angle bounce off the pressure side, reaching the trailing edge after multiple impacts. This category of particles is more prone to generating a high impact frequency than smaller particles due to their heightened inertia, causing them to impact the impeller hub before entering the blade passage.

Figure 5.14 illustrates the coalescence of large-size particles along a band that faces the impeller outlet within the casing domain. Upon exiting from the impeller, these particles undergo acceleration, achieving substantial velocities of up to 122 m/s at the impeller-casing interface. Owing to their elevated inertia and significant Stokes number, these class of particles follow a linear trajectory, resulting in forceful collisions with the casing wall. Their impact on the volute surface persists until they reach the casing outlet, where their velocity decreases to 30 m/s due to impact-induced loss and the exchange of fluid forces.

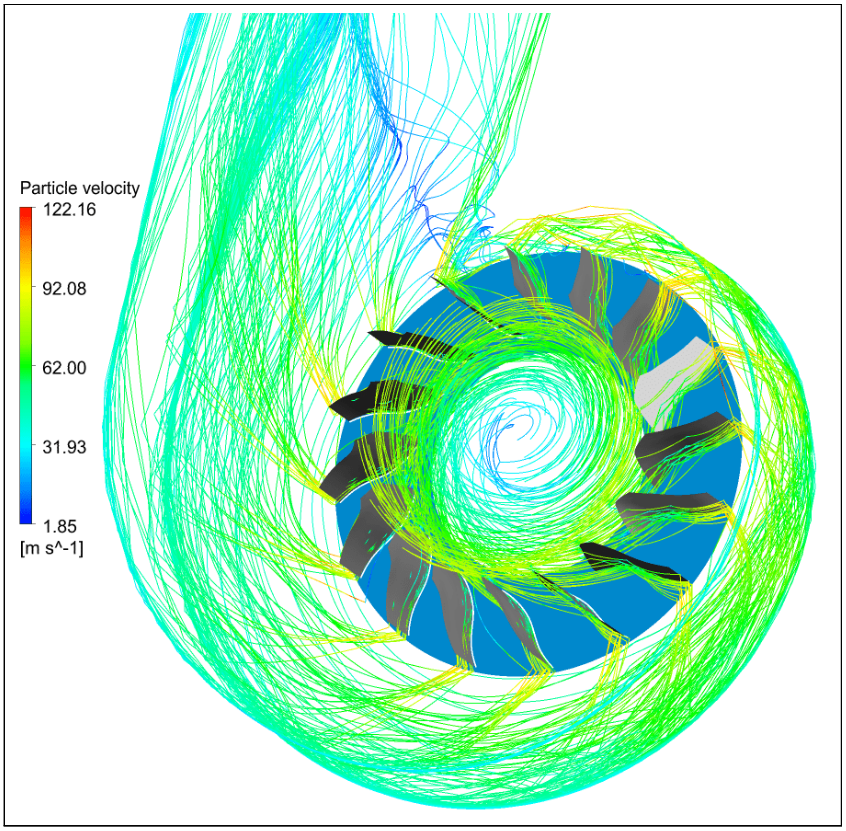

Figure 5.14: Samples of particle trajectories (LSP) through the fan domain at Q_d.

5.2.2 Particle impact characteristics and erosion assessment

To gain insight into the impact characteristics and distribution of both Small-Size Particles (SSP) and Large-Size Particles (LSP), each individual particle impact was recorded on the most critical boundary surface of the fan. A dot was utilized to represent each impact in Cartesian coordinates. These dots were then colored based on particle diameter, as well as impact parameters such as impact velocity and impact angle. Subsequently, they were superimposed on the target surface and depicted in contour. Figure 5.15 showcases the frequency distribution of particle impacts on the blade pressure side within the considered particle size classes. Additionally, Figures 5.16 and 5.17 illustrate contours depicting the velocity and angle at which the impacts occur, respectively

As depicted in Figure 5.15, the distribution of impacts on the blade pressure side surface exhibits notable distinctions between the two size classes. In Figure 5.15(a), the impact distribution of large-size particles reveals that areas more susceptible to impacts include the fore and lower mid-span of the blade surface, along with the leading-edge strip. Additionally, the central region of the blade is affected by particles rebounding from the leading-edge strip. However, no impacts are observed at the blade tip or the second part of the blade mid-span near the shroud. Consistent with the particle trajectories depicted in Figure 5.13, a peak impact region near the blade root is evident, occurring at 50% of the blade chord.

As indicated in Figure 5.16(a), the majority of large-sized particles hit the blade pressure side surface, exhibiting velocities in the range of 60,m/s to 80,m/s. However, particles that are directly propelled onto the blade surface experience higher impact velocities, reaching a maximum of up to 110,m/s near the trailing edge. Notably, these particles undergo a singular impact on the blade surface, avoiding momentum loss from multiple collisions. In Figure 5.17(a), it is observed that the most common instances of large-size particle impacts on the blade surface occur at low impact angles. Nevertheless, impacts in specific regions, such as a band near the blade root at the mid-cord of the blade and the top fore part of the blade, happen at an impact angle close to 30°—coinciding with the angle associated with maximum erosion. Owing to the heightened impact velocities in these blade regions, particles of this size class play a substantial role in contributing to erosion on the blade pressure surface in these particular areas.

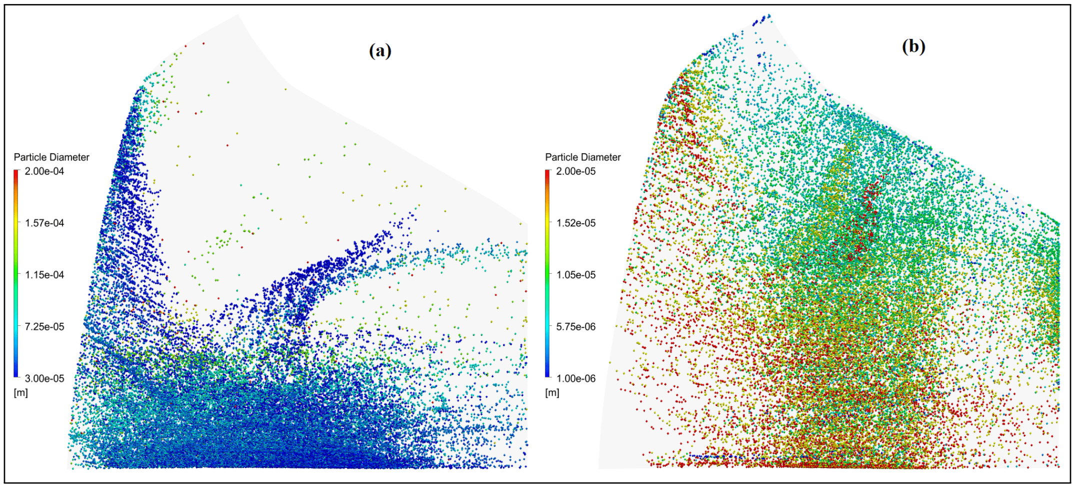

Figure 5.15: Particle impact on the blade Pressure side colored by particle diameter: (a) LSP; (b) SSP.

According to Figure 5.15 (b), small-size particles impact the blade pressure side surface uniformly. An analysis of the particle diameter distribution on the blade surface reveals that smaller particles are more prone to striking the blade tip compared to their larger counterparts. Additionally, it is apparent that the mid-cord, upper fore part, and near the trailing edge of the blade are particularly susceptible to particle impacts.

In Figure 5.16 (b), it is depicted that the velocity of particle impact on the mid-cord region is approximately 40,m/s for small-size particles, with higher values observed in the upper fore part of the blade and near the trailing edge due to the high efflux fluid velocity. Small particles predominantly impact the blade surface at a low angle, except for the mid-cord region near the impeller hub and the top part of the leading-edge strip, as shown in Figure 5.17 (b). The impact angle distribution reveals a consistent pattern of particle impact angles across both diameter classes.

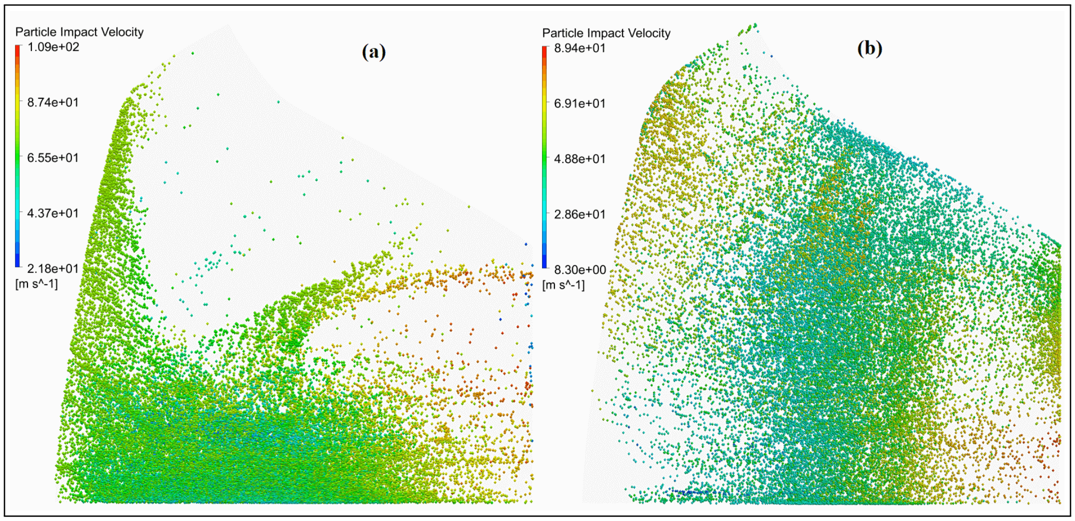

Figure 5.16: Particle impact on the blade pressure side colored by impact velocity:(a) LSP; (b) SSP.

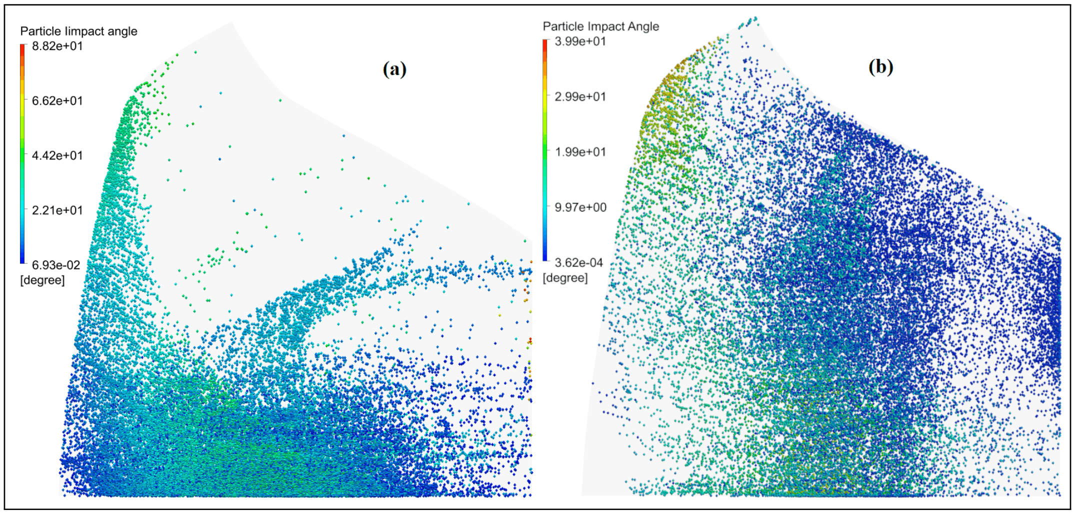

Figure 5.17: Particle impact on the blade PS colored by impact angle:(a) (a) LSP; (b) SSP.

Figure 5.18 illustrates the frequency of particle impacts on various components of the fan, including the blade's leading edge, pressure side, suction side, and the impeller hub. This illustration aims to assess how particle size influences erosion patterns and contributions. According to the figure, the frequency of impacts on the pressure side of the blade is nearly identical for both particle size categories. Despite small-size particles constituting more than 55% of the total particle release (as indicated in Figure 4.9), large-size particles contribute to 54% of all impacts on the blade's pressure side. This difference can be attributed to the fact that some small particles do not hit the blade's surface as they pass through the blade passage (as depicted in Figure 5.11), while larger particles are more likely to undergo repeated collisions with the pressure side of the blade after bouncing off its surface.

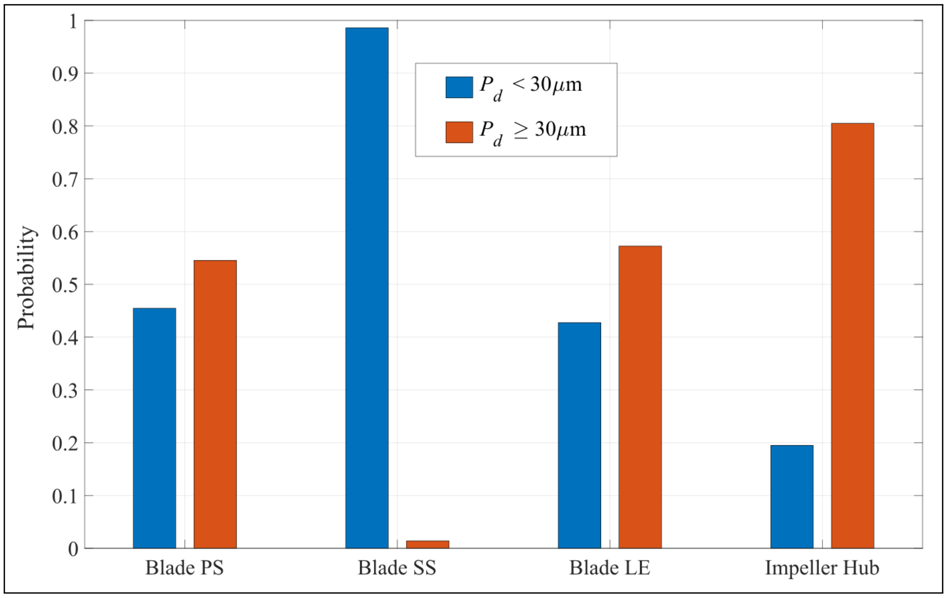

Figure 5.18: Dispersion of impacts of different Particle Size classes on the Principal Components of the Rotor.

The predominant area of impact by large-size particles on the blade surface is concentrated in a specific region of the blade's lower midspan. However, analyzing only the distribution of impact frequencies for the two-particle size classes is insufficient for determining which size class contributes the most to erosion on the blade surface. This is because a comprehensive assessment requires an examination of both the velocity and angle at which impacts occur for both size classes simultaneously. To address this, Figure 5.19 illustrates the distribution of impact velocities (recorded in increments of 10 units), and Figure 5.20 presents the impact angles (recorded in increments of 5 units).

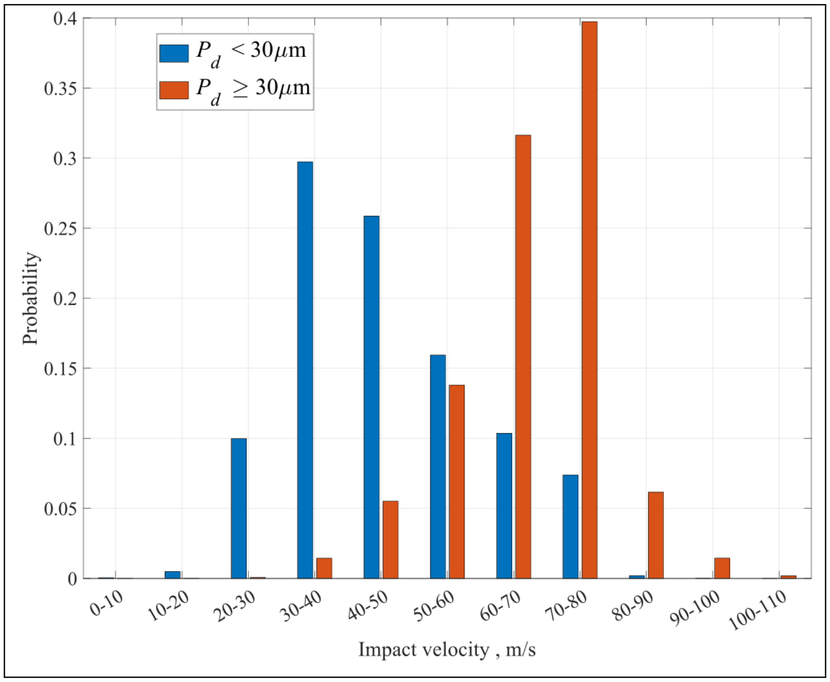

Figure 5.19: Dispersion of Impact velocities on the blade pressure side.

The bar chart depicted in Figure 5.19 illustrates the probability distribution of impact velocities on the surface of the blade pressure side for the two distinct particle diameter classes. Impact velocities cover a range from 0 to 110,m/s and are segmented into 11 intervals. Examining the graph reveals that at lower impact velocities (0-20,m/s), the likelihood of impact for both small and large particles is relatively minimal. As impact velocities increase, the probability of impact increases for both particle size classes. This pattern persists until the impact velocity reaches 30-40,m/s, where the impact probability for small particles peaks at approximately 0.3. Subsequently, the probability decreases, reaching zero at impact velocities beyond 80m/s. For large-size particles, the probability of impact attains a maximum value of around 0.397 within the velocity range of 70-80,m/s. Following this range, the probabilities for both small and large particles diminish at higher impact velocities (90-100,m/s and 100-110,m/s). This trend holds significant implications for the erosion process, suggesting that large-size particles are more likely to cause severe damage to the blade compared to smaller ones. This heightened probability of impact at high velocities is attributed to the increasing influence of inertia and centrifugation as particle size increases.

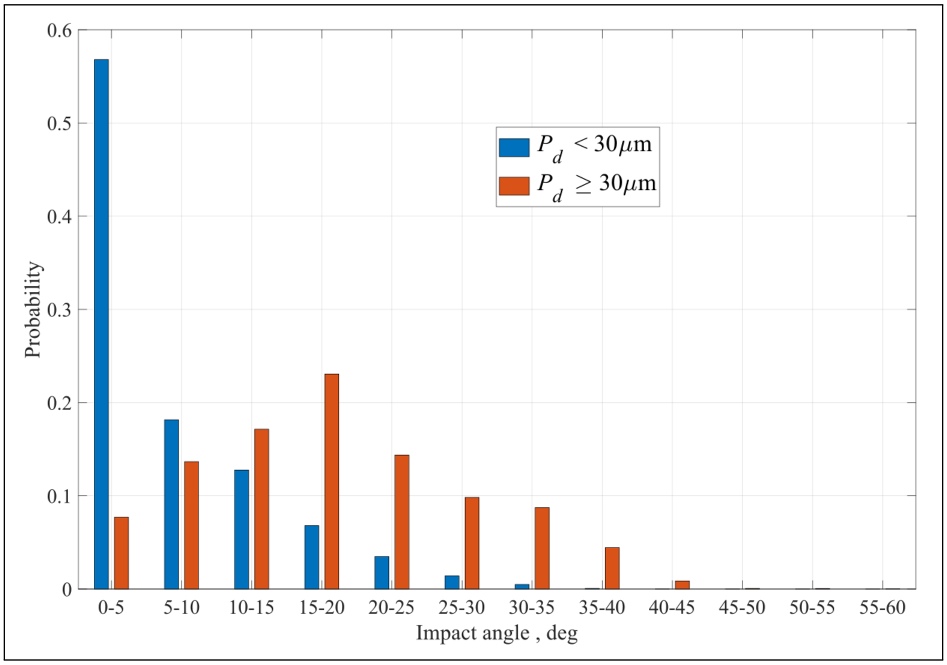

Figure 5.20: Dispersion of Impact angles on the blade pressure side.

The histogram presented in Figure 5.20 illustrates the probability distribution of impact angles on the surface of the blade pressure side for two distinct particle diameter classes. The impact angles span from 0° to 60°, divided into 11 intervals. The peak probability of impact for small-size particles occurs within the angle range of 0°-5°, reaching a maximum probability of 0.57. In contrast, the highest probability of impact for large-size particles is observed in the range of 15°-20°, with a maximum probability of 0.17. It is noteworthy that an impact angle of 30 degrees leads to maximum erosion. The histogram indicates that large-size particles have a relatively elevated probability of impacting the blade at an angle close to 30°, with 24% of the impact angles falling between 20°–30°. This representation offers valuable insights, suggesting that large-size particles have the potential to significantly contribute to blade erosion. Considering the combined influence of impact angle and velocity during the fan design stage may be essential to mitigate their effects and reduce blade erosion.

Figure 5.21 illustrates a significant erosion rate on the blade pressure side. The figure displays the erosion rate density contour for a particle concentration of 30,mg/m^3 at the design volume flow rate Q_d. Furthermore, Figure 5.22 showcases a typical erosion pattern observed on the pressure side of the blade during operation. This pattern served as a basis for comparing the results obtained from the numerical analysis with the actual erosion patterns observed during inspections.

The comparison between the erosion pattern depicted in Figure 5.21 and the on-field erosion pattern shown in Figure 5.22 validates the capability of the numerical model developed in this study to faithfully reproduce the actual erosion pattern resulting from solid particle impact on the blade's pressure side. Significant erosion predominantly occurs in regions near the hub in the mid-span part of the blade and the top fore part of the blade, where there is a concentration of large-size particles impacting the blade surface. The scattering of erosion at the center of the blade is attributed to particles rebounding off the leading-edge strip, while minimal wear is evident on the rest of the blade surface. The most severe erosion is observed in the blade root region at around 50% of the blade chord.

Although the entire blade surface is exposed to small particle impact, noteworthy erosion is only apparent in regions impacted at an angle between 20-30 degrees, as indicated by the impact angle distribution in Figure 5.17-b. This observation implies that larger particles are more likely to induce severe erosion compared to their smaller counterparts. Minimal to no erosion occurs when smaller particles impact at moderate velocity and a low impact angle, underscoring the pivotal role of impact angle in determining the erosion rate. For most ductile metals, the maximum erosion typically occurs at an angle between 20 and 30 degrees.

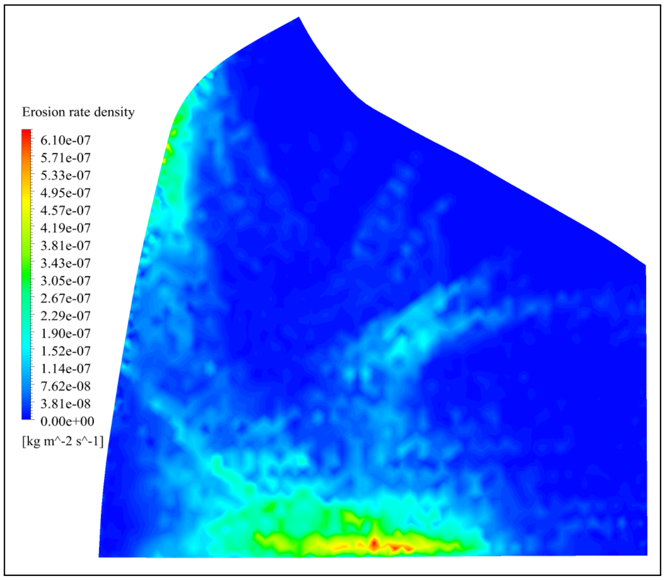

Figure 5.21: Erosion rate density on the Blade PS at Q_d.

Figure 5.22: In-service erosion inspection of the Blade pressure side .

According to the impact distribution chart in Figure 5.18, it is clear that the blade suction side experiences impact predominantly from small-sized particles. The majority of these particles hit the blade suction side at low angles and moderate impact velocities, as shown in Figure 5.23. However, the frequency of these impacts is not enough to cause substantial erosion on the blade suction side. In contrast, the leading edge faces high impact frequency and high-velocity impacts from all particles, with the highest velocity observed at the top. These particles collide with the leading-edge surface at both normal and approximately 35° angles at the top, leading to a notable erosion rate in this specific area of the leading edge.

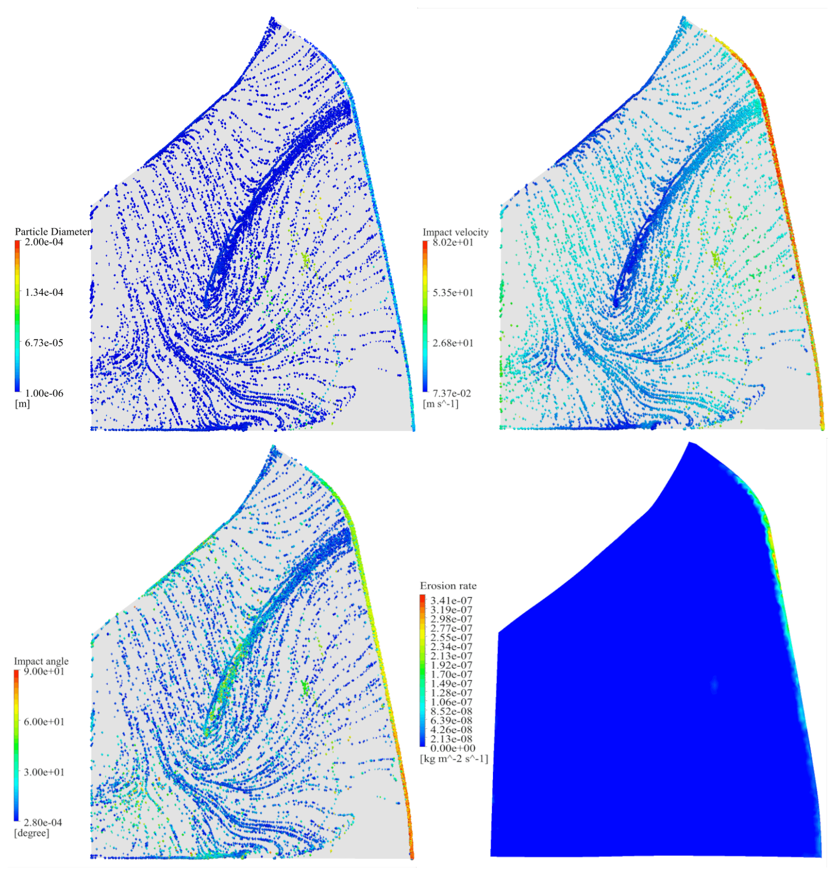

Figure 5.23: Blade SS Erosion rate density at Q_d.

Figures 5.24 through Figure 5.26 illustrate the particle impact distribution on the impeller hub, with color-coding representing particle diameter, impact velocity, and impact angle, respectively.

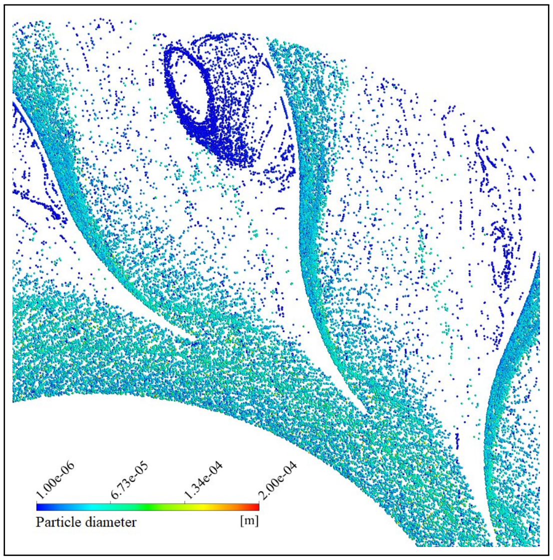

Figure 5.24: Impact on the impeller hub colored by particle diameter at ($\mathbf{Q_d}$).

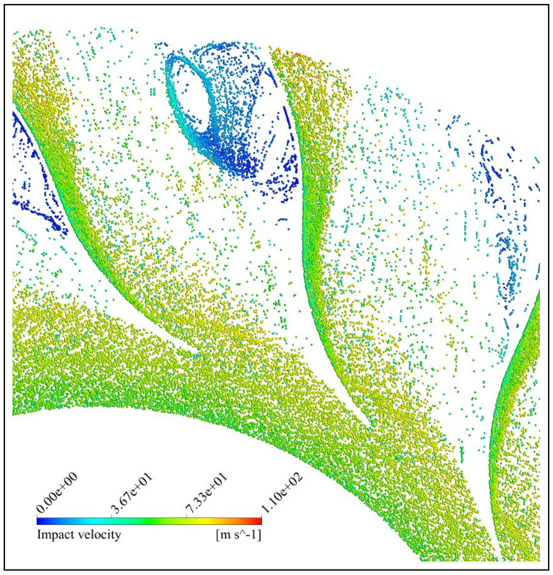

Figure 5.25: Impact on the impeller hub colored by impact velocity at ($\mathbf{Q_d}$).

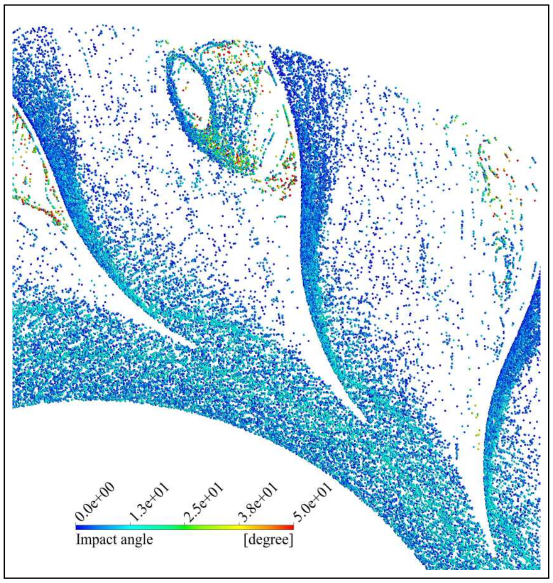

Figure 5.26: Impact on the impeller hub colored by impact angle at (Q_d).

According to the impact frequency chart depicted in Figure 5.18, more than 80% of the impacts on the hub originate from large-size particles, possessing significant inertia that propels them toward the hub. This increases the likelihood of these particles striking the hub before entering the blade passage. The concentration of large particles, as evident in Figure 5.24, is notable near the blade pressure side and the hub-blade junction during their traversal through the blade passage, resulting in a heightened frequency of impacts in this particular region. Figures 5.25 and Figure 5.26 indicate that large-size particles tend to impact the hub at angles around 15° and impact velocities ranging from 50 m/s to 70 m/s. The velocity increases as these particles move away from the hub-blade junction, reaching up to 110 m/s near the impeller outlet.

In contrast, the majority of impacts by small particles occur near the blade suction side within the blade passage. The trajectories of small particles near the blade pressure side, as shown in Figure 5.11, reveal that these impacts result from flow separations primarily occurring near the blade suction side. In this area, a flow vortex drives recirculating particles downward from the shroud to the hub, creating a dense region of impact characterized by low impact velocity and a moderate to high impact angle.

Figures 5.27 depict the erosion rate density contour on the impeller hub at the design flow rate. A comparison with the erosion pattern observed during the periodic inspection, as illustrated in Figure 5.22, reveals noticeable erosion concentrated around the blade mid-cord near the blade root, extending toward the trailing edge of the blade. However, no erosion is evident on the majority of the surface. The predicted erosion pattern presented in Figure 5.27 accurately anticipates the observed in-field erosion pattern with a high level of precision.

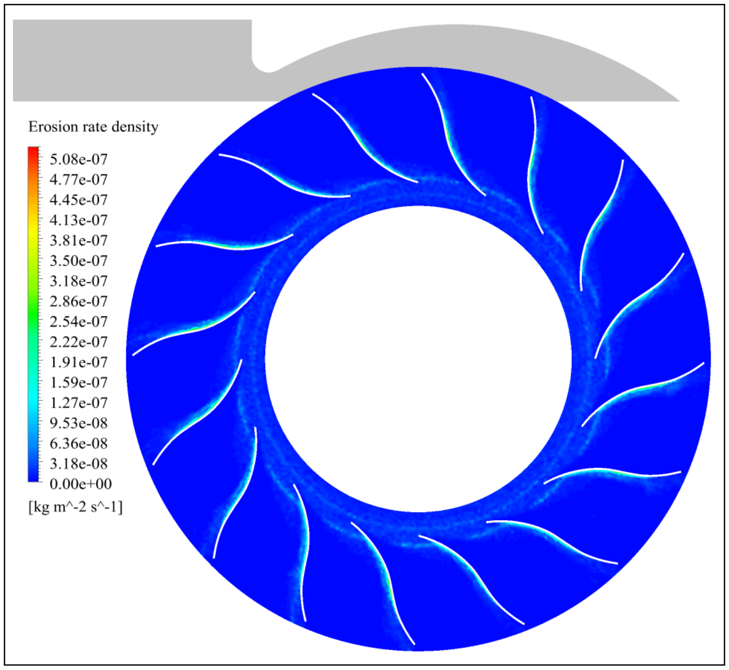

Figure 5.27: Impeller hub erosion rate density at (Q_d).

5.2.3 Effect of the operating condition on the erosion process

To explore the impact of operational conditions on the erosion process, Figures 5.28 and 5.29 present the erosion rate density contour for the pressure side of the blade. These figures depict the erosion rate density contour for a particle concentration of 30 mg/m^3 at flow rates corresponding to 0.74Q$_d$ and 1.78Q$_d$ respectively.

At a flow rate of 0.74Q$_d$ (40 m^3/s), as shown in Figure 5.28, the erosion pattern closely resembles that observed at the design flow rate, except for the blade's fore near the shroud, which remains unaffected by erosion. The erosion extends nearly to the mid-span of the blade, with the most substantial erosion occurring near the blade root. It's noteworthy that the maximum erosion at this flow rate is approximately ten times higher than the maximum erosion observed at the design flow rate. As the flow rate increases, illustrated in Figure 5.29, the area most prone to erosion becomes concentrated in the middle of the blade, covering almost the entire blade mid-span, with the maximum erosion occurring near the blade midspan at 50% of the blade's cord.

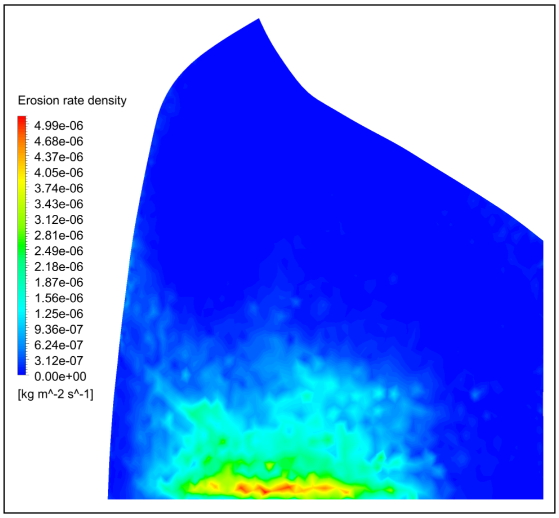

Figure 5.28: Erosion rate density on the Blade PS at 0.74Q$_d$.

As depicted in Figure 5.30 and Figure 5.31, the erosion rate density on the hub at flow rates of 0.74Q$_d$ and 1.78Q$_d$ follows a similar pattern, but the maximum erosion magnitude is one order of magnitude greater than that observed at the design flow rate. At a flow rate of 1.78Q$_d$, the eroded area along the blade root has expanded to encompass the blade passages upstream of the casing tongue. This expansion is attributed to non-uniformities in the flow field within each blade passage, as illustrated

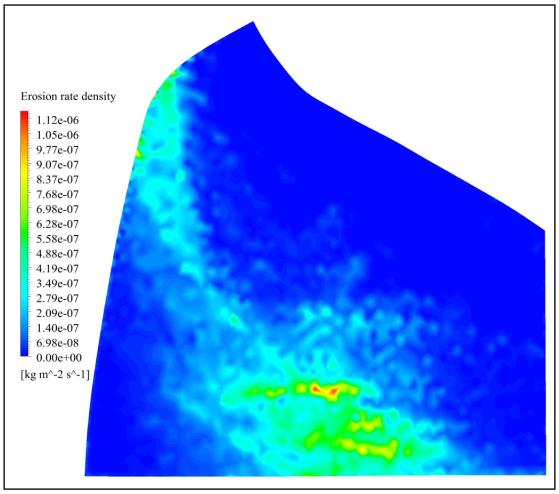

Figure 5.29: Erosion rate density on the Blade PS at 1.78Q_d.

in Figure 5.10.

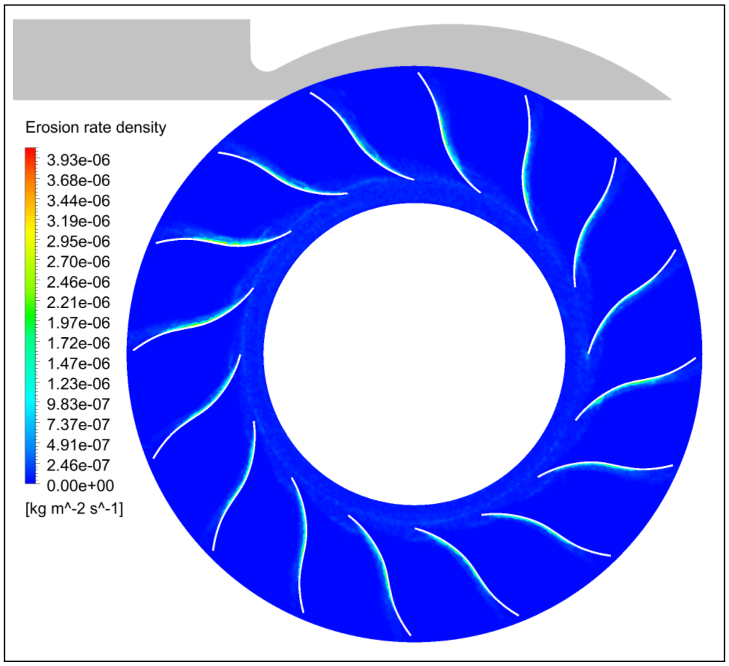

Figure 5.30: Impeller hub erosion rate density at (0.74Q_d).

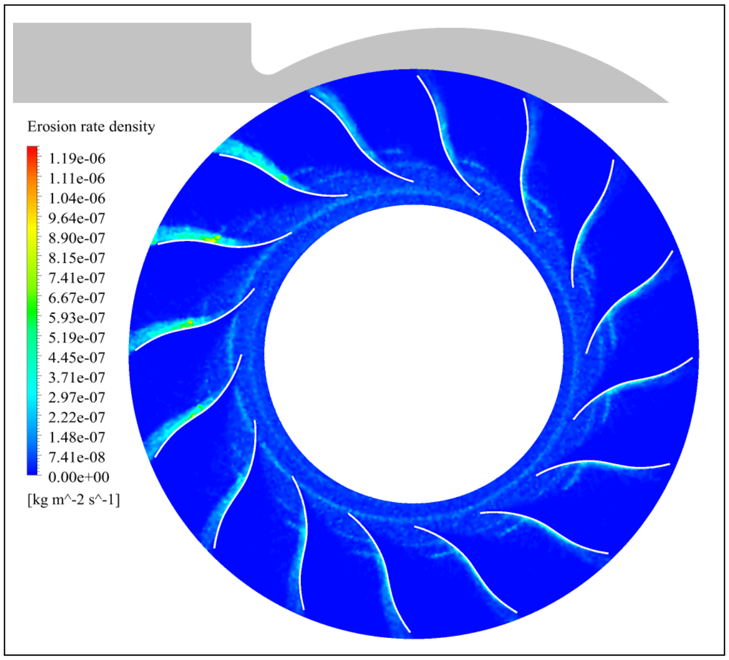

Figure 5.31: Impeller hub erosion rate density at (1.78Q_d).

5.2.4 Effect of the particle concentration on the erosion

The particle concentration in the airflow undergoes substantial variations due to the deterioration of the bag-filter tissue during operation. The escalation in particle concentration can lead to elevated erosion rates, necessitating an examination of the erosion intensity of impeller components under varying particle concentrations. The simulations incorporated solid particle concentrations ranging from 30 mg/m^3 to 150 mg/m^3. To ensure numerical results unaffected by the number of particles introduced at the inlet, 1.5×10^{-5} individual particles were released at the inlet. To evaluate the impact of particle concentration on erosion intensity, the total number of injected particles remained constant in each simulation. The mass flow rates of solid particles were adjusted for each simulation to align with the modeled particle concentration. This approach led to an increased number rate for each representative particle at varying concentration levels. Subsequently, the erosion rate was calculated using Equation **??**, resulting in a consistent erosion pattern while the intensity fluctuated across different particle concentration levels.

Figure 5.32 depicts the maximum erosion rate of impeller components, including the blade pressure side, suction side, impeller hub, and leading edge, for diverse particle concentrations at the design flow rate. The scatter plot reveals a positive correlation between particle concentration and maximum erosion rate, with the blade pressure side exhibiting a higher erosion rate than the other components. Furthermore, the relationship between erosion rate and particle concentration is linear, where the slopes are proportional to the maximum erosion rate of the targeted surface.

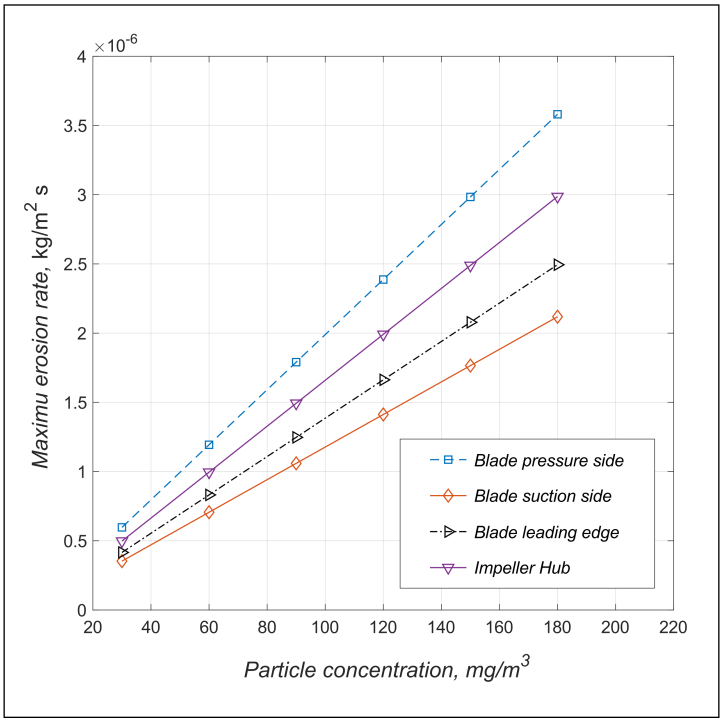

Figure 5.32: Erosion rate of monitoring surface under different particle load.

5.3 Geometrical Modification of the Reference Design

5.3.1 Different Blade Outlet Angles

The research involved conducting computational fluid dynamics (CFD) simulations to investigate the impact of altering the outlet angle of impeller blades on the performance and erosion patterns of the fan. for that purpose, the blade outlet angle was varied assuming four different outlet angles of 71°, 67°, 62° (the reference model), 58°, and 56°. All impellers in the study were equipped with 16 blades, and the blade inlet angles were kept constant across all configurations. Specifically, the study examined four operating regimes to plot the performance curve of the fan.

Figures 5.33, 5.34, and 5.35 demonstrate the correlation between adjustments in the blade outlet angle and the aerodynamic performance of the fan. The pattern is relatively straightforward: An increase in the outlet angle leads to a notable rise in both total pressure and torque across the entire operational range, while a decrease in the blade outlet angle produces the opposite effect. At lower flow rates (e.g., 40 m^3/s), altering the outlet angle has a relatively minor impact on the fan's overall efficiency. However, when the outlet angle is reduced to 56°, it enhances performance by approximately 1.12%, whereas larger outlet angles (e.g., 67°) result in a reduced performance of about 1.52%.At flow rates of 53.9 m^3/s and 72 m^3/s, increasing the outlet angle generates higher torque, which negatively affects the fan's performance. This is because, for the backward-S fan under investigation, the increase in total pressure rise does not sufficiently compensate for the rise in torque to enhance efficiency. Conversely, decreasing the blade outlet angle improves the fan's aerodynamic performance by up to 2.1%. At higher loads (e.g., 96 m^3/s), the reference design exhibits the highest total efficiency compared to various blade outlet angles. For higher loads, it appears that further increases in the blade outlet angle may have a detrimental effect while decreasing the blade outlet angle enhances the fan's performance.

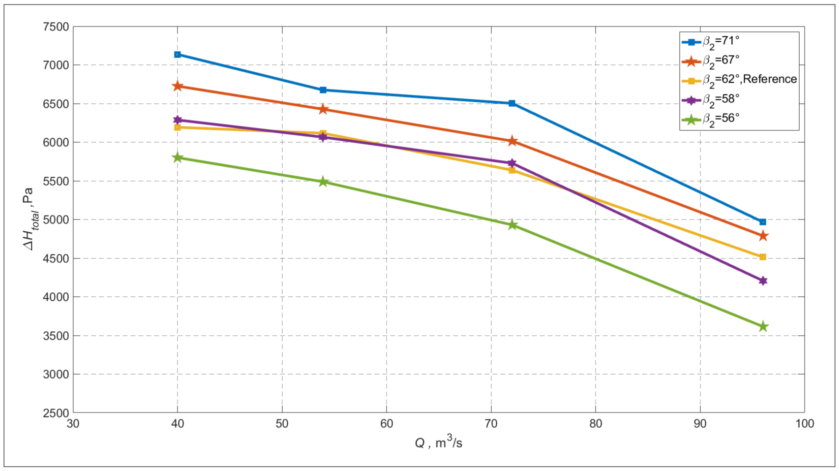

Figure 5.33: The effect of changing the outlet angle of the impeller blades on total pressure rise of the fan.

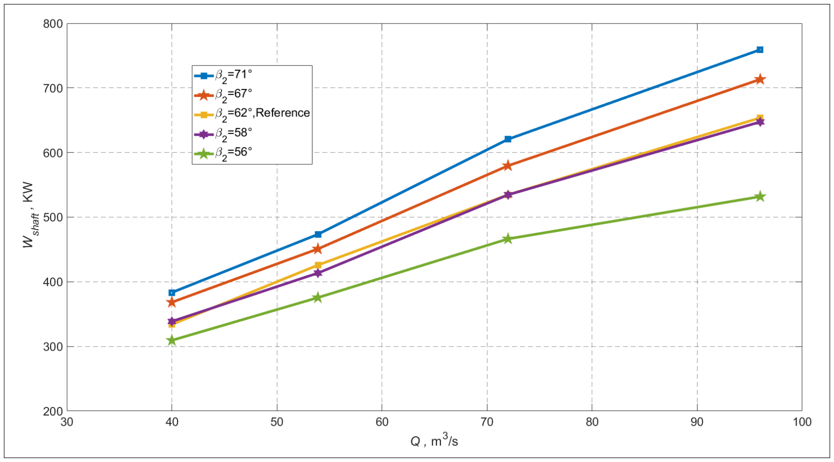

Figure 5.34: The effect of changing the outlet angle of the impeller blades on fan shaft power.

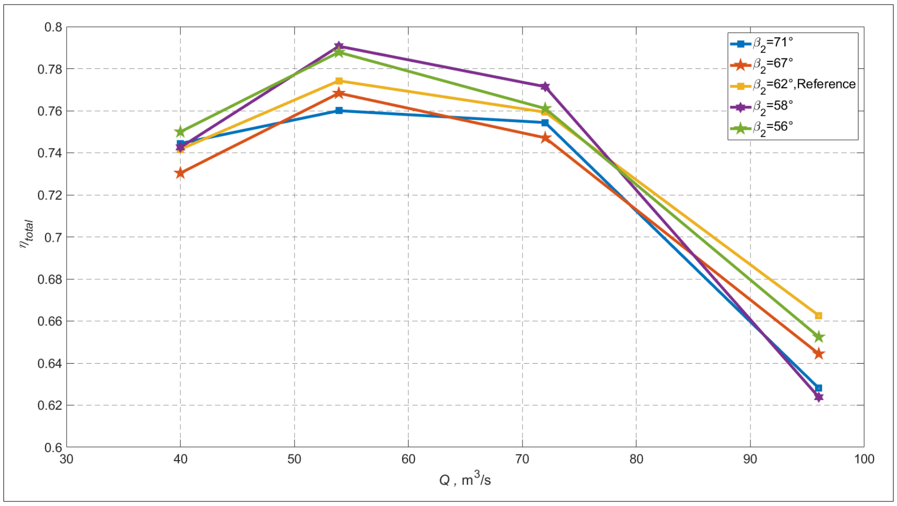

Figure 5.35: The effect of changing the outlet angle of the impeller blades on the total efficiency of the fan.

Furthermore, as depicted in Figure 5.36, 5.37, and 5.38, showcasing the relative velocity magnitude at the mid-span section of the corresponding blade under flow rates of 40m^3/s, 53.9 m^3/s, and 96m^3/s, it becomes evident that the extent of flow separations occurring in the impeller channels near the blade's suction side, which are inescapable, becomes more confined when the blade outlet angle is reduced. This development holds advantages from both an aerodynamic perspective and could be a contributing factor to the enhanced performance observed in impellers with narrower outlet angles.

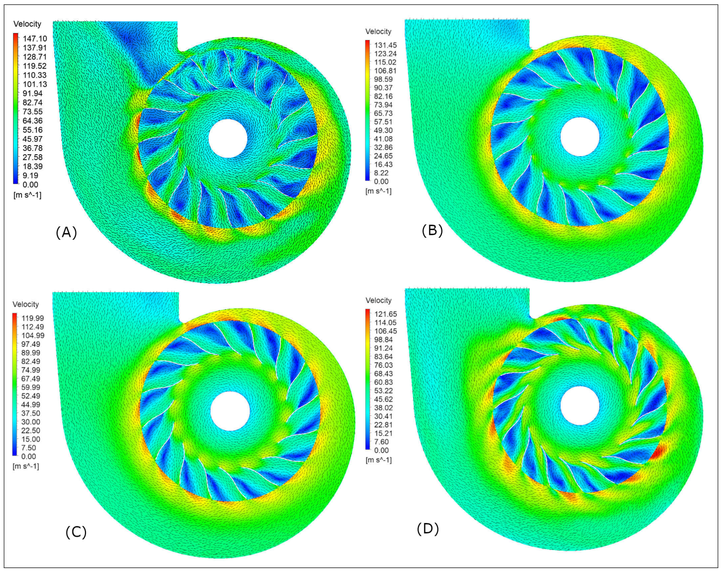

Figure 5.36: Relative velocity magnitude at the mid-span section of the blade with different outlet angles at (40 m^3/s),A)= 71°,B)= 67°,C)= 58°,D)= 56°.

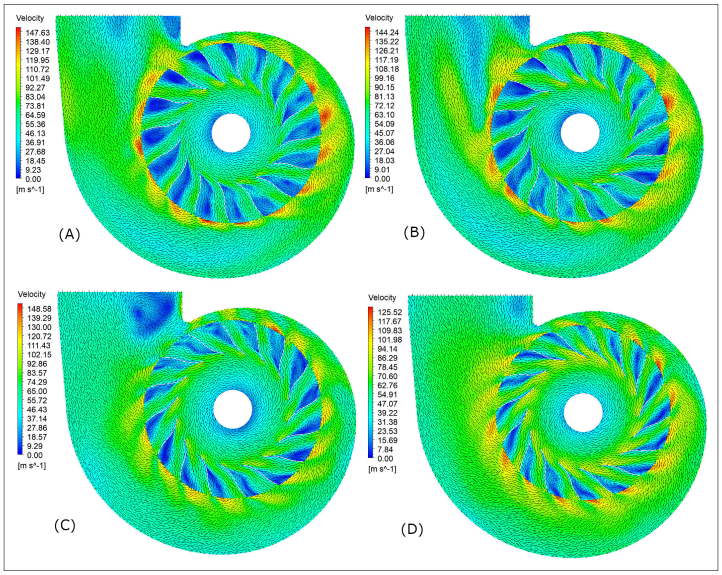

Figure 5.37: Relative velocity magnitude at the mid-span section of the blade with different outlet angles at (53.9 m^3/s),A)= 71°,B)= 67°,C)= 58°,D)= 56°.

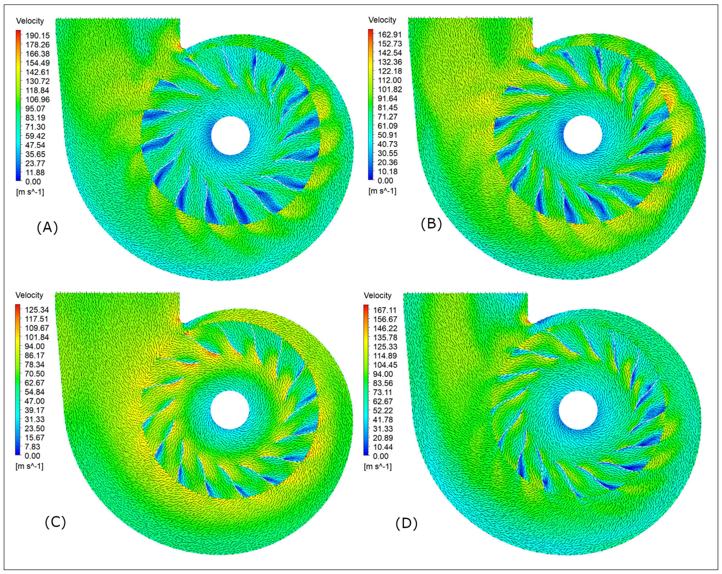

Figure 5.38: Relative velocity magnitude with different outlet angles at (96 m^3/s).

5.3.1.1 Erosion patterns on the impeller components

Figure 5.39 illustrates the erosion rate density on the blade pressure side across various blade outlet angles: 71°, 67°, 58°, and 56°. The general observation reveals that the erosion rate density peaks at the mid-cord of the blade root for all angles. Higher outlet angles, specifically 71° and 67°, display erosion spreading towards the upper portion of the leading edge. This particular region faces more direct particle impact due to the increased flow deflection at higher angles. Notably, the blade outlet angle significantly influences erosion rates and patterns, with the erosion rate density being highest for the blade featuring the largest outlet angle (71°) and lowest for the blade with the smallest outlet angle (56°). Moreover, larger outlet angles (71°, 67°) result in wider erosion zones covering nearly two-thirds of the blade chord and extending toward the leading edge. Conversely, smaller outlet angles (58°, 56°) lead to concentrated erosion around the mid-cord, with minimal impact on the leading edge.

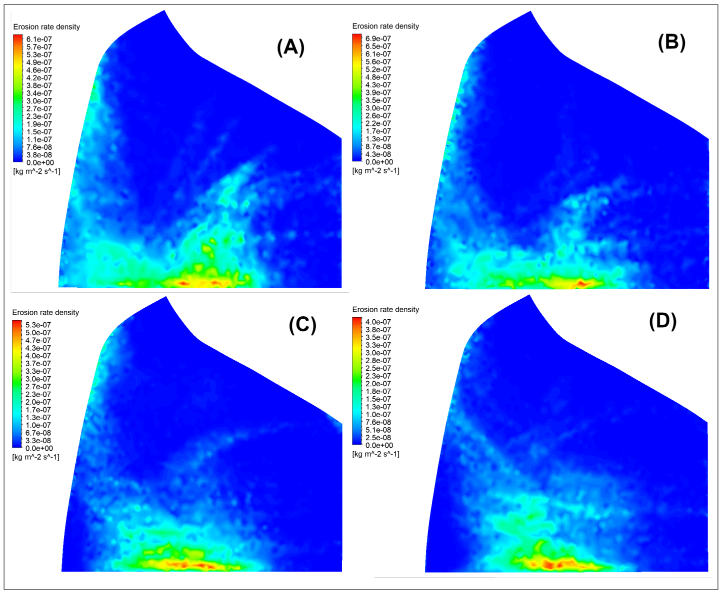

Figure 5.39: Erosion pattern on the blade PS with different outlet angle at 53.9 m^3/s, A)=71°,B)=67°,C)=58°,D)=56°.

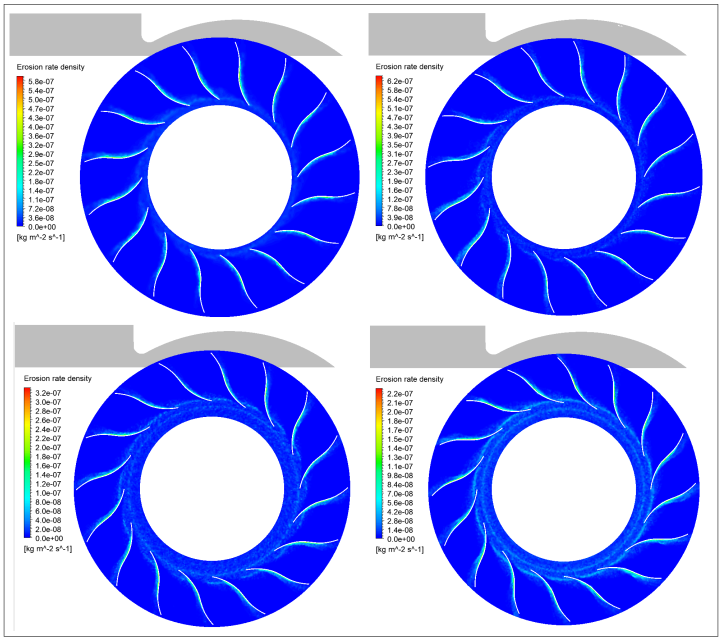

Figure 5.40: Erosion rate density on the impeller hub with different outlet angle at 53.9 m^3/s; A)=71°,B)=67°,C)=58°,D)=56°.

5.3.1.2 Wall thickness reduction per year on the blade pressure side with different outlet angle

In our investigation, we conducted an additional analysis to examine the impact of changes in the blade outlet angle on erosion on the pressure side of the blade. Specifically, we plotted the thickness of eroded material as it varies across the normalized length of the blade's camber. This normalized length scale spans from zero, representing the leading edge of the blade, to one, which corresponds to the trailing edge. To evaluate erosion, we measured the thickness of eroded material at a particle load of 30 mg/m^3 at six distinct sections marked as S1, S2, S3, S4, S5, and S6. These sections are indicated in Figure 5.41 for reference. This additional analysis is a crucial step in comprehending how the blade's outlet angle influences erosion on the pressure side. By charting the eroded material thickness across the normalized blade camber length, we can pinpoint the areas of the blade that are most susceptible to erosion. This data can then inform the design of more erosion-resistant blades. The utilization of six specific sections for erosion assessment is a good approach, providing a detailed view of the erosion pattern along the blade. By comparing erosion profiles for various blade outlet angles, we can identify the specific effects of this parameter on erosion.

The mass of material denoted as **m**, which is removed from surface **A**, can be mathematically characterized by the product of the erosion rate density over a defined operational duration and the surface area of the element cell, as illustrated by the following equation:

$$m = ER . A \tag{5.2}$$

Considering the erosion rate density denoted as ER following a year of operation, the mass of eroded material can alternatively be expressed as a function of the wall surface density and the volume of eroded material:

$$m = \rho_s \, V_{er} = \rho_s \, A \, h \tag{5.3}$$

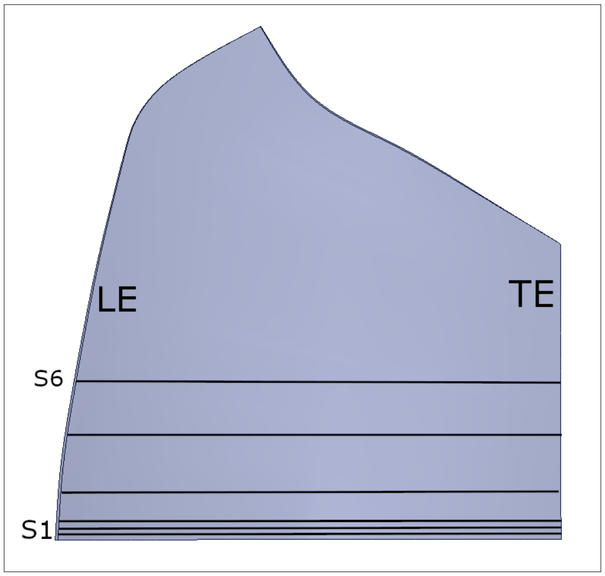

Figure 5.41: Blade sections used for measuring the eroded thickness on the blade pressure side.

The thickness of the eroded volume represented as **h**, can be readily calculated by comparing the two aforementioned equations

$$h = \frac{ER}{\rho_s} \tag{5.4}$$

The eroded thickness data for sections S1, S2, S3, and S4 depicted in Figure 5.42 through Figure 5.47 clearly demonstrate a consistent trend: eroded thickness decreases as the blade's outlet angle decreases. This pattern is remarkably similar across all these sections, showcasing the robustness of this relationship. To delve deeper, it's important to note that at blade outlet angles of 62°, 58°, and 56° degrees, the leading and trailing edges of the blade pressure side remain unaffected by erosion. However, a slight reduction in thickness, averaging about 0.3 mm, is observed when the blade outlet angles are increased to 67 and 71 degrees. Moving further along the blade's surface, it's evident that the eroded thickness gradually increases as we move from the leading edge toward the camber's center position on the blade's pressure side. The highest eroded thickness values are concentrated in this region. Subsequently, moving towards the trailing edge, the eroded thickness begins to decrease again.

When we compare the different sections, specifically S1 through S6, the data reveals a consistent reduction in eroded thickness. However, it's noteworthy that at sections S1 and S2, the maximum eroded thickness is approximately 1.8 mm when the blade outlet angles are set at 71° and 67°. The changes in erosion rates are more pronounced in section S1 compared to sections S2, S3, and S4. The maximum erosion rates decline by approximately 45% as the blade outlet angle decreases from 71° to 56°. This substantial drop in erosion rates underscores the potential of lower blade outlet angles to significantly mitigate erosion. It's also essential to point out that in section S4, with blade outlet angles of 58° and 56°, the distribution of eroded thickness varies slightly from the other models. In these cases, the peak eroded thickness extends about one unit to the left and right from the blade's center. While this alteration is not drastic, it introduces some variability in the erosion pattern.

On average, the maximum eroded thickness difference between the reference model (62° blade outlet angle) and the model with the smallest blade outlet angle (56°) is about 0.4 mm. This may seem like a minor distinction, but it can have a noteworthy impact on the fan's overall erosion resistance, especially under operating conditions characterized by high particle concentration and heavy loads. This data underscores the importance of optimizing the blade outlet angle to enhance the fan's durability and performance in challenging conditions. In contrast to the other sections, specifically, sections S5 and S6 (located at the blade's midspan), the distribution of eroded thickness exhibits dissimilar patterns for varying blade outlet angles. Notably, when the blade outlet angles are set at 62°, 58°, and 56°, the maximum reduction in thickness shifts by one unit to the left and right in section S5. However, when the outlet angle is adjusted to 67° and 71°, the maximum thickness reduction remains centered at the blade's camber.

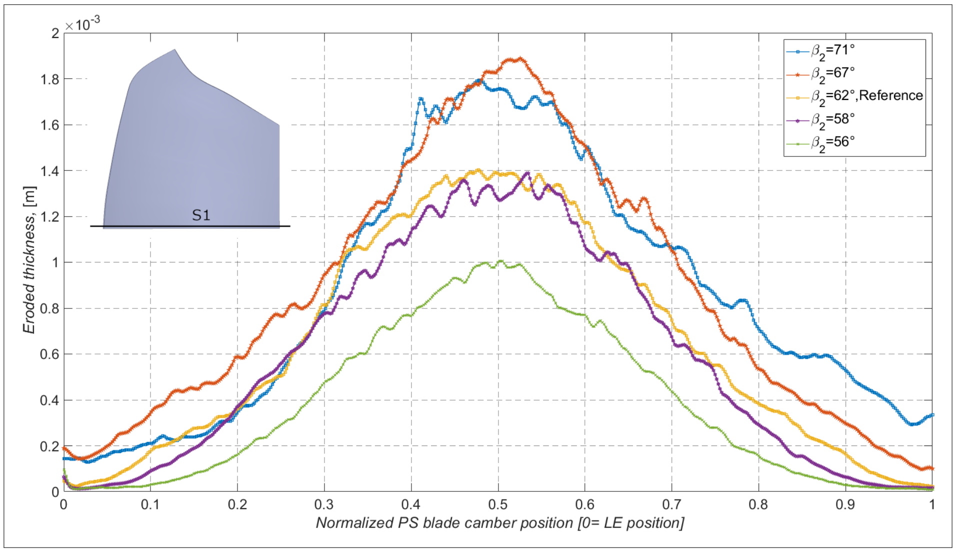

Figure 5.42: Eroded Thickness on Blade PS along S1 After 8760 Hours at 53.9 m^3/s and 30, mg/m^3.

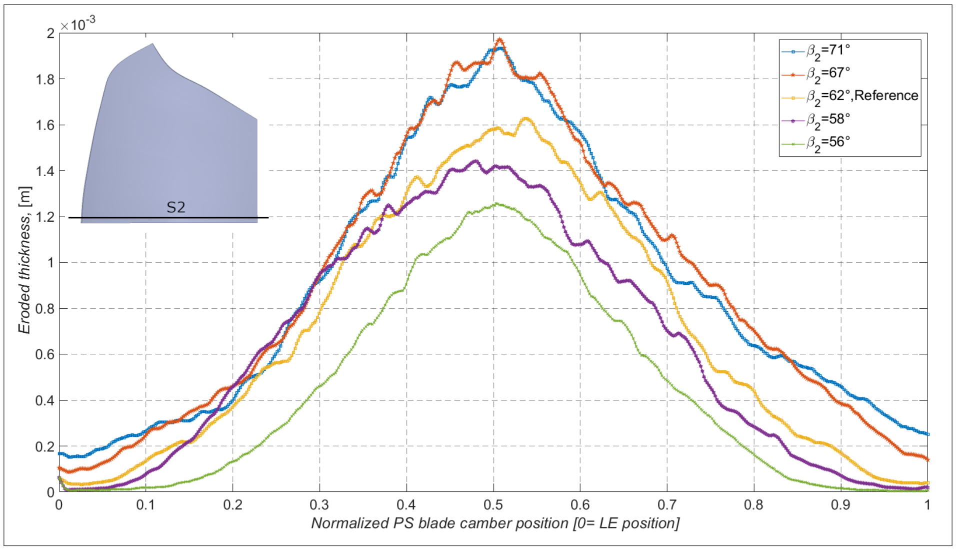

Figure 5.43: Eroded Thickness on Blade PS along S2 After 8760 Hours at 53.9 m^3/s and 30, mg/m^3.

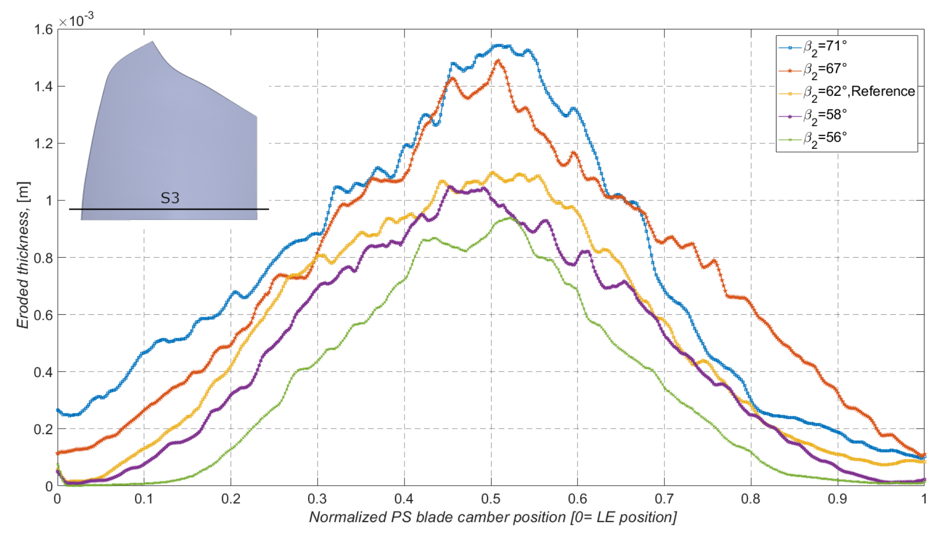

Figure 5.44: Eroded Thickness on Blade PS along S3 After 8760 Hours at 53.9 m^3/s and 30, mg/m^3.

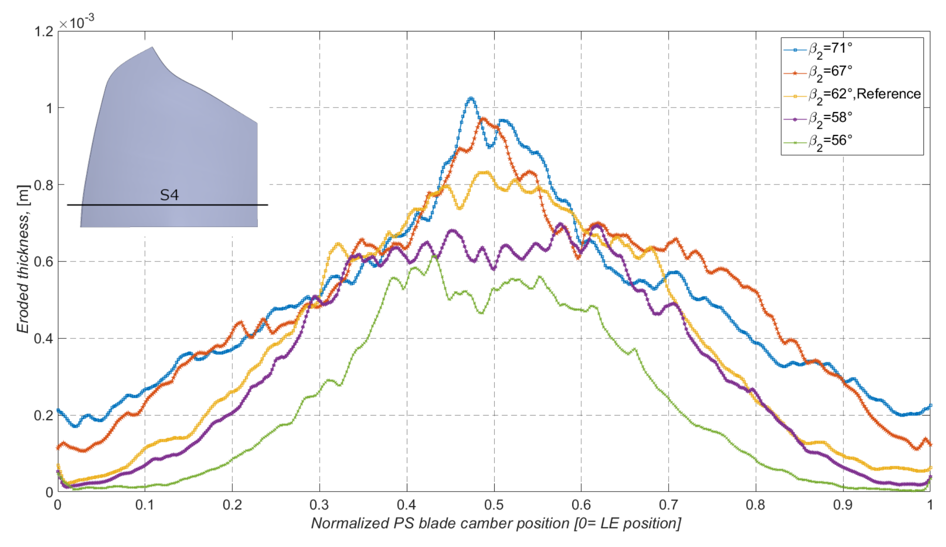

Figure 5.45: Eroded Thickness on Blade PS along S4 After 8760 Hours at 53.9 m^3/s and 30, mg/m^3.

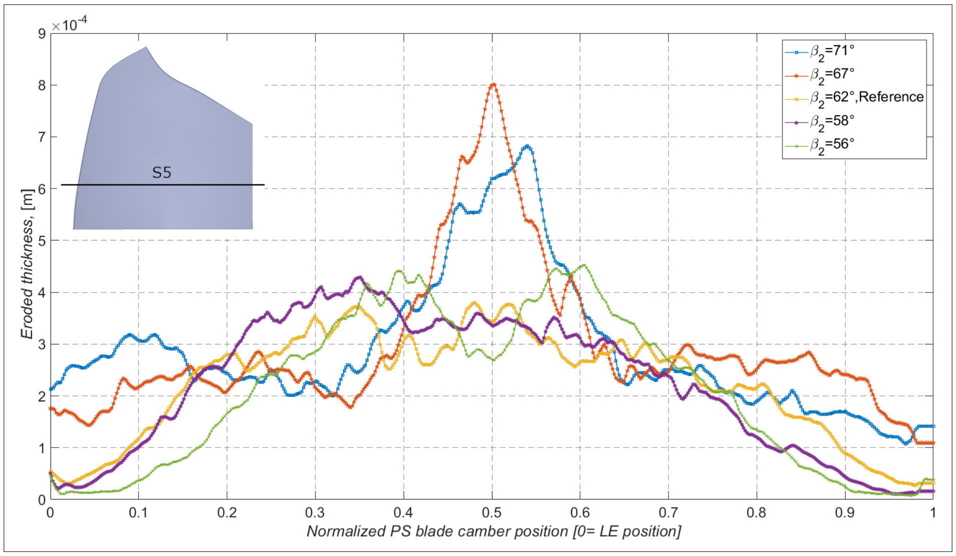

Figure 5.46: Eroded Thickness on Blade PS along S5 After 8760 Hours at 53.9 m^3/s and 30, mg/m^3.

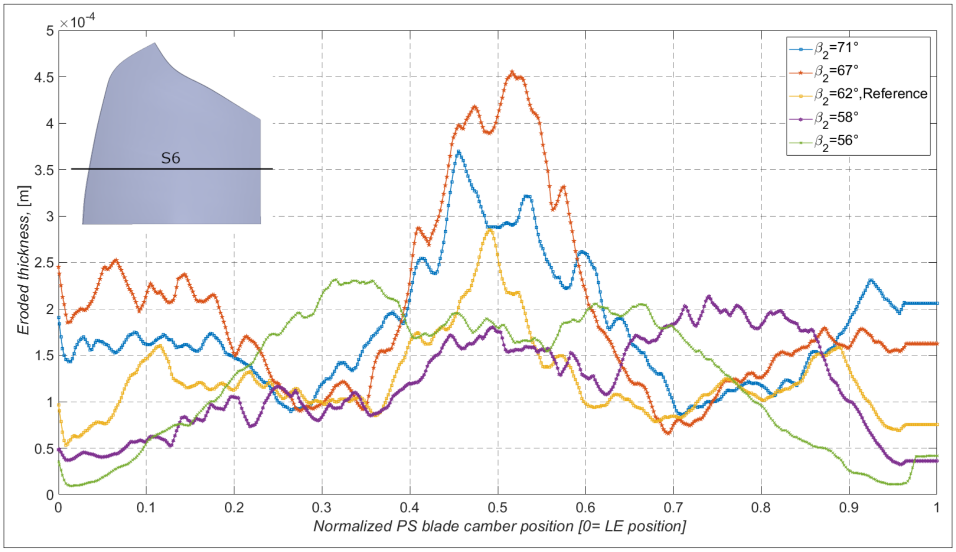

Figure 5.47: Eroded Thickness on Blade PS along S6 After 8760 Hours at 53.9 m^3/s and 30, mg/m^3.

The varying erosion patterns observed at different blade outlet angles is strongly attributed to the distinct flow conditions. Consequently, at different blade outlet angles, the characteristics of particle impact are significantly influenced by the fluid dynamics within the impeller region, particularly within the blade-to-blade passage. The data provided in Fig.5.48 offers valuable insights into the impact frequencies of particles on the blade pressure side at varying blade outlet angles. The dataset encompasses particle impact frequencies at five distinct blade outlet angles: 71°, 67°, 62°(Reference), 58°, and 56°. Each blade outlet angle is associated with two primary segments in the stacked bar chart. These segments delineate particles based on their size class previously discussed, SSP with particle diameters $d_p < 30\,\mu m$ and large-size particles LSP with diameters ranging from $30\,\mu m$ to $200\,\mu m$.

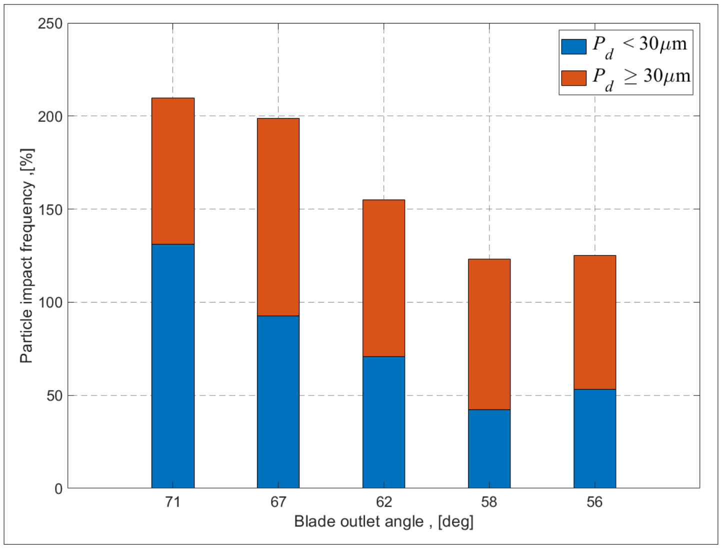

Figure 5.48: Particle impact frequency distribution on the blade PS at different Blade outlet angle.

The chart conveys several noteworthy observations, with a critical focus on the total particle impact as it varies with blade outlet angles. In the dataset, the total particle impact reveals an essential trend: it decreases as the blade outlet angle decreases. This observation highlights the profound influence of blade geometry on the overall particle impact, suggesting that larger blade outlet angles may lead to higher total particle impact. One of the most evident trends pertains to the effect of blade outlet angles on particle behavior. As the blade outlet angle decreases from 71° to 56°, the behavior of particle impact frequencies becomes markedly distinct. A compelling insight emerges when comparing the segments within each bar: the impact frequency of smaller-sized particles (SSP) tends to decrease as the blade outlet angle decreases, while conversely, the impact frequency of larger particles shows a tendency to increase relative to smaller particles when blade outlet angles decrease. Overall, this chart provides valuable insights into how variations in blade outlet angles can impact the distribution of particle impact frequencies, particularly for different particle size classes. These insights can inform engineering decisions related to blade design and particle impact control.

To gain a deeper understanding of how changes in the blade outlet angle affect impact characteristics on the blade's pressure side, Figures 5.49 to 5.52 depict the velocity and angle at which impacts occur on the blade's pressure side for various blade outlet angles.

For large particles, the impact velocity distribution follows a consistent pattern across different blade outlet angles. Large particles predominantly impact the blade within the velocity ranges of 60-70 m/s and 70-80 m/s, with minimal impact probability observed at both lower and higher velocity ranges. The alteration of the blade outlet angle appears to have negligible effects on the impact velocity distribution, except for the case of the lowest outlet angle, 56°. Conversely, small particles exhibit a preference for impacting the blade at moderate velocities. They display a significant probability of impact within the velocity range of 10-20 m/s for larger blade outlet angles (71° and 67°), followed by a gradual decrease in probability as velocity increases further. However, for smaller outlet angles (58° and 56°), the impact velocity is centered around the 30-50 m/s range, and reducing the blade outlet angle seems to decrease the impact velocity of small particles. Notably, for the lowest outlet angle of 56°, small-size particles exhibit a peak impact velocity within the 0-10 m/s range.

When examining the impact angles, distinct patterns become evident, particularly when considering different blade outlet angles, notably 71° and 67°. These patterns showcase unique behaviors exhibited by small and large particles:

For Higher Blade Outlet Angles (71° and 67°): Small particles tend to favor striking the blade within a relatively narrow range of impact angles, predominantly falling within the 0° to 25° range. The highest probability is concentrated in the 0-5° range, signifying a strong preference for shallow impact angles. In contrast, large particles display a wider spread of impact angles, covering the range from 0° to 45°. The peak probability is observed in the 20-25° range, with notable probabilities in the 25-30° and 30-35° ranges, which encompass the angle (30°) associated with maximum erosion. Transitioning to a 67° blade outlet angle, small particles maintain their inclination for shallow impact angles but exhibit an expanded distribution within the 5-20° range compared to the 71° configuration. For large particles, the probability distribution of impact angles becomes less prominent, particularly in the 20-25°, 25-30°, and 30-35° ranges. Although a preference for impact angles in the 20-25° range remains, it is not as pronounced as observed at the 71° angle setting.

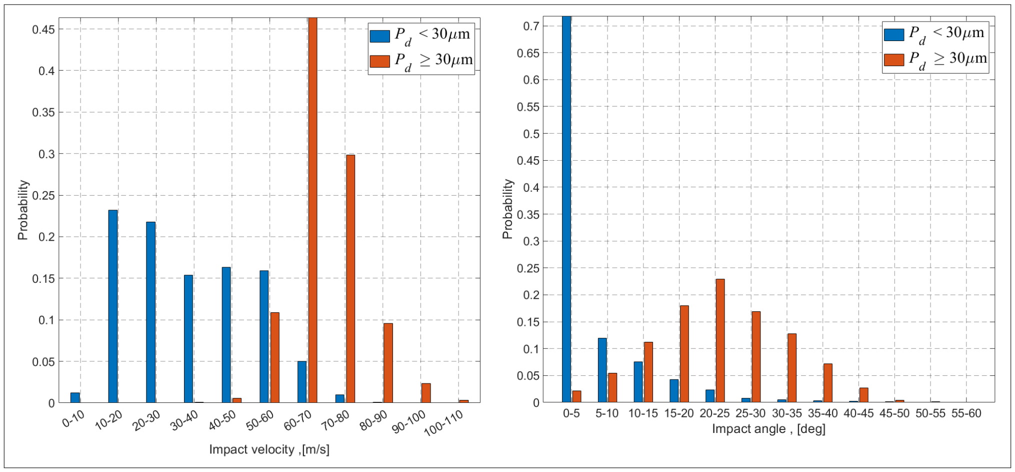

Figure 5.49: Probability of Impact Velocities and Angles for different Particle Size Classes on Blade PS at 71°.

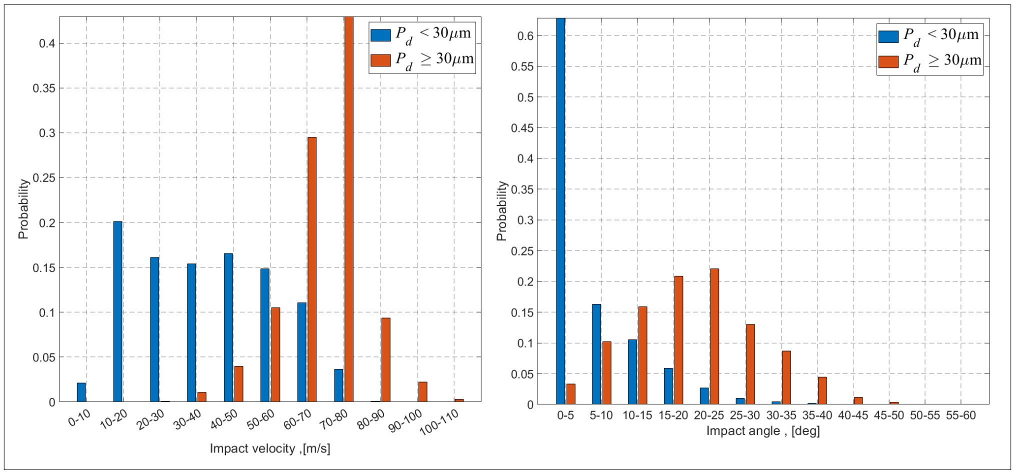

Figure 5.50: Probability of Impact Velocities and Angles for different Particle Size Classes on Blade PS at 67°.

With Further Reduction in Blade Outlet Angle: As the blade outlet angle is further decreased, a few noteworthy trends emerge: Small particles demonstrate a more uniform distribution of impact angles spanning the 5-25° range. Decreasing the blade outlet angle to 56° results in small-sized particles exhibiting wider impact angle distributions, extending up to 75° and even reaching 90° when compared to higher outlet angles. At smaller outlet angles like 56°, small particles continue to exhibit a preference for shallow impact angles, although the peak probability is less prominent than at higher angles. Similarly, for large particles at smaller outlet angles, the peak probability shifts to the 15-20° range, indicating a preference for slightly steeper impact angles. Further reduction in the blade outlet angle to 56° leads to a shift toward even smaller angles, particularly within the 10-15° range.

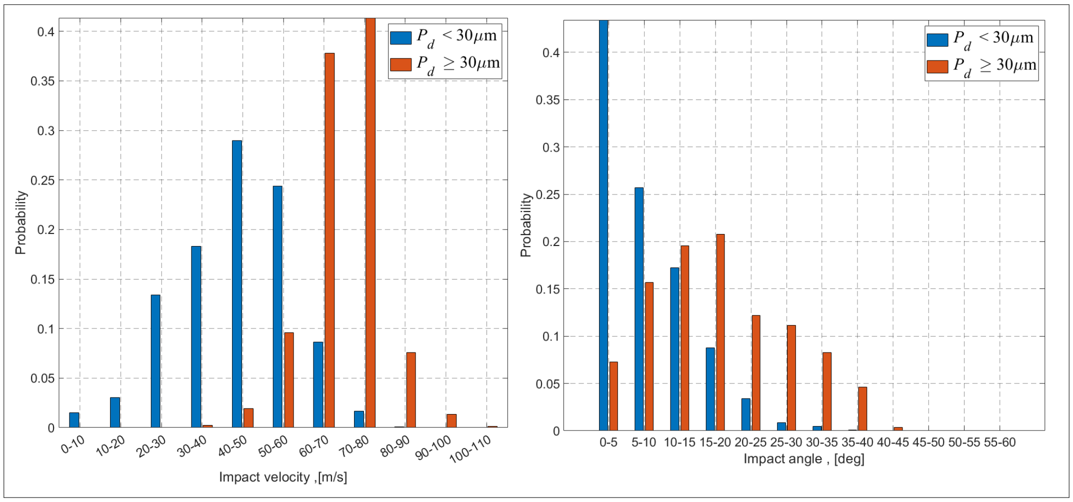

Figure 5.51: Probability of Impact Velocities and Angles for different Particle Size Classes on Blade PS at 58°.

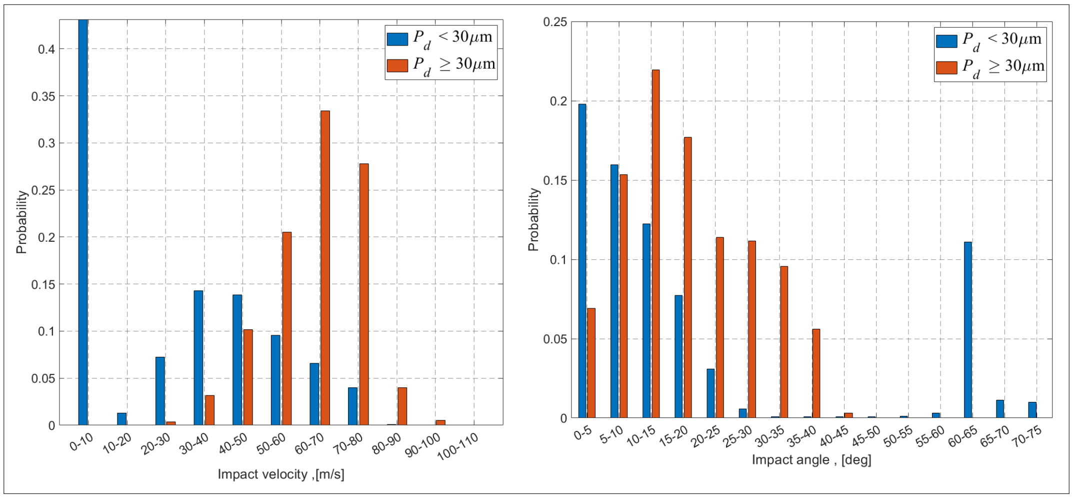

Figure 5.52: Probability of Impact Velocities and Angles for different Particle Size Classes on Blade PS at 56°.

This dataset offers valuable insights into the influence of blade outlet angles on erosion patterns. It becomes evident that blade outlet angles play a pivotal role in shaping the overall particle impact dynamics. Larger blade outlet angles, specifically

71° and 67°, are associated with higher total particle impact, while a prominent trend emerges: as blade outlet angles decrease, the total particle impact decreases as well. The examination of particle size classes uncovers interesting trends. Smaller particles (SSP) tend to experience reduced impact frequencies as blade outlet angles decrease, while the opposite holds true for larger particles (LSP), with their impact frequencies increasing as blade outlet angles decrease.

Regarding impact velocities, it is noteworthy that large particles consistently strike the blade within the velocity ranges of 60-70 m/s and 70-80 m/s across varying blade outlet angles. The impact velocity distribution for large particles is moderately influenced by blade outlet angle alterations, with the exception of the lowest angle, 56°. In contrast, small particles exhibit a preference for impacting the blade at moderate velocities.

Lastly, Small particles consistently favor shallow impact angles, primarily falling within the 0° to 25° range. As blade outlet angles decrease, small particles show more even impact angle distributions in the 0-20° range. On the contrary, large particles present a broader range of impact angles, spanning from 0° to 45°, with the peak probability transitioning from the 20-25° range to the 10-15° range as the blade outlet angle decreases. Impact angles in the 20-30° range are particularly relevant, as this range corresponds to the angle associated with maximum erosion rates, (30°).

the analysis reveals that while blade outlet angle variations have a significant impact on impact angles and particle impact frequency, the velocity impact distribution remains relatively consistent across different blade outlet angles. This highlights that the primary driver of higher erosion rates at larger blade outlet angles is the combination of particle impact angle and impact frequency. These findings emphasize the critical importance of considering impact angles in erosion control strategies and blade design for backward-S centrifugal fans.

5.3.1.3 Effect of the flow regime

Figure 5.53 illustrates the erosion thickness along various sections of the blade pressure side at an airflow rate of 96 m^3/s and a particle load of 30 mg/m^3. This investigation aims to understand how the high-load operating conditions impact erosion severity.

The overall observation reveals that the maximum erosion thickness occurs at the center of the blade's camber length. In the case of larger outlet blade angles such as 71° and 67°, the trend is straightforward: erosion thickness increases from section S6, where erosion rates are relatively uniform along the section from the leading to the trailing edge, to section S1, where the erosion thickness is the highest, reaching up to 2.8 mm. However, for smaller blade outlet angles like 58° and 56°, the erosion thickness distribution differs from that of larger outlet angles. The blade's mid-span exhibits higher erosion rates, and decreasing the blade outlet angle further shifts the maximum erosion rates towards the blade's mid-span, in contrast to larger outlet blade angles where the maximum eroded thickness is located near the blade root.

It is crucial to emphasize that the impact of the high-load operational conditions is notably substantial. the values indicated in Fig.5.53 correspond to a particle load of 30 mg/m^3. However for higher particle loads the erosion thickness may experience a sharp and noteworthy increase, this increase is linearly dependent on the partilce concentration as discussed in section.5.2.4. This information implies that reducing the blade outlet angle can potentially yield favorable outcomes in terms of erosion patterns and severity, particularly under conditions involving higher particle loads and operational regimes. This tendency may hold significant relevance for engineering purposes, as it presents a viable approach to address erosion-related challenges in high-load environments.

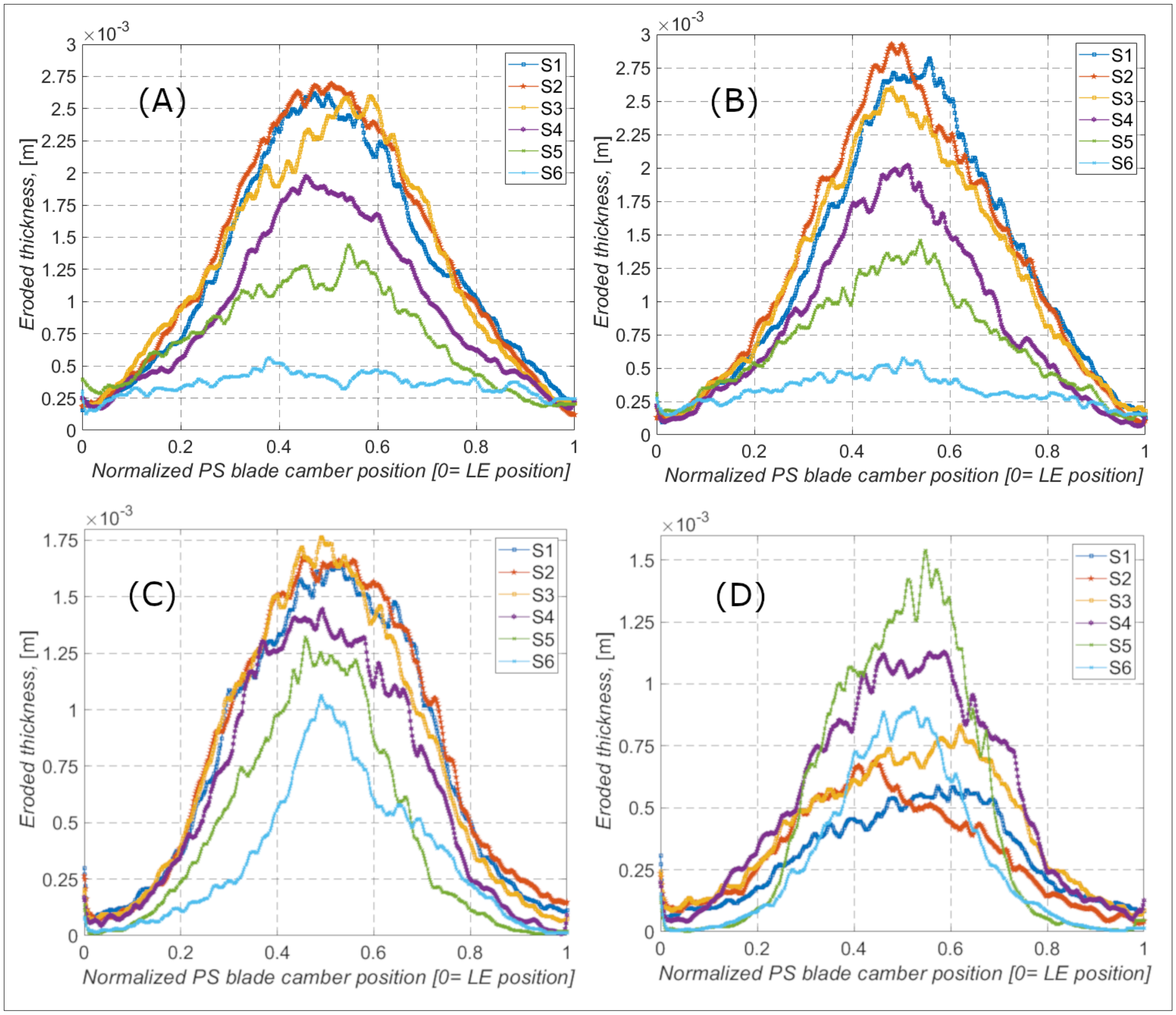

Figure 5.53: Eroded Thickness on Blade PS along different sections After 8760 Hours at 96 m^3/s and 30, mg/m^3, A)=71°,B)=67°,C)=58°,D)=56°.

5.3.2 Different Number of Blades

The effect of changing the number of impeller blades on the performance characteristics of the fan and the erosion pattern is also investigated. The numerical investigations consider impellers with 12, 14,18, and 20 blades. The inlet and outlet blade angles are identical in all of the impeller models. The performance curves and the erosion prediction are obtained from URANS simulation.

Figures 5.54-5.56 show the effect of this modification on the aerodynamic performance of the fan. It appears that the effect of changing the impeller blade number has a small effect on the total pressure rise for low flow rates, however, for higher flow rates the total pressure rise decreases especially for decreased blade numbers e.g. (12 and 14). as for the power shaft, The trend is quite straightforward: increasing the number of blades leads to higher torque, particularly in higher range flow rates. In the low to mid-range flow rates changing the impeller blade count does not considerably affect the total efficiency of the fan, whereas the ensuing effects in the higher range are significant where altering the impeller blade count shows a decreased performance.

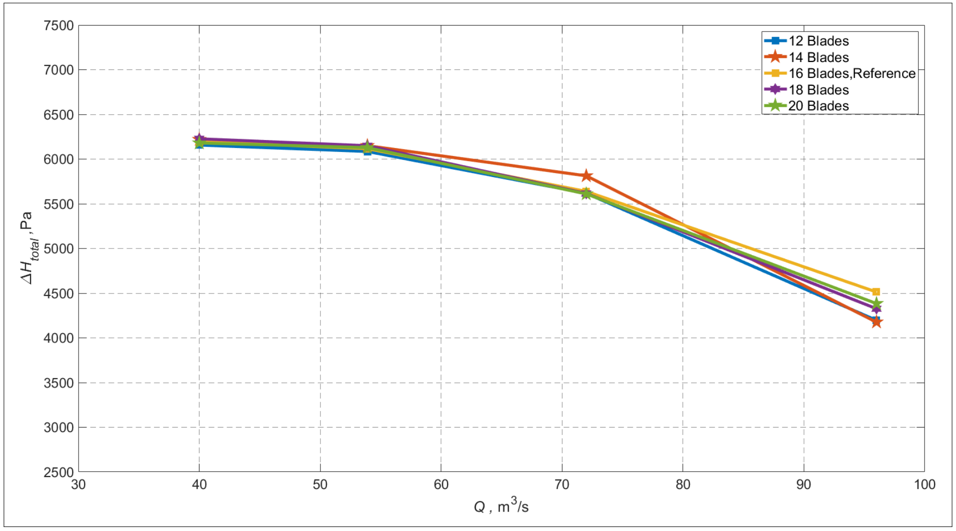

Figure 5.54: The effect of changing the number of impeller blades on total pressure rise of the fan.

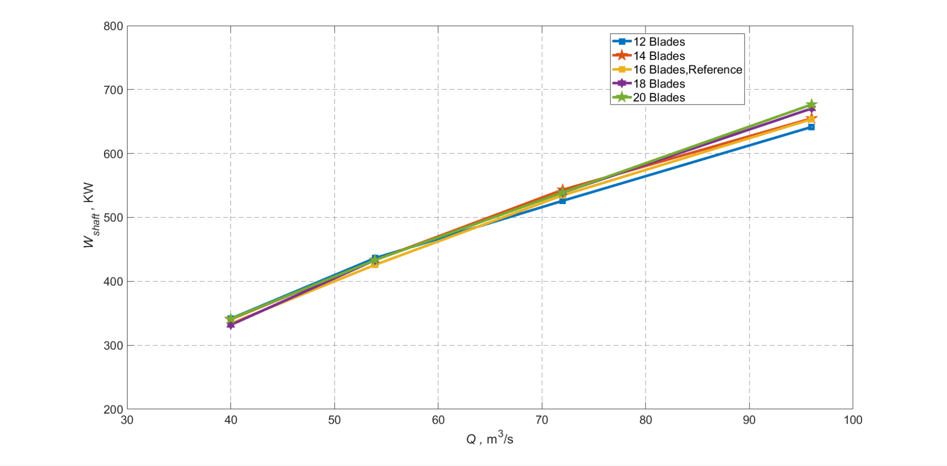

Figure 5.55: The effect of changing the number of impeller blades on the shaft power.

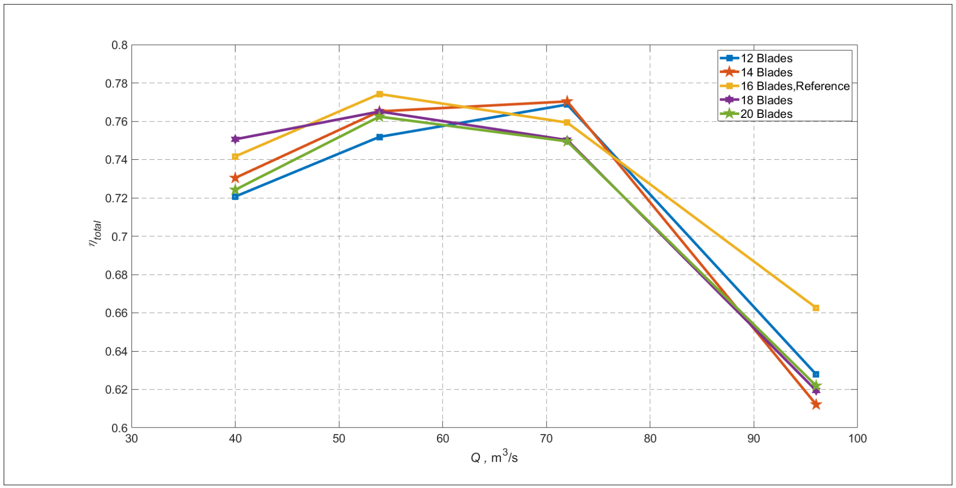

Figure 5.56: The effect of changing the number of impeller blades on the total efficiency.

As depicted in Figure.5.57, The size of the flow separation in the blade passage on the blade suction side becomes smaller as the number of blades increases. notably, the flow separation on the blade suction side begins after one-third of the blade near the leading edge and extends toward the blade's trailing edge.

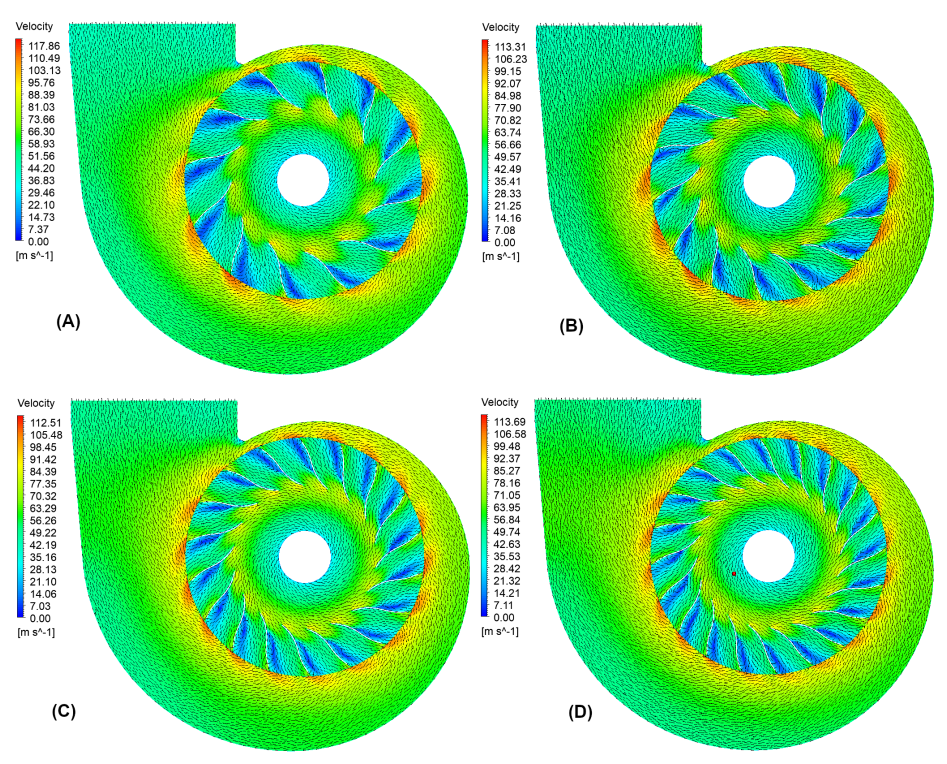

Figure 5.57: Relative velocity contour with different number of blades at 53.9 m^3/s , ,A)=12 blades,B)=14 blades,C)=18 blades, D)=20 blades.

According to Figure.5.58 and Figure.5.59, which depict the erosion rate density on the blade pressure side with varying numbers of blades, the effects of changing the number of blades on the erosion pattern and magnitude is not as significant as changing the blade outlet angle. yet, the area that face erosion on the blade pressure side extend to cover nearly the blade outlet mid-span for reduced blade count e.g (12 and 14) in contrast to impeller design featuring increased blade count where erosion is

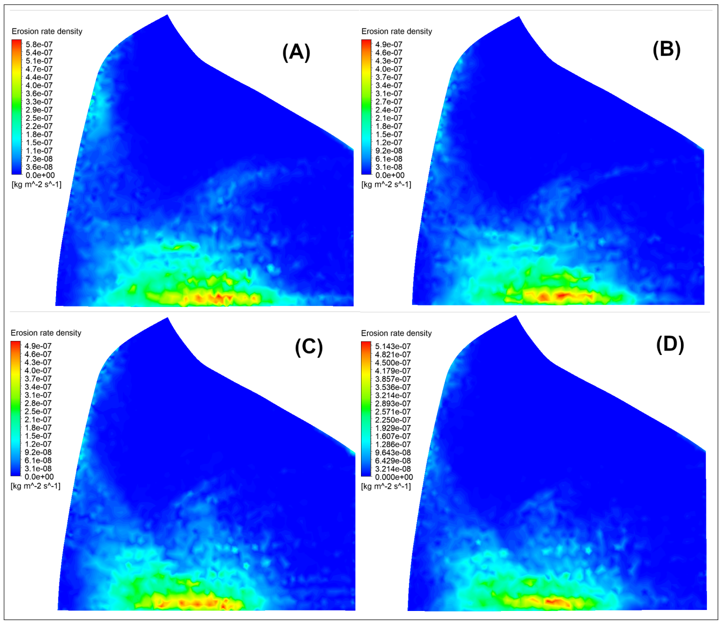

Figure 5.58: Erosion rate density on the blade PS at 53.9 m^3/s; A)=12 blades,B)=14 blades,C)=18 blades, D)=20 blades .

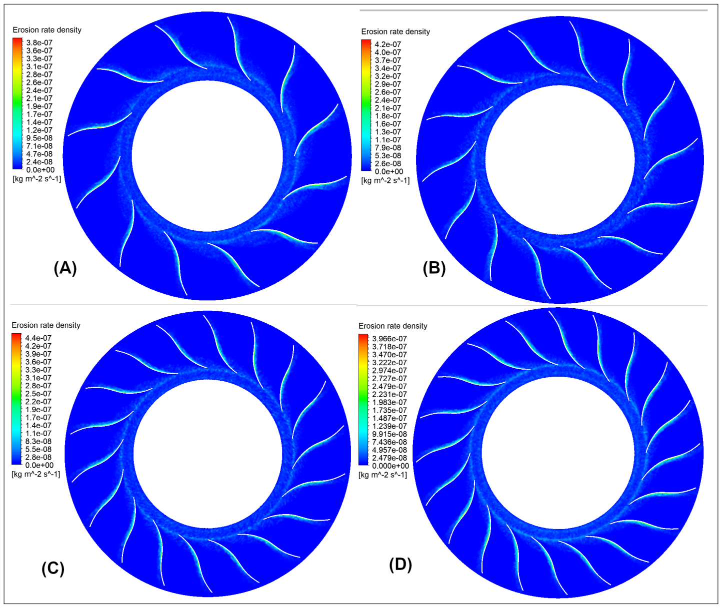

Figure 5.59: Erosion rate density on the impeller hub at 53.9 m^3/s ,A)=12 blades,B)=14 blades,C)=18 blades, D)=20 blades.

5.3.3 Wall thickness reduction per year on the blade pressure side with different number of blades

The data depicted in Fig.5.60 to Fig.5.65, showcasing the erosion patterns on the blade pressure side wall over one year, operating at a flow rate of 53.9 m^3/s and an ideal particle load threshold of 30 mg/m^3, offer valuable insights into the interplay between the number of blades within the impeller and the resultant eroded thickness on the blade pressure side wall. These findings assume a position of profound importance in the realm of centrifugal fan design, particularly when the emphasis is placed on ensuring the durability and structural integrity of fan components under erosive operational conditions.

While the adjustment of the blade count does not appear to have a significant influence on the erosion patterns on the blade pressure side, a discernible trend emerges when fewer blades are employed, resulting in a more pronounced reduction in wall thickness. It is noteworthy that this reduction in wall thickness may not attain statistical significance, yet it becomes particularly evident in sections S4 and S5. Notably, the advantages of increasing the number of blades in this context seem to be relatively limited. It is imperative to recognize that the decision to increase the blade count in a centrifugal fan system should be considered in conjunction with broader performance parameters. The augmentation of the blade count may confer advantages related to enhanced efficiency, thereby positively impacting the overall system performance. Consequently, the selection of the optimal blade count should be the outcome of a comprehensive assessment, one that is rooted in the specific operational demands of the centrifugal fan system.

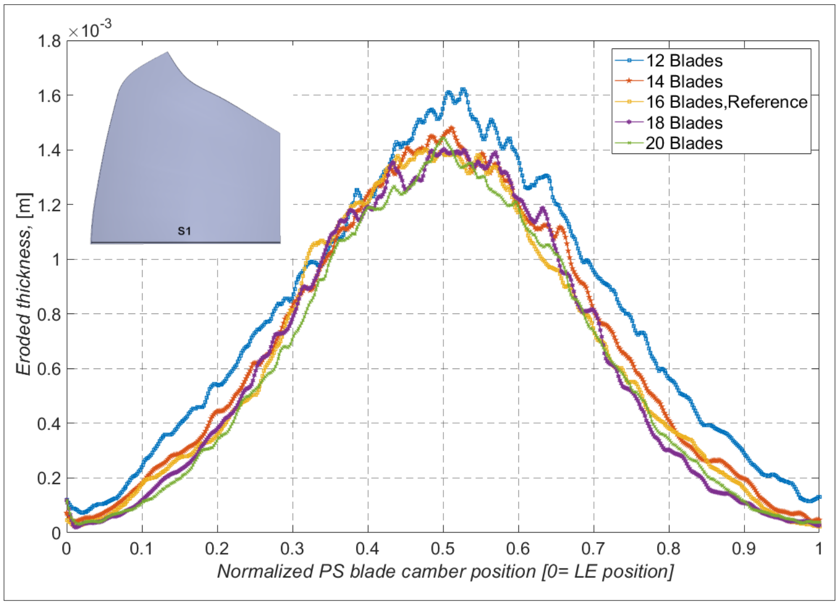

Figure 5.60: Eroded Thickness on Blade PS with various blade numbers along S1.

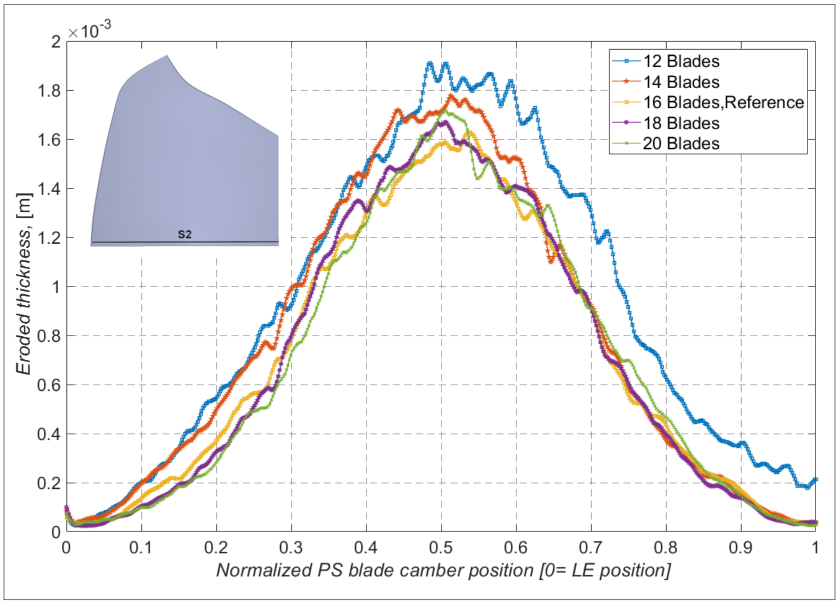

Figure 5.61: Eroded Thickness on Blade PS with various blade numbers along S2.

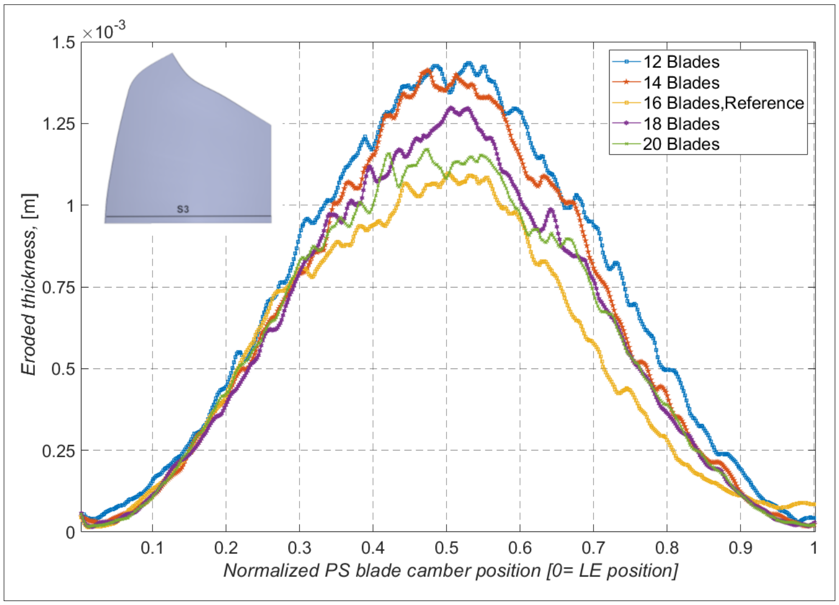

Figure 5.62: Eroded Thickness on Blade PS with various blade numbers along S3.

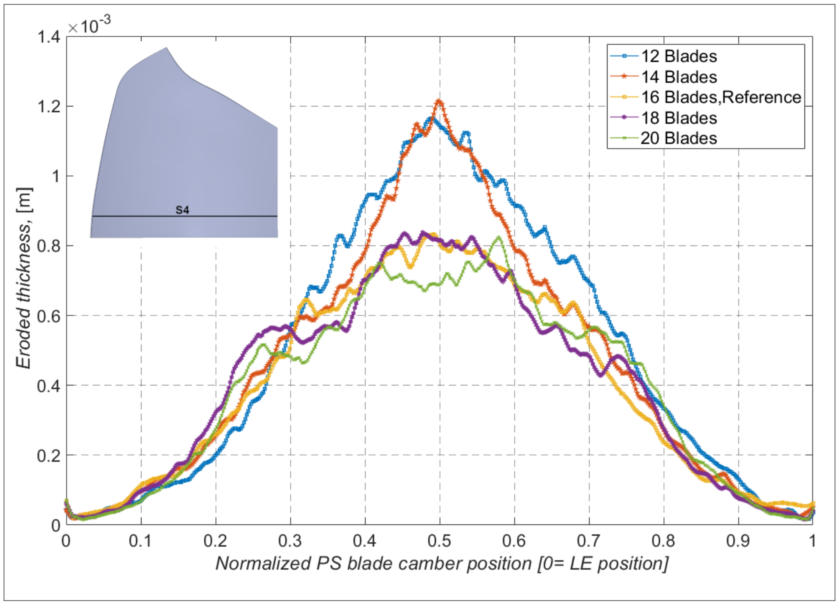

Figure 5.63: Eroded Thickness on Blade PS with various blade numbers along S4.

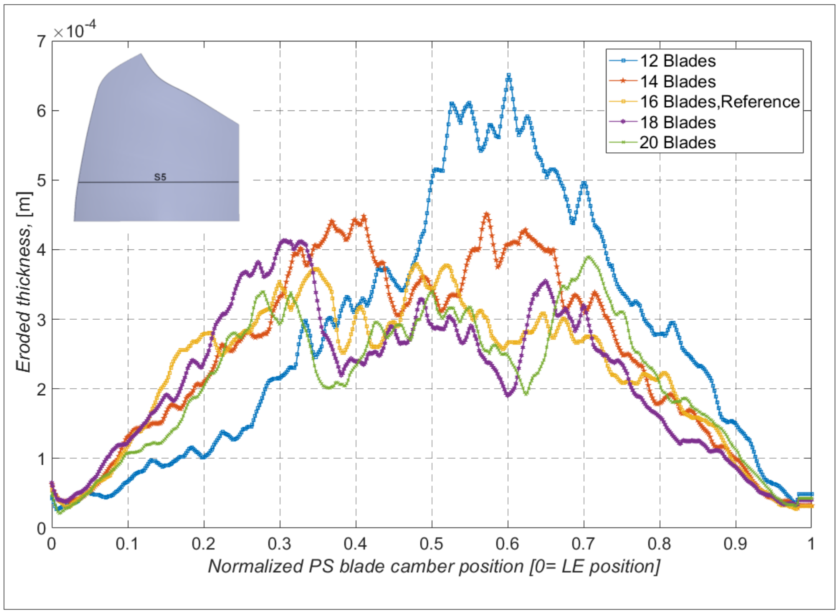

Figure 5.64: Eroded Thickness on Blade PS with various blade numbers along S5.

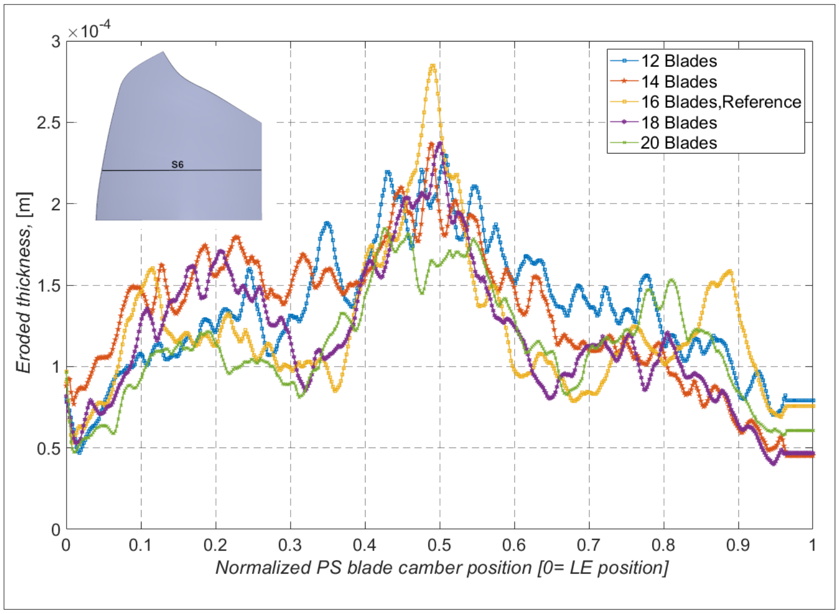

Figure 5.65: Eroded Thickness on Blade PS with various blade numbers along S6.

The chart presented in Fig.5.66 provides valuable insights into the frequencies at which particles impact the blade pressure side under different blade count configurations. The dataset presents a concept analogous to what has been discussed in the section concerning the influence of the blade outlet angle. A marked trend emerges, where the frequency of particle impacts rises alongside an increase in the number of blades in the impeller. Moreover, this increase in impact frequency is observed for both small and large particles, contrary to the intuitive expectation that reducing the number of blades should result in a higher frequency of impacts.

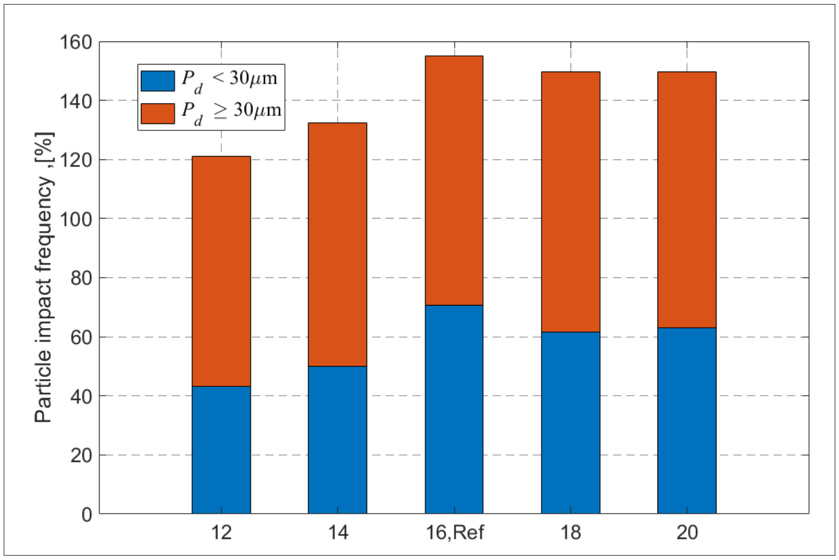

Figure 5.66: Particle impact frequency distribution on the blade PS with various number of blades.

In order to delve deeper into the complex correlation between the number of blades of the impeller and the attributes of particle impacts on the blade's pressure side, Figures 5.67 to 5.70 provide critical insights into the distribution of impact velocity and angle across various blade number configurations.

When considering large-size particles, a noteworthy pattern consistently emerges across all blade count variations. These particles tend to hit the blade surface within a relatively confined velocity range, typically spanning from 40 m/s to 90 m/s. Notably, large particles predominantly exhibit impact velocities within the 60-70 m/s and

70-80 m/s ranges. However, what stands out is the discernible impact of blade count variations within the impeller. As the number of blades increases, a notable shift in impact velocity probability becomes evident, with the probability of impact velocities concentrating within the 70-80 m/s range. In fact, this specific velocity range attains the highest probability, reaching 43% for an impeller configuration featuring 20 blades. Turning our attention to small-size particles, a distinct preference emerges for impacting the blade at moderate velocities, typically ranging from 20 m/s to 70 m/s. These particles exhibit a significant probability of impact within the velocity range of 30-60 m/s. Similar to their larger counterparts, small particles demonstrate a pattern of shifting impact velocities. Specifically, the highest impact velocity values shift from the 30-40 m/s and 40-50 m/s ranges towards the 50-60 m/s range, followed by a substantial increase in the probability of impact velocity within the 60-70 m/s range. It's important to note that the impact velocity charts for blade configurations from 12 blades to 20 blades remain consistent with the impact velocity distribution for the reference impeller configuration, featuring 16 blades (as depicted in Fig.5.19. This consistency further solidifies the observed trend: increasing the number of blades consistently leads to a pronounced increase in the probability of impact velocities within higher ranges for both small and large particles.

analyzing the distribution of impact angles and comparing them with the impact angle probability distribution for the reference model, similar trends emerge across various blade count configurations. For large-size particles, the probability of impact angles increases from the 0-5° range towards the 15-20° range, where it reaches its peak then it decreases for higher angles. As the number of blades increases, the probability of impact angles within the 15-20° range escalates. Conversely, small-size particles tend to strike the blade surface at lower impact angles, with the maximum probability occurring within the 0-5° range (approximately 50%), gradually decreasing for higher impact angles. This pattern remains consistent throughout the impeller configurations, spanning from 12 blades to 20 blades.

Considering the probability distributions of impact angles and velocities, it becomes evident that increasing the number of blades results in heightened impact velocity probabilities and impact angles resulting in maximum erosion rates. However, it's worth noting that impeller designs with fewer blades, such as those featuring 12 and 14 blades, appear to be more susceptible to high erosion rates, particularly in the central region of the blade cord length. Furthermore, the impact frequency, as depicted in Fig.5.66, indicates a lower total impact frequency for impellers with fewer blades. Consequently, we can deduce that the relatively high erosion rates on the blade surface of impellers with 12 and 14 blades should be attributed to the higher local impact frequency occurring in the central region of the blade cord length.

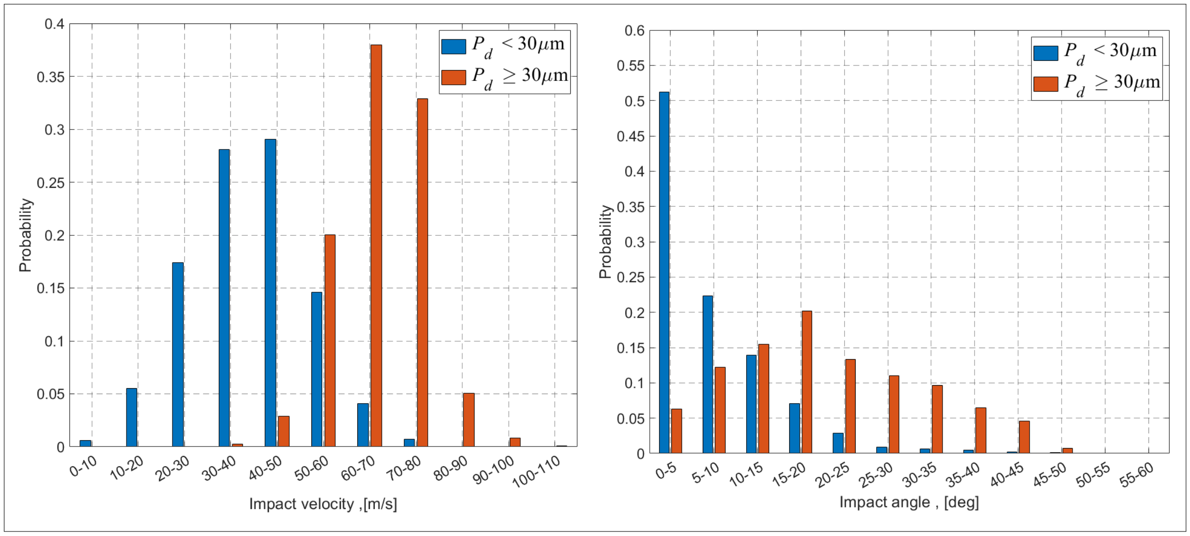

Figure 5.67: Probability of impact Angles and impact Velocities on the Blade PS with 12 blades.

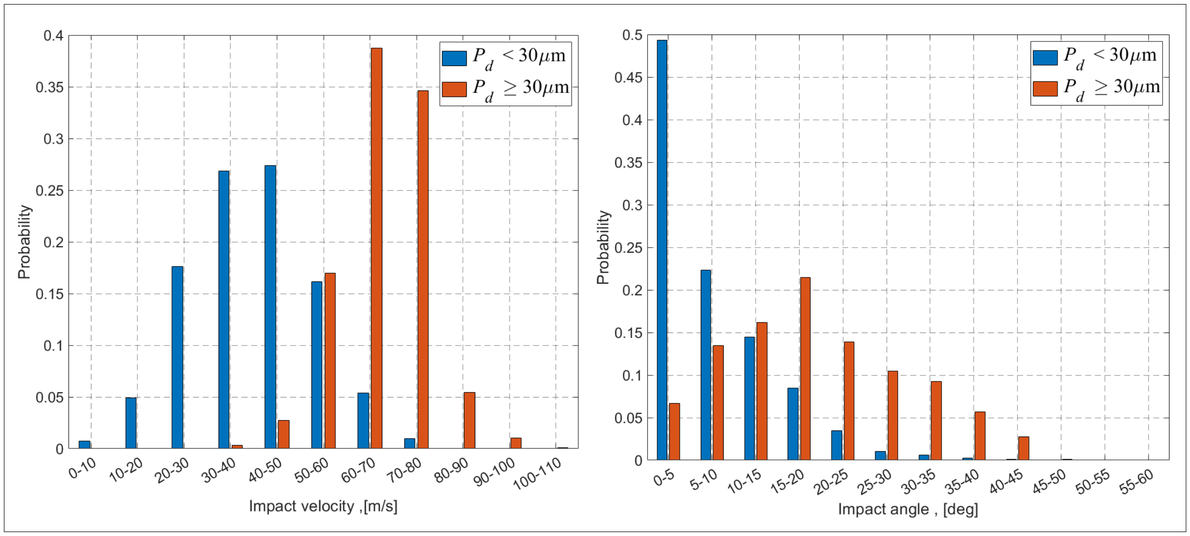

Figure 5.68: Probability of impact Angles and impact Velocities on the Blade PS with 14 blades.

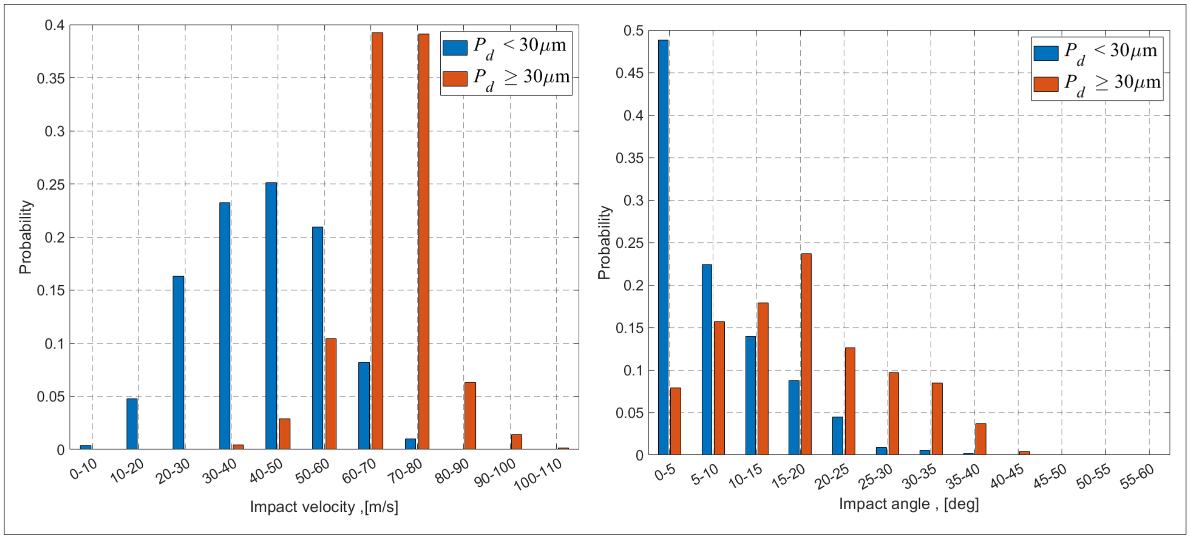

Figure 5.69: Probability of impact Angles and impact Velocities on the Blade PS with 18 blades.

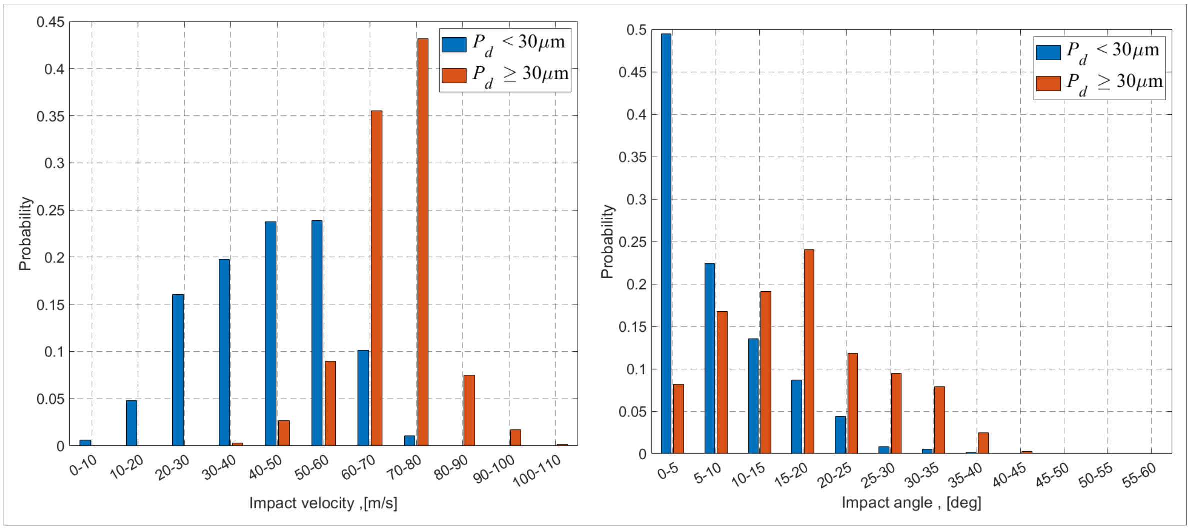

Figure 5.70: Probability of impact Angles and impact Velocities on the Blade PS with 20 blades.

Chapter 6

Concluding remarks and recommendations for further work

6.1 Concluding remarks

the production of cement is a very demanding process that involves several critical production steps. Harsh environments with abrasive and adhering media put a constant strain on all components, including industrial fans and blowers. Centrifugal fans are widely used in the cement industry to manage specific manufacturing processes such as for conveying, exhausting, dedusting, cooling, and fresh air supply, as well as in the kiln burning and cooling process. where the fans used operate under harsh conditions and must withstand high temperatures. Likewise, high dust loads are a challenge for all components of industrial fans, especially for moving parts. The highly abrasive particles in dust-laden gases can lead to fan's component erosion. This can decrease the fan's performance and lead to substantial costs and production losses if the eroded parts need replacement. Therefore, thoughtful design and experience in the manufacture of radial fans in the cement industry are required. Despite the broad range of applications of centrifugal fans in the cement plant, the erosion process and pattern of this type of fan have not been extensively investigated and understood in detail. this thesis attempts to shed some light on the performance characteristics and erosion occurrence in the backward-S curved fan (FN-280) particularly the impeller part through numerical investigations.

For the purpose of this investigation, Computational Fluid Dynamics (CFD) has been used to simulate air-solid two-phase flow with the use of the Eulerian-Lagrangian model in the whole domain of the centrifugal fan under study. The CAD model of the centrifugal fan was designed using SOLIDWORKS whereas the blades were reconstructed using reverse engineering by means of CMM (Coordinate measuring machine) because of the lack of blade geometry drawings. the flow field within the fan domain was obtained by carrying out numerical simulations at various operating points at a rotating speed of 985rpm. A commercially available computational fluid dynamics (CFD) package CFX has been employed for the numerical simulations including both performance and erosion prediction.The modeling approach is validated by comparing the deviation of numerical results from The aerodynamic performance curves of the studied fan experimentally derived in accordance with the industrial fan testing standard ISO 5801 requirements. the modeling approach of the flow field follows two steps, A steady state simulation based on RANS K_ω turbulence model using the MRF approach was first carried out, and then the converged solution obtained is used as an initial solution for the unsteady simulation using the sliding mesh technique. the computational domain of the fan was spatially discretized by means of ANSYS ICEM-CFD using unstructured tetrahedral grids for the fan domain's core region. To address the coupling between the stationary and rotating domains, the computational domain was partitioned into multiple zones with sliding interfaces, allowing the flux to pass through non-conformal mesh connections during unsteady simulation.

The solid phase dispersion was modeled by a Lagrangian approach. solid particles were injected into the flow domain and the particles were tracked using a polydisperse particle transport Model. To account for the actual composition of the cement powder, Particles were characterized by different geometrical properties. the size distribution of the particles was conducted using the particle size analyzer called Mastersizer 3000. the mass flow rate of injected particles at each particle tracking simulation was determined by taking into account the particle's concentration, the total volume flow rate of the carrier fluid, and the particle size distribution. Erosion rates were accounted for by using the erosion model due to Tabakoff and Grant.

Based on the results from this study, it has been concluded that the unsteady (URANS) simulation can accurately predict the performance curve data and is found to be in good agreement with experimental data. the numerical approach predicted the total pressure rises and the power output within a reasonable error. The unsteady simulation adopted under-predicted the total pressure rise by a maximum of 2.55% and over-predicted the power output by 3.81%.The steady MRF approach, on the other hand, overpredicted the power output by 9.81% in average, which shows that the flow field within the impeller passage was not properly resolved even at design working condition. This accuracy limitation stems from the simplification that consists of neglecting the unsteady interaction between the impeller and the volute. The analysis of the flow evolution revealed that there was always some level of flow separation in the blade passage near the blade suction side, with this flow pattern being consistent across all blade passages, except for high-load regimes where there was moderate flow separation in specific blade passages upstream of the casing tongue and in the casing throat section.

The study's findings indicate that particle transport results show that large particles ($d_p \geq 30\,\mu m$) cause high impact frequency on the blade pressure side, leading edge, and impeller hub, while smaller particles ($d_p < 30\mu m$) mainly affect the blade suction side and the whole blade pressure side. Although small particles hit almost the entire blade pressure side surface, analysis of the two erosion process factors, incidence angle, and impact velocity, revealed that large-size particles are the main cause of blade pressure side wear due to the fact that their impacts occur at high-velocity and at an impact angle that results in the highest erosion rate. The lower mid-span and the top part of the leading-edge strip of the blade pressure side and the blade-hub junction of the impeller hub are the most affected areas by large-size particle impact. The authors also found that The blade root of the pressure side and the hub-blade pressure side junction have the most extreme erosion, while the blade suction side experiences little wear. The erosion rate is heavily influenced by operating conditions, and maximum erosion rates occur at off-design operating conditions, which are ten times greater than the design flow rate, The non-uniformity of fluid dynamics at each blade passage significantly determines the erosion rate on the blade surface and the impeller hub, particularly under high-load operating conditions. The comparison between CFD predictions and on-field erosion detections proves the reliability of the numerical results and the model's ability to replicate the actual erosion patterns. This information can be used to modify the fan design to reduce the erosion rate.

The effects of different geometrical modifications on the erosion and performance of the fan have been investigated in this thesis. the effects of the blade's outlet angle, as well as the number of blades, are studied by performing numerical simulations. in summary, the investigation into the effect of the blade outlet angle on the centrifugal fan's performance and erosion pattern reveals distinct trends. It is concluded that increasing the outlet angle leads to higher total pressure and torque but negatively impacts efficiency, especially at higher flow rates. Conversely, decreasing the blade outlet angle leads to lower total pressure and torque but has the potential to enhance the fan efficiency at moderate and low flow rates. Additionally, reducing the blade outlet angle confines flow separations near the blade's suction side, offering aerodynamic advantages, especially at high flow rates. This observation aligns with the improved performance noted in impellers featuring blades with narrower outlet angles.

For the assessment of the effect of blade outlet angle on the erosion pattern and rates, particularly on the blade pressure side, this assessment was conducted By plotting the thickness of eroded material along the normalized blade camber length at six distinct sections on the blade pressure side surface. Assessing the thickness reduction at six specific sections demonstrated a consistent trend: eroded thickness decreases as the blade's outlet angle decreases. This pattern is remarkably similar across all sections. the flow field conditions alteration for each blade outlet angle configuration leads to different particle impact characteristics, such as the velocity and angle of impacts and impact frequency, for each blade outlet angle. Thus, an analysis of these key factors influencing the erosion rates revealed that while blade outlet angle variations have a significant impact on the angles of impact and particle impact frequency, the velocity impact distribution remains relatively consistent across different blade outlet angles.

This highlights that the primary driver of higher erosion rates at larger blade outlet angles is the combination of particle impact angle and impact frequency.

The study also revealed that varying the number of blades has a comparatively lesser impact on both the erosion pattern and its magnitude in contrast to changes in the blade outlet angle. While this geometric alteration may not initially seem to exert a significant influence on erosion patterns on the pressure side of the blade, a noticeable trend emerges when a reduced number of blades are employed, resulting in a more prominent reduction in wall thickness.

Upon scrutinizing the probability distributions of particle impact characteristics, it was noted that an increase in the number of blades led to higher probabilities of encountering high impact velocities, increased impact frequency, and impact angles within the range associated with maximum erosion rates. This potential consequence could result in elevated erosion rates. Despite this, the findings showed that impeller designs with fewer blades, specifically those featuring 12 and 14 blades, were more susceptible to experiencing high erosion rates, especially in the central region of the blade cord length. Consequently, it was suggested that the relatively heightened erosion rates on the blade surface of impellers featuring 12 and 14 blades could be attributed to the increased local impact frequency occurring in the central region of the blade cord length.

6.2 Recommendations for further work

This section outlines recommendations for future research inspired by the findings of this thesis. By identifying potential areas for further exploration, These recommendations aim to inspire future researchers and contribute to the advancement of knowledge in this field.

- This study utilized the Lagrangian Particle transport model with one-way coupling, which does not account for the influence of particles on the fluid and particle-particle collisions. Consequently, there is a need to investigate how these interactions affect particle transport dynamics and erosion patterns. The Discrete Element Method (DEM) emerges as a promising modeling technique capable of providing detailed insights into individual particle behavior and accurately simulating particle-particle interactions.

- Furthermore, the assumption that the surface profile of the wall remains unchanged throughout the erosion analysis disregards the alteration of particle impingement and impact on the fluid flow.
- To enhance the accuracy of erosion predictions in this study, it is recommended to conduct proper experimental analyses with identical particle and target surface proprieties.

Bibliography

[1] David S-K. Ting. Chapter 3 - statistical description of flow turbulence. In David S-K. Ting, editor, *Basics of Engineering Turbulence*, pages 47–68. Academic Press, 2016.

[2] Kenneth C Wilson, Graeme R Addie, Anders Sellgren, and R Clift. *Slurry transport using centrifugal pumps.* Springer Science & Business Media, 2006.

[3] Lampros-Gerasimos Giourntas. *Investigation of erosion-corrosion behaviour of pump materials.* PhD thesis, University of Strathclyde, 2016.

[4] Jasem Alqallaf, Naser Ali, Joao A Teixeira, and Abdulmajid Addali. Solid particle erosion behaviour and protective coatings for gas turbine compressor blades—a review. *Processes*, 8(8):984, 2020.

[5] Vahid Javaheri, David Porter, and Veli-Tapani Kuokkala. Slurry erosion of steel–review of tests, mechanisms and materials. *Wear*, 408:248–273, 2018.

[6] JGA Bitter. A study of erosion phenomena part i. *wear*, 6(1):5–21, 1963.

[7] Iain Finnie. Some reflections on the past and future of erosion. *Wear*, 186:1–10, 1995.

[8] Oluwademilade Adekunle Ogunsesan. *CFD modelling of pipe erosion under multiphase flow regimes.* PhD thesis, 2020.

[9] D Ramajo, M Raviculé, R Benini, S Marquez Damian, M Storti, and N Nigro. Diagnose and prediction of erosion-corrosion damage in a pipeline transporting reduced crude oil from the heater to the vacuum distillation tower. *Mecánica Computacional*, 28(19):1621–1639, 2009.

[10] Iain Finnie. Erosion of surfaces by solid particles. *wear*, 3(2):87–103, 1960.

[11] Alan V Levy. The platelet mechanism of erosion of ductile metals. *Wear*, 108(1):1–21, 1986.

[12] A Hamed, WC Tabakoff, and RV Wenglarz. Erosion and deposition in turbomachinery. *Journal of propulsion and power*, 22(2):350–360, 2006.

[13] Pankaj P Shitole, Shravan H Gawande, Girish R Desale, and Bhushan D Nandre. Effect of impacting particle kinetic energy on slurry erosion wear. *Journal of Bio- and Tribo-Corrosion*, 1:1–9, 2015.

[14] Shuaijun Zhang, Junqiu Zhang, Bin Zhu, Shichao Niu, Zhiwu Han, and Luquan Ren. Progress in bio-inspired anti-solid particle erosion materials: Learning from nature but going beyond nature. *Chinese journal of mechanical engineering*, 33:1–27, 2020.

[15] Iain Finnie. Some observations on the erosion of ductile metals. *wear*, 19(1):81–90, 1972.

[16] G Grant and Widen Tabakoff. Erosion prediction in turbomachinery resulting from environmental solid particles. *Journal of Aircraft*, 12(5):471–478, 1975.

[17] IM Hutchings and RE Winter. Particle erosion of ductile metals: a mechanism of material removal. *Wear*, 27(1):121–128, 1974.

[18] IM Hutchings and RE Winter. The erosion of ductile metals by spherical particles. *Journal of Physics D: Applied Physics*, 8(1):8, 1975.

[19] Ian M Hutchings. Ductile-brittle transitions and wear maps for the erosion and abrasion of brittle materials. *Journal of Physics D: Applied Physics*, 25(1A):A212, 1992.

[20] G Sundararajan and PG Shewmon. A new model for the erosion of metals at normal incidence. *Wear*, 84(2):237–258, 1983.

[21] Joshua James Owen. *Erosion-Corrosion of Carbon Steel in Complex Flow Geometries in Oil & Gas CO2 Environments.* PhD thesis, University of Leeds, 2018.

[22] I.M. Hutchings. Wear by particulates. *Chemical Engineering Science*, 42(4):869–878, 1987.

[23] Alan V Levy. The solid particle erosion behavior of steel as a function of microstructure. *Wear*, 68(3):269–287, 1981.

[24] YI Oka, H Ohnogi, T Hosokawa, and M Matsumura. The impact angle dependence of erosion damage caused by solid particle impact. *Wear*, 203:573–579, 1997.

[25] JG Mbabazi, TJ Sheer, and R Shandu. A model to predict erosion on mild steel surfaces impacted by boiler fly ash particles. *Wear*, 257(5-6):612–624, 2004.

[26] QB Nguyen, DN Nguyen, R Murray, NX Ca, CYH Lim, M Gupta, and XC Nguyen. The role of abrasive particle size on erosion characteristics of stainless steel. *Engineering Failure Analysis*, 97:844–853, 2019.

[27] Markus Liebhard and Alan Levy. The effect of erodent particle characteristics on the erosion of metals. *Wear*, 151(2):381–390, 1991.

[28] Alessandro Corsini, Andrea Marchegiani, Franco Rispoli, Paolo Venturini, and Anthony G Sheard. Predicting blade leading edge erosion in an axial induced draft fan. 2012.

[29] NICOlò BECCaTI, CrISTIaN FErrarI, MarCO ParMa, and MaSSIMO SEMPrINI. Eulerian multi-phase cfd model for predicting the performance of a centrifugal dredge pump. 2019.

[30] Yunqing Gu, Nuojia Liu, Jiegang Mou, Peijian Zhou, Heng Qian, and Dongshun Dai. Study on solid–liquid two-phase flow characteristics of centrifugal pump impeller with non-smooth surface. *Advances in Mechanical Engineering*, 11(5):1687814019848269, 2019.

[31] Rahul Tarodiya and Bhupendra K Gandhi. Numerical simulation of a centrifugal slurry pump handling solid-liquid mixture: Effect of solids on flow field and performance. *Advanced Powder Technology*, 30(10):2225–2239, 2019.

[32] Yanping Wang, Bozhou Chen, Ye Zhou, Jianfeng Ma, Xinglin Zhang, Zuchao Zhu, and Xiaojun Li. Numerical simulation of fine particle solid-liquid two-phase flow in a centrifugal pump. *Shock and Vibration*, 2021:1–10, 2021.

[33] Guangjie Peng, Fengyi Fan, Ling Zhou, Xin Huang, and Junfei Ma. Optimal hydraulic design to minimize erosive wear in a centrifugal slurry pump impeller. *Engineering Failure Analysis*, 120:105105, 2021.

[34] Khaled Alawadhi, Bashar Alzuwayer, Mosab Alrahmani, and Ahmed Murad. Evaluation of the erosion characteristics for a marine pump using 3d rans simulations. *Applied Sciences*, 11(16):7364, 2021.

[35] ZJ Shen, RN Li, W Han, WG Zhao, and XH Wang. The research on particle trajectory of solid-liquid two-phase flow and erosion predicting in screw centrifugal pump. In *IOP Conference Series: Materials Science and Engineering*, volume 129, page 012052. IOP Publishing, 2016.

[36] Zhengjing Shen, Wuli Chu, Xiangjun Li, and Wei Dong. Sediment erosion in the impeller of a double-suction centrifugal pump–a case study of the jingtai yellow river irrigation project, china. *Wear*, 422:269–279, 2019.

[37] Xijie Song, Dunzhe Qi, Lijuan Xu, Yubin Shen, Wei Wang, Zhengwei Wang, and Yan Liu. Numerical simulation prediction of erosion characteristics in a double-suction centrifugal pump. *Processes*, 9(9):1483, 2021.

[38] Yexiang Xiao, Bao Guo, Soo-Hwang Ahn, Yongyao Luo, Zhengwei Wang, Guangtai Shi, and Yanhao Li. Slurry flow and erosion prediction in a centrifugal pump after long-term operation. *Energies*, 12(8):1523, 2019.

[39] Seung Jun Na, Young Shin Kim, and Euy Sik Jeon. Analysis of erosion minimization for a slurry pump using discrete phase model simulations. *Applied Sciences*, 12(3):1597, 2022.

[40] Fabian Hankeln and Stefan Riedelbauch. Comparison of different models for determination of erosion wear in centrifugal pumps. In *13 th European Conference on Turbomachinery Fluid dynamics & Thermodynamics*. EUROPEAN TURBOMACHINERY SOCIETY, 2019.

[41] Wenqi Zhang, Shuai Yang, Dazhuan Wu, and Jiegang Mou. Effect of particle mass concentration on erosion characteristics of self-priming pump. *Proceedings of the Institution of Mechanical Engineers, Part C: Journal of Mechanical Engineering Science*, 235(23):6782–6797, 2021.

[42] Zhongqian Jiang, Xiaodong Zeng, and Yi Li. Study on the relationship between wear and flow characteristics of a centrifugal pump at different mass concentrations. *Processes*, 9(6):988, 2021.

[43] Yanping Wang, Ruilin Tao, Chuanfeng Han, Weiqin Li, Tielin He, and Zuchao Zhu. Numerical study on flow and wear characteristics of dense fine particle solid–liquid two-phase flow in centrifugal pump. *AIP Advances*, 12(4), 2022.

[44] Haoyu Wang, Zhen Tan, Shibo Kuang, and Aibing Yu. Numerical modeling and analysis of particle-fluid flow and wall erosion in centrifugal slurry pumps under different solid concentrations. *Powder Technology*, 410:117861, 2022.

[45] Nicola Aldi, Nicola Casari, Michele Pinelli, Alessio Suman, Alessandro Vulpio, Paolo Saccenti, Riccardo Beretta, Annalisa Fortini, Mattia Merlin, et al. Erosion behavior on a large-sized centrifugal fan. In *Proceedings of the 13th European Turbomachinery Conference on Turbomachinery Fluid Dynamics and Thermodynamics, ETC*, pages 1–8, 2019.

[46] SG Sapate and AV RamaRao#. Effect of erodent particle hardness on velocity exponent in erosion of steels and cast irons. *Materials and manufacturing processes*, 18(5):783–802, 2003.

[47] Nicola Aldi, Nicola Casari, Michele Pinelli, Alessio Suman, Alessandro Vulpio, Ottavio Mantovani, and Paolo Saccenti. Evaluation of the wear-resistant plate performance on different locations over the flow path of a large-sized heavy-duty centrifugal fan. *International Journal of Turbomachinery, Propulsion and Power*, 7(4):32, 2022.

[48] ASTM G76. Standard test method for conducting erosion tests by solid particle impingement using gas jets, 2004.

[49] Ian Finnie and DH McFadden. On the velocity dependence of the erosion of ductile metals by solid particles at low angles of incidence. *Wear*, 48(1):181–190, 1978.

[50] Y Isomoto Oka, K Okamura, and T Yoshida. Practical estimation of erosion damage caused by solid particle impact: Part 1: Effects of impact parameters on a predictive equation. *Wear*, 259(1-6):95–101, 2005.

[51] Zhiwu Han, Hailong Feng, Wei Yin, Shichao Niu, Junqiu Zhang, and Daobing Chen. An efficient bionic anti-erosion functional surface inspired by desert scorpion carapace. *Tribology Transactions*, 58(2):357–364, 2015.

[52] Zhiwu Han, Bin Zhu, Mingkang Yang, Shichao Niu, Honglie Song, and Junqiu Zhang. The effect of the micro-structures on the scorpion surface for improving the anti-erosion performance. *Surface and Coatings Technology*, 313:143–150, 2017.

[53] He Huang, Yan Zhang, and Luquan Ren. Particle erosion resistance of bionic samples inspired from skin structure of desert lizard, laudakin stoliczkana. *Journal of bionic engineering*, 9(4):465–469, 2012.

[54] YuHang Zhang, He Huang, and LuQuan Ren. Erosion wear experiments and simulation analysis on bionic anti-erosion sample. *Science China Technological Sciences*, 57:646–650, 2014.

[55] Junqiu Zhang, Zhiwu Han, Wei Yin, Huiyuan Wang, Chao Ge, and Jialian Jiang. Numerical experiment of the solid particle erosion of bionic configuration blade of centrifugal fan. *Acta Metallurgica Sinica (English Letters)*, 26:16–24, 2013.

[56] Adel Ghenaiet. Study of particle dynamics and erosion in a centrifugal fan. In *Proc. 14th European Conference on Turbomachinery Fluid Dynamics & Thermodynamics ETC14*, pages 12–16, 2021.

[57] Manuel Fritsche, Philipp Epple, Michael Steber, and Hans J Rußwurm. Erosion optimized radial fan impellers and volutes for particle flows. In *ASME International Mechanical Engineering Congress and Exposition*, volume 58424, page V007T09A071. American Society of Mechanical Engineers, 2017.

[58] P Venturini. *Modelling of particle-wall deposition in two-phase gas-solid flows.* PhD thesis, Sapienza University of Rome, 2010.

[59] Alessandro Corsini, Giovanni Delibra, and Anthony G Sheard. A critical review of computational methods and their application in industrial fan design. *International Scholarly Research Notices*, 2013, 2013.

[60] Lucio Cardillo, Alessandro Corsini, Giovanni Delibra, Franco Rispoli, Anthony G Sheard, and Paolo Venturini. Predicting the performance of an industrial centrifugal fan incorporating cambered plate impeller blades. *Periodica Polytechnica Mechanical Engineering*, 58(1):15–25, 2014.

[61] W Tabakoff, R Kotwal, and A Hamed. Erosion study of different materials affected by coal ash particles. *Wear*, 52(1):161–173, 1979.

[62] Lucio Cardillo, Alessandro Corsini, Giovanni Delibra, Franco Rispoli, Anthony G Sheard, and Paolo Venturini. Simulation of particle-laden flows in a large centrifugal fan for erosion prediction. In *Turbo Expo: Power for Land, Sea, and Air*, volume 45578, page V01AT10A014. American Society of Mechanical Engineers, 2014.

[63] Alessandro Corsini, Franco Rispoli, Anthony G Sheard, and Paolo Venturini. Numerical simulation of coal fly-ash erosion in an induced draft fan. *Journal of fluids engineering*, 135(8):081303, 2013.

[64] Alessandro Corsini, Franco Rispoli, Paolo Venturini, and Anthony G Sheard. Numerical modelling of erosion in highly-loaded axial flow fans. In *Gas Turbine India Conference*, volume 45165, pages 793–802. American Society of Mechanical Engineers, 2012.

[65] F.P. Bleier. *Fan Handbook: Selection, Application, and Design*. McGraw-Hill Education, 1998.

[66] Manoochehr Darvish. *Numerical and experimental investigations of the noise and performance characteristics of a radial fan with forward-curved blades*. PhD thesis, Berlin, Technische Universität Berlin, Diss., 2015, 2015.

[67] Aerovent, 2021.

[68] Y. Cengel and J. Cimbala. *Fluid Mechanics Fundamentals and Applications: Third Edition*. MCGRAW-HILL US HIGHER ED, 2013.

[69] Gerard W McKervey and B Perry. Fan applications in the cement industry. In *[1993] Record of Conference Papers 35th IEEE Cement Industry Technical*, pages 467–476. IEEE, 1993.

[70] D.J. Gingery. *How To Design & Build Centrifugal Fans For the Home Shop*. David J. Gingery Publishing, LLC, 2014.

[71] Allen L Ray and Derek Couse. Cement plant fan efficiency upgrades. *IEEE Transactions on Industry Applications*, 53(2):1562–1568, 2016.

[72] P.A. Alsop. *Cement Plant Operations Handbook: For Dry Process Plants*. International Cement Review. Tradeship Publications, 2007.

[73] A.K. Chatterjee. *Cement Production Technology: Principles and Practice*. CRC Press, 2018.

[74] Din 5801 industrial fans-performance testing using standardized airways.international organisation for standardization. 2007.

[75] Vinesh Raja and Kiran J Fernandes. *Reverse engineering: an industrial perspective*. Springer Science & Business Media, 2007.

[76] Tamas Varady, Ralph R Martin, and Jordan Cox. Reverse engineering of geometric models—an introduction. *Computer-aided design*, 29(4):255–268, 1997.

[77] Gayatri D Barai, Sunil S Shete, and Laukik P Raut. Design and development of a component by reverse engineering. *IJRET: International Journal of Research in Engineering and Technology, eISSN*, pages 2319–1163, 2015.

[78] Zoran Pandilov, Betim Shabani, Dejan Shishkovski, and Gligorche Vrtanoski. Reverse engineering–an effective tool for design and development of mechanical parts. *Acta Technica Corviniensis-Bulletin of Engineering*, 11(2):113–118, 2018.

[79] Atul Kumar, Pramod Kumar Jain, and Pushparaj Mani Pathak. Reverse engineering in product manufacturing: an overview. *DAAAM international scientific book*, 39:665–678, 2013.

[80] 3D Systems, Inc. Geomagic Solutions. *Geomagic Design X User Guide*, 2013.

[81] John F. Wendt. *Computational Fluid Dynamics - An Introduction.* Springer, Berlin, 3 edition, 2009.

[82] Joel H. Ferziger, Milovan Perić, and Robert L. Street. *Basic Concepts of Fluid Flow*, pages 1–21. Springer International Publishing, Cham, 2020.

[83] W. Michael Lai, David Rubin, and Erhard Krempl. Chapter 6 - newtonian viscous fluid. In W. Michael Lai, David Rubin, and Erhard Krempl, editors, *Introduction to Continuum Mechanics (Fourth Edition)*, pages 353–410. Butterworth-Heinemann, Boston, fourth edition edition, 2010.

[84] Amir A. Aliabadi. *Introduction*, pages 3–5. Springer International Publishing, Cham, 2022.

[85] I.M. Cohen and P.K. Kundu. *Fluid Mechanics*. Fluid Mechanics Series. Elsevier Science, 2007.

[86] Hermann Schlichting (Deceased) and Klaus Gersten. *Onset of Turbulence (Stability Theory)*, pages 415–496. Springer Berlin Heidelberg, Berlin, Heidelberg, 2017.

[87] S.B. Pope and S.B. Pope. *Turbulent Flows*. Cambridge University Press, 2000.

[88] H. K. (Henk Kaarle) Versteeg. *An introduction to computational fluid dynamics : the finite volume method*. Pearson Education Ltd., Harlow, England ;, 2nd ed. edition, 2007.

[89] S. Rodriguez. *Applied Computational Fluid Dynamics and Turbulence Modeling: Practical Tools, Tips and Techniques*. Springer International Publishing, 2019.

[90] M. Tabatabaian. *CFD Module: Turbulent Flow Modeling*. Multiphysics modeling. Mercury Learning and Information, 2015.

[91] Jerry Westerweel, Bendiks J Boersma, and Frans TM Nieuwstadt. *Turbulence: Introduction to Theory and Applications of Turbulent Flows*. Springer International Publishing, 2016.

[92] J. Blazek. Chapter 7 - turbulence modelling. In J. Blazek, editor, *Computational Fluid Dynamics: Principles and Applications (Second Edition)*, pages 227–270. Elsevier Science, Oxford, second edition edition, 2005.

[93] R.H. Pletcher, J.C. Tannehill, and D. Anderson. *Computational Fluid Mechanics and Heat Transfer, Second Edition*. Series in Computational and Physical Processes in Mechanics and Thermal Sciences. Taylor & Francis, 1997.

[94] D. C. Wilcox. *Turbulence modelling for CFD*. DCW Industries, La Cañada, 1993.

[95] B.E. Launder and D.B. Spalding. The numerical computation of turbulent flows. *Computer Methods in Applied Mechanics and Engineering*, 3(2):269–289, 1974.

[96] Bengt Andersson, Ronnie Andersson, Love Håkansson, Mikael Mortensen, Rahman Sudiyo, and Berend van Wachem. *Computational Fluid Dynamics for Engineers*. Cambridge University Press, 2011.

[97] David C Wilcox. Reassessment of the scale-determining equation for advanced turbulence models. *AIAA journal*, 26(11):1299–1310, 1988.

[98] Florian R Menter. Performance of popular turbulence model for attached and separated adverse pressure gradient flows. *AIAA journal*, 30(8):2066–2072, 1992.

[99] Florian R Menter. Improved two-equation k-omega turbulence models for aerodynamic flows. Technical report, 1992.

[100] Florian R Menter. Two-equation eddy-viscosity turbulence models for engineering applications. *AIAA journal*, 32(8):1598–1605, 1994.

[101] ANSYS, Inc., http://www.ansys.com. *Ansys Fluent -Theory Guide*, 2020 R1.

[102] T. J. Chung. *Computational Fluid Dynamics*. Cambridge University Press, 2002.

[103] Cecil G Armstrong, Harold J Fogg, Christopher M Tierney, and Trevor T Robinson. Common themes in multi-block structured quad/hex mesh generation. *Procedia Engineering*, 124:70–82, 2015.

[104] Nicole A Kallemeyn, Srinivas C Tadepalli, Kiran H Shivanna, and Nicole M Grosland. An interactive multiblock approach to meshing the spine. *Computer methods and programs in biomedicine*, 95(3):227–235, 2009.

[105] Rafael Ballesteros-Tajadura, Sandra Velarde-Suárez, Juan Pablo Hurtado-Cruz, and Carlos Santolaria-Morros. Numerical calculation of pressure fluctuations in the volute of a centrifugal fan. 2006.

[106] Zhao Yu, Song Li, Wenqi He, Weixiong Wang, Dongtao Huang, and Zhichi Zhu. Numerical simulation of flow field for a whole centrifugal fan and analysis of the effects of blade inlet angle and impeller gap. *HVAC&R Research*, 11(2):263–283, 2005.

[107] Kyung Jung Lee, Il Wung Park, Ki Suk Bang, Yeong Min Kim, and Young Chull Ahn. Optimal design of a plenum fan with three-dimensional blades. *Applied Sciences*, 10(10):3460, 2020.

[108] M Younsi, F Bakir, S Kouidri, and R Rey. Numerical and experimental study of unsteady flow in a centrifugal fan. *Proceedings of the Institution of Mechanical Engineers, Part A: Journal of Power and Energy*, 221(7):1025–1036, 2007.

[109] Thomas Bouquet, Smaïne Kouidri, Farid Bakir, and Robert Rey. Study of the 3d flows in the forward-curved bladescentrifugal fans. *Progress in Computational Fluid Dynamics, an International Journal*, 3(1):13–21, 2003.

[110] CHEAH KEAN WEE. *Unsteady flow in centrifugal pump at design and off-design conditions*. PhD thesis, 2011.

[111] Zhongxin Gao, Wenruo Zhu, Li Lu, Jie Deng, Jianguang Zhang, and Fujun Wuang. Numerical and experimental study of unsteady flow in a large centrifugal pump with stay vanes. *Journal of Fluids Engineering*, 136(7):071101, 2014.

[112] H.W. Oh. *Applied Computational Fluid Dynamics*. IntechOpen, 2012.

[113] WK Hiromi Ariyaratne, EVPJ Manjula, Chandana Ratnayake, and Morten C Melaaen. Cfd approaches for modeling gas-solids multiphase flows–a review. In *Proceedings of The 9th EUROSIM Congress on Modelling and Simulation, EUROSIM 2016, The 57th SIMS Conference on Simulation and Modelling SIMS 2016*, number 142, pages 680–686. Linköping University Electronic Press, 2018.

[114] Xizhong Chen and Junwu Wang. A comparison of two-fluid model, dense discrete particle model and cfd-dem method for modeling impinging gas–solid flows. *Powder Technology*, 254:94–102, 2014.

[115] Maksims Kirpo. *Modeling of turbulence properties and particle transport in recirculated flows*. Citeseer, 2008.

[116] Matteo Chiesa, Vidar Mathiesen, Jens A Melheim, and Britt Halvorsen. Numerical simulation of particulate flow by the eulerian–lagrangian and the eulerian–eulerian approach with application to a fluidized bed. *Computers & chemical engineering*, 29(2):291–304, 2005.

[117] SuryaNarayana Prasad Vegendla, Geraldine J Heynderickx, and Guy B Marin. Comparison of eulerian–lagrangian and eulerian–eulerian method for dilute gas–solid flow with side inlet. *Computers & chemical engineering*, 35(7):1192–1199, 2011.

[118] Salem Alhajraf. Numerical simulation of drifting sand. 2000.

[119] Jesse Capecelatro and Olivier Desjardins. An euler–lagrange strategy for simulating particle-laden flows. *Journal of Computational Physics*, 238:1–31, 2013.

[120] Roland Tebowei. *Computational fluid dynamics (CFD) modelling of critical velocity for sand transport flow regimes in multiphase pipe bends*. PhD thesis, 2016.

[121] JAC Humphrey. Fundamentals of fluid motion in erosion by solid particle impact. *International journal of heat and fluid flow*, 11(3):170–195, 1990.

[122] JS Shirolkar, CFM Coimbra, and M Queiroz McQuay. Fundamental aspects of modeling turbulent particle dispersion in dilute flows. *Progress in Energy and Combustion Science*, 22(4):363–399, 1996.

[123] C.T. Crowe. *Multiphase Flow Handbook*. Mechanical and Aerospace Engineering Series. CRC Press, 2005.

[124] Luis Fernando Echeverri. *MEASUREMENTS AND COMPUTATIONS OF THE FLOW IN FULL-SCALE SUGAR EVAPORATIVE-CRYSTALLIZERS AND IN LAB-SCALE MODELS*. PhD thesis, Citeseer, 2007.

[125] Ian Proudman and JRA Pearson. Expansions at small reynolds numbers for the flow past a sphere and a circular cylinder. *Journal of Fluid Mechanics*, 2(3):237–262, 1957.

[126] CE Lapple and CB Shepherd. Calculation of particle trajectories. *Industrial & Engineering Chemistry*, 32(5):605–617, 1940.

[127] Walter RA Goossens. Review of the empirical correlations for the drag coefficient of rigid spheres. *Powder Technology*, 352:350–359, 2019.

[128] L SCHILLER. Uber die grundlegenden berechnungen bei der schwerkraftaufbereitung. *Z. Vereines Deutscher Inge*, 77:318–321, 1933.

[129] Shiva P Pudasaini and Martin Mergili. A multi-phase mass flow model. *Journal of Geophysical Research: Earth Surface*, 124(12):2920–2942, 2019.

[130] AD Gosman and E Loannides. Aspects of computer simulation of liquid-fueled combustors. *Journal of energy*, 7(6):482–490, 1983.

[131] Fabio Chiti. *Lagrangian studies of turbulent mixing in a vessel agitated by a rushron turbine: positron emission particle tracking (PEPT) and computational fluid dynamics (CFD).* PhD thesis, University of Birmingham, 2008.

[132] W Tabakoff, A Hamed, and M Metwally. Effect of particle size distribution on particle dynamics and blade erosion in axial flow turbines. 1991.

[133] Malvern Instruments Limite, Worcestershire, United Kingdom. *Mastersizer 3000 User Manual*, 2013.

Appendix A

Appendix

A.1 Conditions for the averaging operator

For two instantaneous flow propreties $\varphi = \Phi + \varphi'$ and $\psi = \Psi + \psi'$,the time average proprieties are as follow:

$\overline{\varphi'} = \overline{\psi'} = 0$, $\overline{\varphi'} = \overline{\psi'} = 0$ $\overline{\varphi'} = \overline{\psi'} = 0$, $\overline{\varphi'} = \overline{\psi'} = 0$ $\overline{\varphi'} = \overline{\psi'} = 0$, $\overline{\varphi'} = \overline{\psi'} = 0$ $\overline{\varphi'} = \overline{\psi'} = 0$

A.2 Averaging methods

Time Average: $\langle\phi\rangle = \frac{1}{T}\int_0^T \phi(t), dt$

Spatial Average: $\langle\phi\rangle = \frac{1}{V}\int_V \phi, dV$

Ensemble Average: $\langle\phi\rangle = \lim_{N\to\infty} \frac{1}{N}\sum_{i=1}^N \phi_i$

Favre Averaging: $\phi^F = \frac{\langle\rho\phi\rangle}{\langle\rho\rangle}$

A.3 FN-280 Cement-Mill Fan Specifications

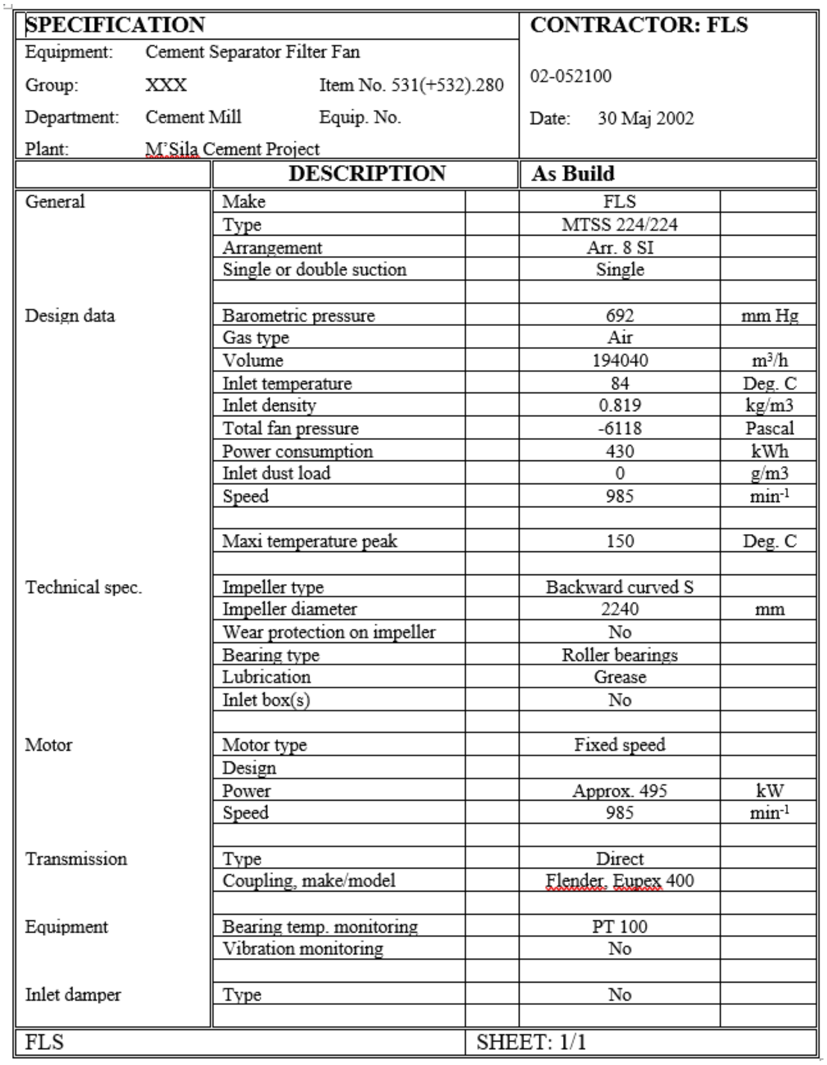

SPECIFICATION

Equipment: Cement Separator Filter Fan
Group: XXX Item No. 531(+532).280
Department: Cement Mill Equip. No.
Plant: M'Sila Cement Project

CONTRACTOR: FLS

02-052100

Date: 30 Maj 2002

	DESCRIPTION		**As Build**	
General	Make		FLS	
	Type		MTSS 224/224	
	Arrangement		Arr. 8 SI	
	Single or double suction		Single	
Design data	Barometric pressure		692	mm Hg
	Gas type		Air	
	Volume		194040	m³/h
	Inlet temperature		84	Deg. C
	Inlet density		0.819	kg/m3
	Total fan pressure		-6118	Pascal
	Power consumption		430	kWh
	Inlet dust load		0	g/m3
	Speed		985	min^{-1}
	Maxi temperature peak		150	Deg. C
Technical spec.	Impeller type		Backward curved S	
	Impeller diameter		2240	mm
	Wear protection on impeller		No	
	Bearing type		Roller bearings	
	Lubrication		Grease	
	Inlet box(s)		No	
Motor	Motor type		Fixed speed	
	Design			
	Power		Approx. 495	kW
	Speed		985	min^{-1}
Transmission	Type		Direct	
	Coupling, make/model		Flender, Eupex 400	
Equipment	Bearing temp. monitoring		PT 100	
	Vibration monitoring		No	
Inlet damper	Type		No	

FLS SHEET: 1/1

Figure A.3: Detailed Fan technical specifications provided by FLS.

A.4 Detailed Casing Dimensions

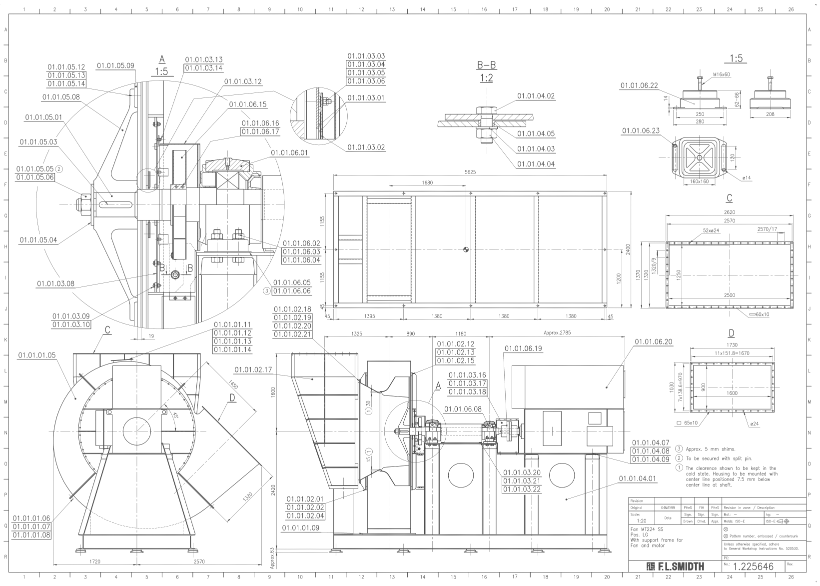

③ Approx. 5 mm shims.
② To be secured with split pin.
① The clearence shown to be kept in the cold state. Housing to be mounted with center line positioned 7.5 mm below center line at shaft.

Revision
Original 04MAY99 PHeS FIH PHeS
Scale: 1:20 Date Sign. Drawn Sign. Chkd. Sign. Appr.
Revision in zone: / Description:
Mat.: — kg: —
Welds: ISO-E ISO-E
Fan MT224 SS
Pos. LG
With support frame for
Fan and motor
⊗ Pattern number, embossed / countersunk
Unless otherwise specified, adhere to General Workshop Instructions No. 520530.
PC:
No.: 1.225646 Rev.

Figure A.4: Casing dimensions provided by FLS.

A.5 Detailed Impeller Dimensions

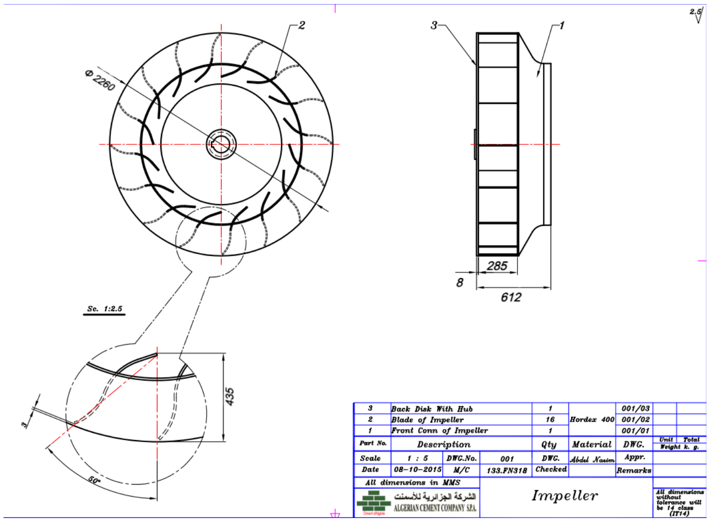

3	Back Disk With Hub	1	Hordex 400	001/03		
2	Blade of Impeller	16		001/02		
1	Front Conn of Impeller	1		001/01		
Part No.	Description	Qty	Material	DWG.	Unit Weight k. g.	Total

Scale	1 : 5	DWG.No.	001	DWG.	Abdel Nasim	Appr.	
Date	08-10-2015	M/C	133.FN318	Checked		Remarks	

All dimensions in MMS

الشركة الجزائرية للأسمنت
ALGERIAN CEMENT COMPANY S.P.A.

Impeller

All dimensions without tolerance will be 14 class (IT14)

Figure A.5: Blade arrangement and rotor dimensions.

A.6 Detailed shroud Dimensions

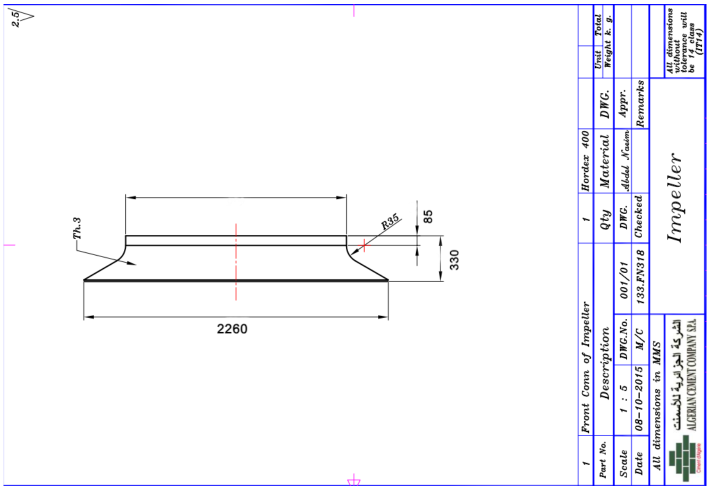

Figure A.6: Shroud dimensions

A.7 Detailed hub Dimensions

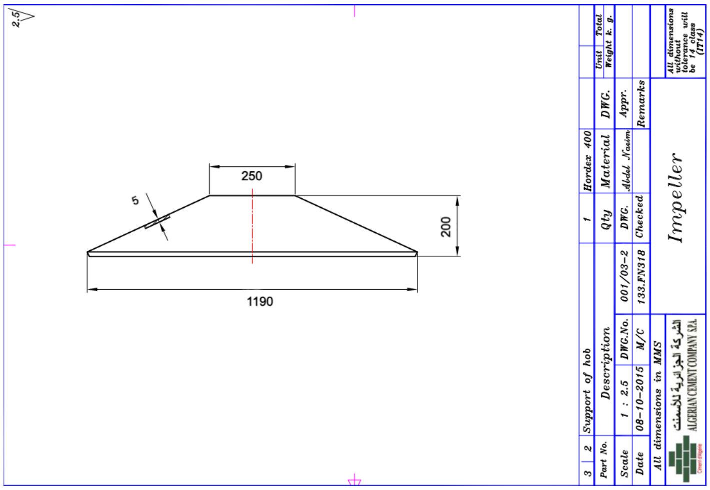

Figure A.7: Detailed hub Dimensions

A.8 Injection independence study

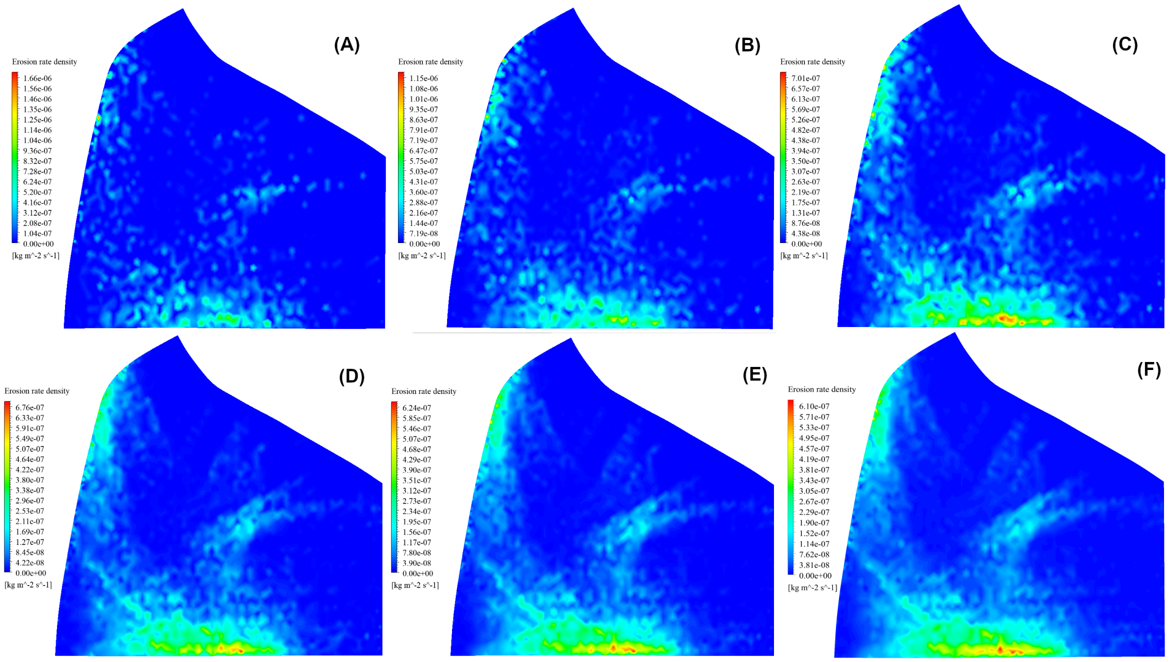

Figure A.8: Injection independence study; A) 300000 particles,B) 700000 particles,C) 900000 particles,D) 100000 particles,A) 1200000 particles,A) 1500000 particles

Abstract

Particle-laden flows are crucial for specific industrial applications but can have undesirable consequences, especially in industries like cement manufacturing that heavily rely on centrifugal fans. Operating under demanding conditions with a notable load of erodent solid particles poses challenges for these fans. Despite their widespread use, erosion in various fan types remains insufficiently explored. This thesis focuses on investigating the erosion process of an induced cement mill fan (FN-280). In pursuit of this objective, Unsteady three-dimensional numerical simulations using the Eulerian-Lagrangian approach were conducted to predict the fan's aerodynamic characteristics and particle dispersion. Results are compared with experimental data and on-site inspections to assess the simulation's effectiveness in predicting the fan's performance and erosion patterns. Additionally, a thesis section examines how altering the number of blades and the blade's outlet angle affects overall performance and erosion patterns.

The numerical fan's performance curve closely aligns with experimental data, validating the model's reliability. Findings underscore the model's ability to accurately replicate actual erosion patterns, emphasizing the substantial influence of particle size, flow conditions, and particle load on patterns and erosion rates. It is shown that increasing the blade outlet angle significantly intensifies erosion on the blade's pressure side, with the primary factor driving higher erosion rates being the interplay between particle impact angle and frequency. Adjusting the blade count has minimal impact on erosion patterns on the blade pressure side compared to changing the blade outlet angle, but a noticeable trend emerges with fewer blades, resulting in more pronounced erosion rates. This is suggested to be attributed to the higher local impact frequency on blades featuring fewer blades.

Résumé

Les flux chargés de particules sont essentiels pour certaines applications, mais ils peuvent entraîner des conséquences indésirable, en particulier dans des secteurs tels que la production de ciment, qui dépend fortement des ventilateurs centrifuges. Fonctionnant dans des conditions exigeantes avec une concentration significative de particules solides érodantes, ces ventilateurs font face à des défis. Malgré leur utilisation répandue, l'érosion dans divers types de ventilateurs reste insuffisamment explorée. Cette thèse se focalise sur l'étude du processus d'érosion d'un ventilateur de tirage de ciment (FN-280). Pour atteindre cet objectif, des simulations numériques tridimensionnelles instationnaires, utilisant l'approche Euler-Lagrangien, ont été réalisées pour prédire les caractéristiques aérodynamiques du ventilateur et la dispersion des particules. Les résultats sont comparés aux données expérimentales et aux inspections sur site afin d'évaluer l'efficacité de la simulation dans la prédiction de la performance aérodynamique du ventilateur et des motifs d'érosion. De plus, une section de la thèse examine comment la modification du nombre de pales et de l'angle de sortie de la pale affecte la performance globale et l'intensité d'érosion.

La courbe de performance numérique du ventilateur correspond étroitement aux données expérimentales, validant la fiabilité du modèle. Les résultats soulignent la capacité du modèle à reproduire précisément les motifs d'érosion observés sur site, mettant en avant l'influence substantielle de la taille des particules, des conditions de fonctionnement et de la charge de particules sur les motifs et l'intensité de l'érosion. Il est démontré que l'augmentation de l'angle de sortie de la pale intensifie l'érosion du côté pression de la pale, le principal facteur entraînant des taux plus élevés étant la combinasion de l'angle d'impact des particules et la fréquence d'impact. Cependant, ajuster le nombre de pales a un impact minimal sur les motifs et l'intensité de l'érosion du côté pression de la pale par rapport au changement de l'angle de sortie de la pale, mais une tendance notable émerge avec moins de pales, entraînant des taux d'érosion plus prononcés. Cela est suggéré être attribué à une fréquence d'impact locale plus élevée sur les pales comportant moins de pales.

ملخص

تعتبر التدفقات المحملة بالجسيمات ذات أهمية كبيرة في تطبيقات صناعية معينة، ولكن يمكن أن تكون لها عواقب غير مرغوب فيها في مجالات أخرى ، خصوصاً في قطاعات مثل إنتاج الإسمنت التي تعتمد بشكل كبير على مروحيات الطرد المركزي. تواجه هذه المروحيات تحديات كبيرة أثناء التشغيل في ظروف معينة أين يمكن للتدفق أن يحتوي على تركيز عالي من الجسيمات الصلبة المسببة للتآكل. على الرغم من استخدامها الشائع، إلا أن مشكلة التآكل الناتج عن الجسيمات الصلبة في أنواع مختلفة من المروحيات تزال تحتاج إلى دراسة مكثفة. تركز هذه الدراسة على دراسة عملية التآكل في مروحية خاصة تُستخدم في محطة طحن الإسمنت (FN-280). من خلال محاكاة رقمية ثلاثية الأبعاد الغير مستقرة باستخدام نموذج Eulerian-Lagrangian ، تم التنبؤ بالخصائص الديناميكية للمروحية ونقل الجسيمات داخل مجال المروحية. تم مقارنة النتائج مع البيانات التجريبية والفحوصات الميدانية لتقييم فعالية المحاكاة في توقع أداء المروحية وأنماط التآكل. بالإضافة إلى ذلك، ركزت جزء من الدراسة على تحليل تأثير عدد الشفرات وزاوية مخرج الشفرة على الأداء العام وأنماط التآكل.

أظهرت النتائج تطابق منحنى الأداء العددي للمروحية بشكل كبير مع البيانات التجريبية، مما يؤكد دقة النموذج المستخدم. كما أكدت النتائج قدرة النموذج على تكرار أنماط التآكل الفعلية بدقة، مشيرة إلى تأثير الحجم الجسيماتي وشروط التدفق وتركيز الجسيمات في التدفق على أنماط ومعدلات التآكل. أظهرت الدراسة أيضاً أن زيادة زاوية مخرج الشفرة تزيد بشكل كبير من معدلات التآكل على جهة الضغط للشفرة، وأن التفاعل بين زاوية اصطدام الجسيمات وتردد الاصطدام هو العامل الرئيسي الذي يُحفّز هذه الزيادة. وبالرغم من ذلك، فإن تعديل عدد الشفرات له تأثير ضئيل على أنماط التآكل على جهة الضغط للشفرة مقارنةً بتغيير زاوية مخرج الشفرة. لكن، ظهرت ارتفاعات ملحوظة في معدلات التآكل عند استخدام عدد أقل من الشفرات، ويرجع هذا الارتفاع إلى زيادة تردد التصادم في مناطق معينة من الشفرات في المروحية التي تحتوي على عدد أقل من الشفرات.